Online State Estimators for Lithium Ion Batteries

PALASH GAIKWAD

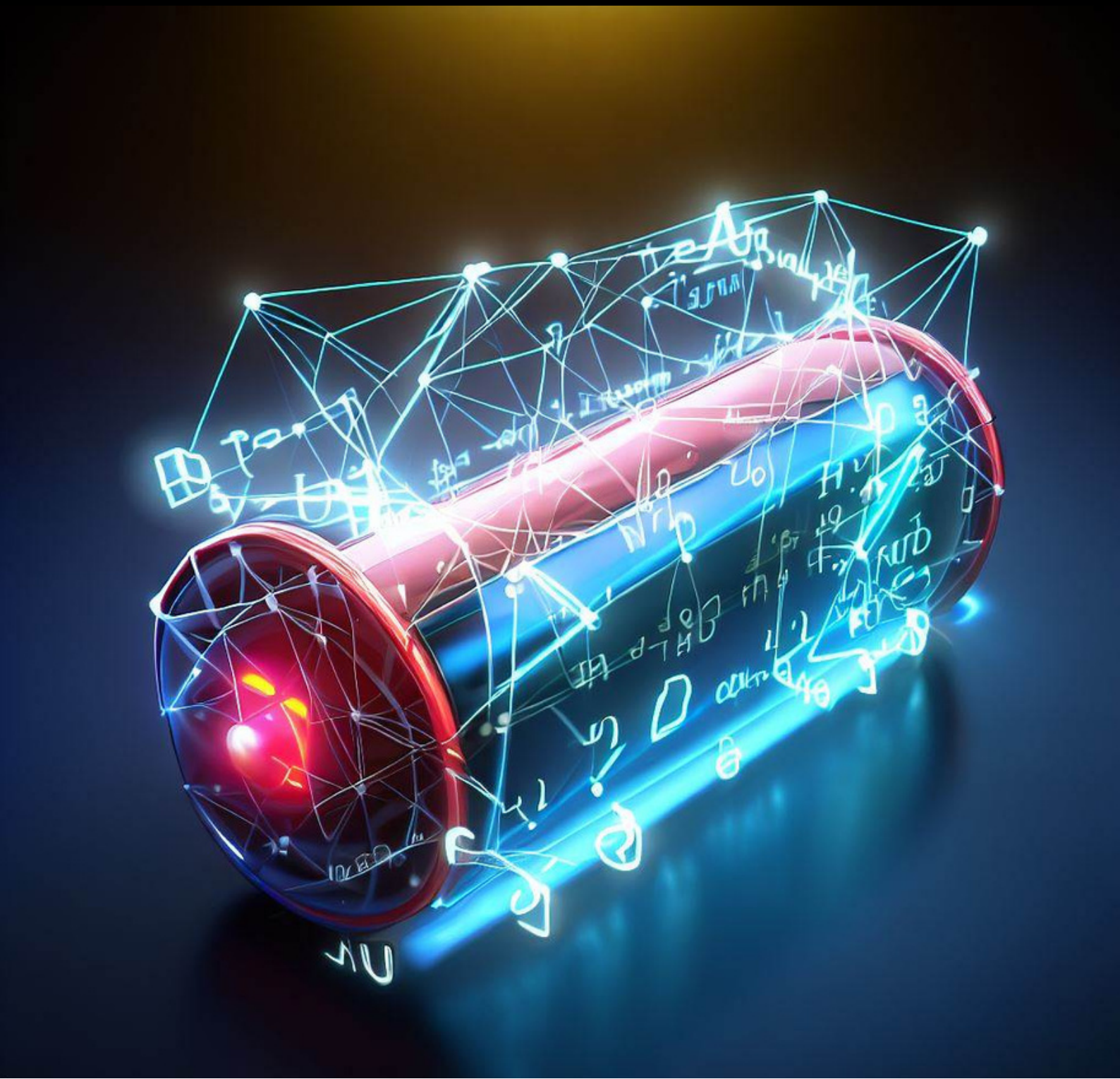

Online State Estimators for Lithium Ion Batteries

Development of a multi-physics based online State of health estimator for Lithium Ion batteries

by

Palash Gaikwad

Student Name	Student Number
Palash Gaikwad	5347785

to obtain the degree of Master of Science in Sustainable Energy Technology
at the Delft University of Technology,
to be defended publicly on Tuesday August 29, 2023 at 2:30 PM.

Thesis supervisor:	Prof. Pavol Bauer
Daily supervisor:	Dr.Gautham Ram Chandra Mouli
External Committee :	Dr. Rudi Santbergen
Daily PhD co-Supervisor:	Dario Slaifstein
Project Duration:	Nov,2022 - August,2023
Faculty:	Faculty of Electrical Engineering, Mathematics and Computer Science, Delft

An electronic version of this thesis is available at
http://repository.tudelft.nl/

Acknowledgements

Writing this master's thesis has been a challenging yet incredibly rewarding journey and I am delighted to present the culmination of my studies in Sustainable Energy Technology at TU Delft. This thesis marks the completion of my academic pursuits, and I am immensely grateful for the guidance and support I have received throughout this endeavor.

First and foremost, I would like to express my heartfelt gratitude to my supervisor, Dr. Gautham Ram Chandra Mouli ,for his exceptional supervision and guidance to help me steer the project and complete the thesis in time. I have enjoyed your courses taught in the electric-mobility track, and it has been a great learning experience.

I would also like to thank Prof. Pavol Bauer and Dr. Rudi Santbergen for being a part of the committee and taking the time to evaluate my thesis.

I am indebted to Dario Slaifstein, my PhD daily supervisor, whose invaluable expertise, encouragement, and unwavering belief in my abilities have been instrumental in shaping this work. Your insightful feedback and constructive criticism have been essential in refining my ideas and pushing me to explore new perspectives. The last two years at TU delft has been a great learning curve for me, and I have enjoyed every bit of it.

I would also, like to thank my parents for supporting me throughout this journey. Finally, I would like to thank my friends who made this journey worthwhile.

Palash Gaikwad
Delft, August 2023

Abstract

Batteries play a crucial role in powering contemporary devices and systems, ranging from smartphones and electric vehicles to renewable energy storage. With the increasing demand for more efficient and reliable battery technologies, the need for accurate monitoring and assessment of battery condition and performance has also grown. Online estimators, that continuously analyse battery conditions in real-time, have emerged as valuable tools to meet these goals. This thesis focuses on constructing model-based online state estimators for real-time estimation of a battery's State of Health (SOH).

These estimators, necessitate a state space model for a lithium-ion cell. In the initial part of the thesis, a physics-based reduced-order model (ROM) of a lithium-ion cell is developed. This model accounts for major aging mechanisms such as Solid Electrolyte Interphase (SEI) layer formation, Loss of Active Material (LAM), and Lithium Plating (LIP). To incorporate temperature effects on cell parameters, a simplified lumped thermal model is integrated into the battery model. The model is subsequently transformed into a state space model using the Discrete Realization Algorithm (DRA) process.

Building upon the noisy outputs from the ROM models, a set of five estimators is formulated: State of Charge (SOC), Voltage, SEI loss, LAM loss, and LIP loss estimators. These estimators are constructed based on Kalman filters and collectively contribute to real-time prediction of a battery's SOH. Given their reliance on the model, the ROM model's output is employed as a reference to gauge the precision of the estimators.

To address the real life scenarios and to check the robustness of the estimators, a series of sub-questions were analysed:

Sub question1: How to estimate the SOH of a cell in real-time using adaptive control techniques ?

Sub question2: How fast can the estimator react to changing initial states of the cell?

Sub question3: Can the estimators be adapted to concurrently estimate both the states and the time varying cell parameters in case of an old cell? How fast can this be achieved in real-time ?

Overall, this research contributes to the development of model-based online estimators, which are poised to have a significant impact on enhancing battery performance, prolonging lifespan, and facilitating the transition towards a more sustainable energy future.

Contents

List of Figures

List of Tables

List of Abbreviations

Abbreviation	Definition
P2D	Pseudo 2-Dimensional
DFN	Doyle Fueller Model
SPM	Single Particle Model
OCV	Open Circuit Voltage
SOH	State of Health
SOC	State of Charge
ECM	Equivalent Circuit Models
PBM	Physics based Models
EMs	Empirical Models
EV	Electric Vehicles
ICEs	Internal Combustion Engine
LIB	Lithium ion Batteries
PbAc	Lead acid battery
NiMH	Nickel- metal hydride battery
SSBs	Solid state batteries
SSE	Solid state electrolyte
LAM	Loss of Active Material
LIP	Lithium Plating
OEMs	Original Equipment Manufacturer

1

Introduction

Today, the world faces energy challenges on two frontiers: shifting electricity production from burning fossil fuel to sustainable energy sources and using EVs instead of cars driven by ICEs. EVs are well recognized in the automobile industry due to their improved performance and efficiency as well as their contribution to address environmental issues of greenhouse gas emissions and global warming [1].The performance of EV is defined by its reliability, safety, driving range, power management system[2].

Due to their high power density (≈1200 W/kg) and energy density (≈200 Wh/kg),high energy efficiency (>95%), and relatively long cycle life measured in thousands of cycles, Li-ion batteries are the accepted solution for electronics, transportation, and grid storage [3]. With the rapid development of industrial technology and the continuous improvement of the degree of product integration and intelligence, the application scenarios of lithium-ion batteries tend to be complicated [4]. The bottleneck usually lies with lower costs and higher energy densities over a long lifetime [4].The predictive maintenance of lithium batteries can effectively reduce maintenance costs, shorten failure times, and improve system reliability. Predictive maintenance is strongly based on the SOH of the battery; therefore, accurate life prediction is the key to effective predictive maintenance.

Currently, the life prediction of lithium-ion batteries is based on prior knowledge of historical battery usage data. This historical data is used as input parameters in the mathematical models which work in offline mode to predict the battery behaviour. These models are usually not very flexible to changing external dynamics. With the development of sensor technology and data analysis methods, the concept of the online estimators provides inspiration and technical ways to solve the above problems[5].

This thesis discusses the development of a multi physics based model of Lithium Ion batteries developed in Matlab software for online State of health estimation. An online estimator uses real life data and virtual model simulation technology to explore and predict the operating state of physical space, which provides the important theoretical basis and technical support for the connection and real-time interaction between virtual and physical space [6].

1.1. Motivation and research gap

Since the early 90's, academia and industry have done extensive research on the different aging mechanisms and came up with 4 methods for modeling LIB degradation behavior

- Machine learning models (MLMs)
- Empirical and semi-empirical models (EMs)
- Physics based models (PBMs)
- Equivalent circuit models (ECMs)

In depth overview of each model is discussed in Chapter 2. Each of these modelling techniques have a potential to predict the aging behaviour of a LIBs with a varying degree of accuracy. Despite the development of these individual models, there have been very few attempts to a combine these modelling techniques.
In literature the state-of-the-art methods in battery-management algorithms use equivalent-circuit cell models as a basis. These algorithms can work very well and are representative of the methods used in practically every fielded BMS at this point. However, majority of the ECM models and EM models are static in nature and cannot detect how the stoichiometric operating windows have shifted in each electrode.This is valuable input to power-limit calculation, because voltages and internal electrochemical potentials that an aged cell can withstand are often different from those of a new cell [7]. SOH estimation using physics-based models is valuable for detecting stoichiometric operating windows in cells, enabling valuable input for power-limit calculations. There have been attempts to use physics based electro-thermal models along with degradation mechanisms to optimise the charging strategies [8] [9] [10] or models based on online state estimations using only the physics based performance model [11] [6]. There still lacks an electro-thermal-aging model based online SOH estimator that can adapt to different parameter states based on the condition of the battery in literature. This thesis attempts to develop an algorithm that can accomplish this goal.

1.1.1. Research objectives and questions

The aim of this research is to develop algorithms for online state of health estimation using a multi-physics reduced order models, that takes into account major degradation mechanisms and a lumped thermal model.

The research sub questions are:

1. How to estimate the SOH of a cell in real-time using adaptive control techniques ?
2. How fast can the estimator react to changing initial states of the cell?
3. Can the estimators be adapted to concurrently estimate both the states and the time varying cell parameters in case of an old cell? How fast can this be achieved in real-time ?

1.2. Report Overview

This report is structured as follows:

- **Chapter 2** : Provides a review of literature about the different battery modeling techniques. Later it discusses the dynamics behind the main three-electrochemical models and makes comparative analysis of the models.Finally it ends with the classification of different aging mechanisms and review of models available in literature.
- **Chapter 3** : This Chapter discuses the process to model a reduce order model with aging mechanisms and a lumped thermal model. A validation of the reduced order model is also discussed. This chapter forms the base to model different online state estimators.
- **Chapter 4** : discusses the algorithms to build real time online-state estimators and discusses the flow of the thesis.
- **Chapter 5** : discusses the speed of the estimators to adapt to various initial conditions.
- **Chapter 6** : Concludes the findings and presents limitations and future work.

2

Literature Review

The objective of this chapter is to present a comprehensive literature review on Battery Modeling . Firstly, in section 2.1 a background on how Li-ion batteries function and an overview of various Lithium Ion chemistries are covered.Followed by the current trends of EV batteries and the need for battery modelling are discussed in Section 2.2. Finally, battery modelling methodologies and a review of them is provided in Section 2.3.

2.1. Operation of a Lithium Ion cell

A battery pack contains one or many identical cells. Each cell stores electric power as chemical energy. LIBs consist of a positive and negative electrode, an electrolyte, and a separator. The electrodes lay in the electrolyte, a chemical liquid that allows the flow of the Li-ions, but not of the electrons. The separator is a porous plastic that separates the two electrodes to prevent them from short-circuiting.

During discharge, the electrode that releases the positively charged Li-ions is called the anode, and the electrode that absorbs Li-ions is the cathode. Figure 2.1 shows how the Li-ions that intercalate through the electrolyte and the separator towards the cathode, create a flow of negatively charged electrons from the anode through an external circuit and towards the cathode, to neutralize the charge at the receiving electrode.

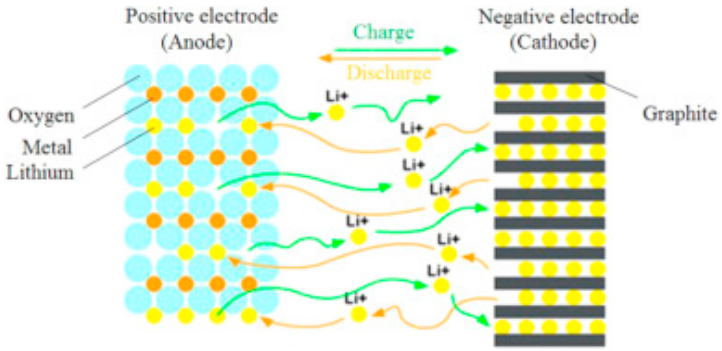

Figure 2.1: Working of Lithium Ion battery [12]

From the battery point of view, during the discharge cycle anode is the graphite electrode and cathode is the transition metal electrode. Therefore the main, reaction is:

$$Li_xN \rightleftharpoons xLi^+ + xe^- + N \tag{2.1}$$

where N is the active negative electrode material and x represents Li amount in the negative electrode [13]. Similarly, the main reaction at the positive electrode is

$$yLi^+ + ye^- + P \rightleftharpoons Li_yP \tag{2.2}$$

where P is the active positive electrode material and y represents Li amount in the positive electrode. The flow of electrons created by the flow of Li-ions creates an opposite flow of electrical current, which can power an electric device or vehicle. During charging, the flow reverses.

2.2. Current Trend of EV Batteries

Over the years,variety of rechargeable battery chemistries have been used to power EVs, with the three main types being PbAc,NiMH and LIB. LIBs have taken the stage in EV applications due to their , high volumetric energy density, high specific power, and low self-discharge rate. Figure 2.2 shows the comparisons of different batteries based on their volumetric energy density $(\frac{Wh}{l})$ and power density $(\frac{Wh}{Kg})$. It can be seen that lead acid batteries have the lowest energy and power density, while Solid State Batteries (SSBs) have the highest power and energy yield. SSBs use a Solid State Electrolyte (SSE) and a lithium metal anode instead of a liquid electrolyte and a carbon anode that LIBs use, which could result in a 20% energy density improvement. However, technical challenges with SSEs, coupled with the decreasing cost of liquid electrolytes, lead researchers to conclude that LIBs will likely remain the favored technology in the foreseeable future.

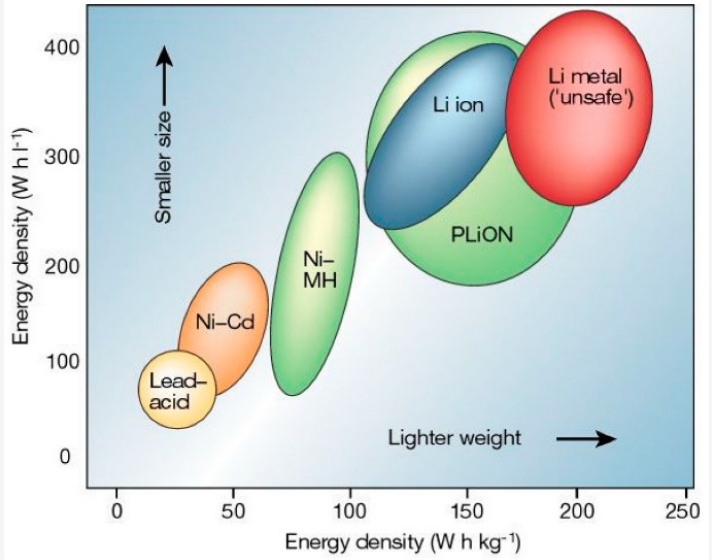

Figure 2.2: Ragone plot of several of the battery technologies used in EVs [14]

2.2.1. Current Trend of Li-ion research

There has been extensive research in the field of Li-ion batteries. fig 2.3 shows the trend of Li-ion battery research based on keyword search. The database consists of roughly 5000 research papers complied in clusters based on the similar keywords used. The larger the cluster the greater amount of research articles available on the subject. The keywords are colour coded based on the year of publishing .

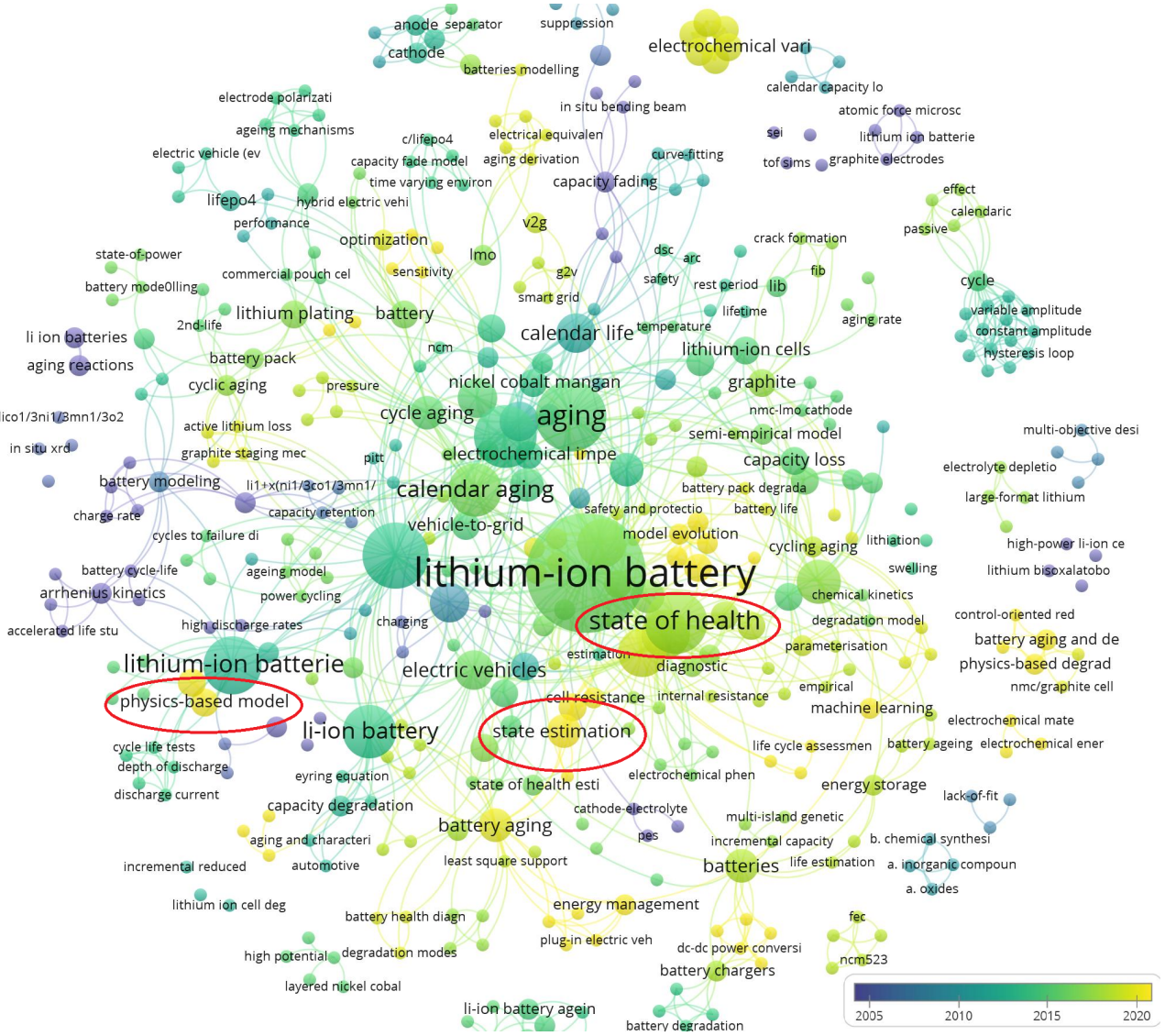

Figure 2.3: Visualization of trend in Lithium Ion research in literature based on Keywords

It can be inferred from the survey that online state of health estimation using physics based models is a very new topic, with lot of work of active research carried out in last 4 years.

2.2.2. Li-ion chemistries

Because of the chemistry of their electrodes, LIBs have different properties. Due to its availability, affordability, extended cycle life, high specific energy (gravimetric energy density), and high specific power (gravimetric power density), graphite is the most often utilised anode material for LIBs. The most used options for cathodes are:

1. Lithium Iron Phosphate (LFP)
2. Lithium Cobalt Oxide (LCO)
3. Lithium Nickel Manganese Cobalt Oxide (NMC)
4. Lithium Nickel Aluminum Oxide (NCA).

Anode Options:

1. Graphite (Carbon based) : It is the most common anode material due to its stable cycling performance and relatively low cost. However, its energy density is limited compared to some other materials.

2. Lithium Titanate (Li4Ti5O12) : This is the anode used in LTO batteries. The main advantage is the faster charging times and high cycle life, but the overall energy density is low compared to traditional graphite based batteries. The cost is also high and acts as a major hurdle in commercial use of LTO batteries [15].
3. Silicon (Si) : Silicon anodes have the potential for much higher energy density than graphite, but they suffer from significant volume changes during charging and discharging, leading to performance degradation over time.

The energy density or Volumetric density of a battery refers to the amount of energy stored in the battery per unit volume usually measured in $(\frac{Wh}{l})$. It is an essential factor in determining the overall performance and range of various applications, including electric vehicles and portable electronics. Power density or gravimetric density, on the other hand, measures how fast the battery can deliver the energy, expressed in watts per kilogram $(\frac{Wh}{Kg})$. The energy and power densities of each kind are discussed below:

Table 2.1: Theoretical and Industrial energy densities for cathode materials [16][12]

Cathode Material	**Theoretical Energy Density (Wh/kg)**	**Industrial Energy Density (Wh/kg)**
Lithium Iron Phosphate	∼160	∼90-120
Lithium Cobalt Oxide	∼200-220	∼150-200
Lithium Nickel Manganese Cobalt Oxide (NMC)	∼200-230	∼150-200
Lithium Nickel Cobalt Aluminum Oxide (NCA)	∼200-250	∼170-200

Table 2.2: Theoretical and Industrial Energy Densities for Anode Materials [16]

Anode Material	Theoretical Energy Density $\frac{mAh}{g}$	Industrial Energy Density $\frac{mAh}{g}$
Graphite	∼372	∼325
Silicon	∼4200	∼2000 (improved with nanostructured silicon, etc.)

- **LCO**:
  The primary benefit of the LCO battery is its high specific energy and low self-discharge rate [17]. The downsides of the LCO battery include its low thermal stability, which poses safety issues, its restricted specific power, its relatively short lifespan, and its usage of contentious cobalt [17].
- **LMO**:
  LMO batteries offer low internal resistance, good current handling, and safety compared to LCO [18]. The downside is that they have short lifespans and average specific power, energy, and low performance due to capacity fading [19]. However, their design flexibility allows for optimization for high specific energy, or long lifespan. Blending LMO and NMC improves certain qualities, such as high current boost during acceleration and extended driving range. OEMs often blend these two chemistries for improved performance [18].
- **LFP**
  The key advantages of the LFP battery are its safety due to its thermal stability, extended lifespan, and lack of cobalt. Its performance is related to minimising the battery's relatively rapid self-discharge by employing expensive, high-quality cells or using control electronics. Its downsides are its poor specific energy and average specific power [18].
- **NMC**:
  The advantage of the NMC battery is that it can, similarly to LMO, be optimized to serve a certain purpose. Nickel on itself provides high specific energy but poor stability, and manganese on itself provides low internal resistance but low specific energy. By blending nickel and manganese, the strengths of the two materials are enhanced which according to [20] makes NMC the most successful Li-ion system. Cobalt increases its specific energy, thermal stability, lifespan, and safety [20]. Blends of nickel,cobalt, and manganese in proportions of 1:1:1, 5:3:2, 8:1:1 have proven to offer useful combinations of qualities while reducing the amount of cobalt in the battery [21], [22].
- **NCA**:
  The advantages of the NCA battery, in which aluminium is used to improve stability, are similar

to that of NMC. NCA batteries provides a high specific energy, average specific power and long lifespan [23]. Its disadvantages are its high cost and lack of safety.[20].

- **LTO**:
  The LTO battery uses titanate for its anode instead of graphite, which all the aforementioned battery chemistries use. The advantages of LTO are its safety due to its thermal stability, and its long lifespan [17]. The disadvantage of LTO is its low specific energy and high cost.

A detailed comparison of key performance aspects is shown in figure 2.4. LFP, NMC and LTO batteries will be discussed below. It can be observed that:

1. **Cost:** NMC batteries are the most costly form of Li-ion battery under consideration, whereas LTO batteries are the least expensive.
2. **Specific Energy:** NMC batteries are shown they have the highest specific energy amongst LFP and LTO batteries. This implies for a required size of the battery in kWh NMC batteries would occupy the least amount of space. LFP and LTO batteries would occupy a similar amount of space.
3. **Specific Power:** Among NMC and LTO batteries, LFP batteries offer the highest potential specific power. The particular power capacities of NMC and LTO are comparable.
4. **Safety:** LFP and LTO batteries are amongst the safest batteries in the industry.
5. **Performance and Lifespan:** Because of their unique anode material, LTO batteries last a long time and charge rapidly, but LFP batteries feature a robust cathode material that makes them safer and allows them to run at high temperatures without substantial deterioration.

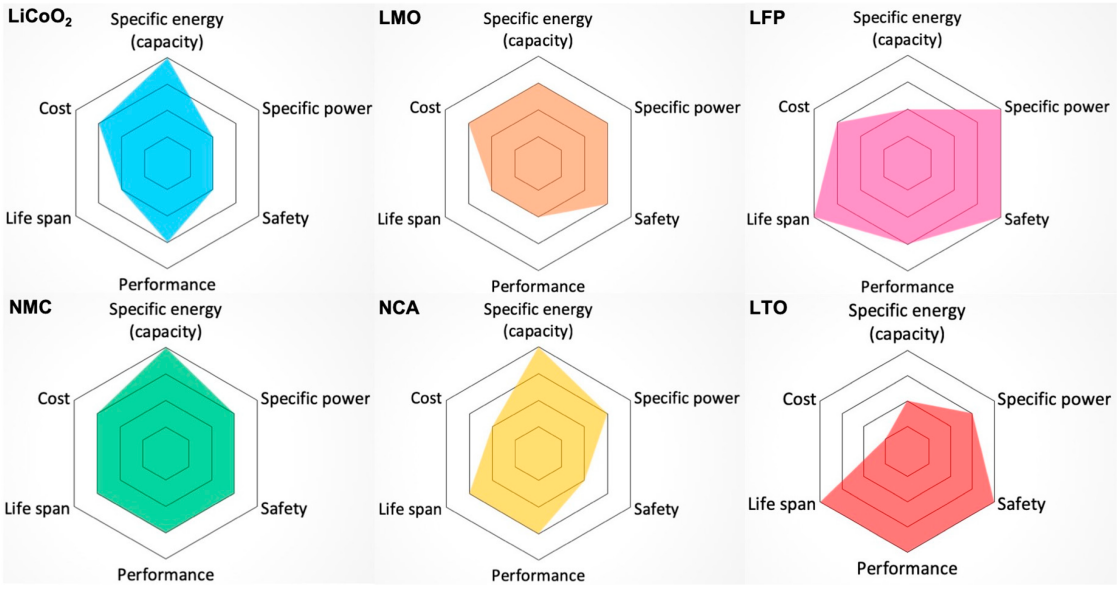

Figure 2.4: Comparison of different Li-ion chemistry's [20]

The demand for batteries is increasing by 32% annually, with China having the biggest demand [14] as seen in fig. 2.4.

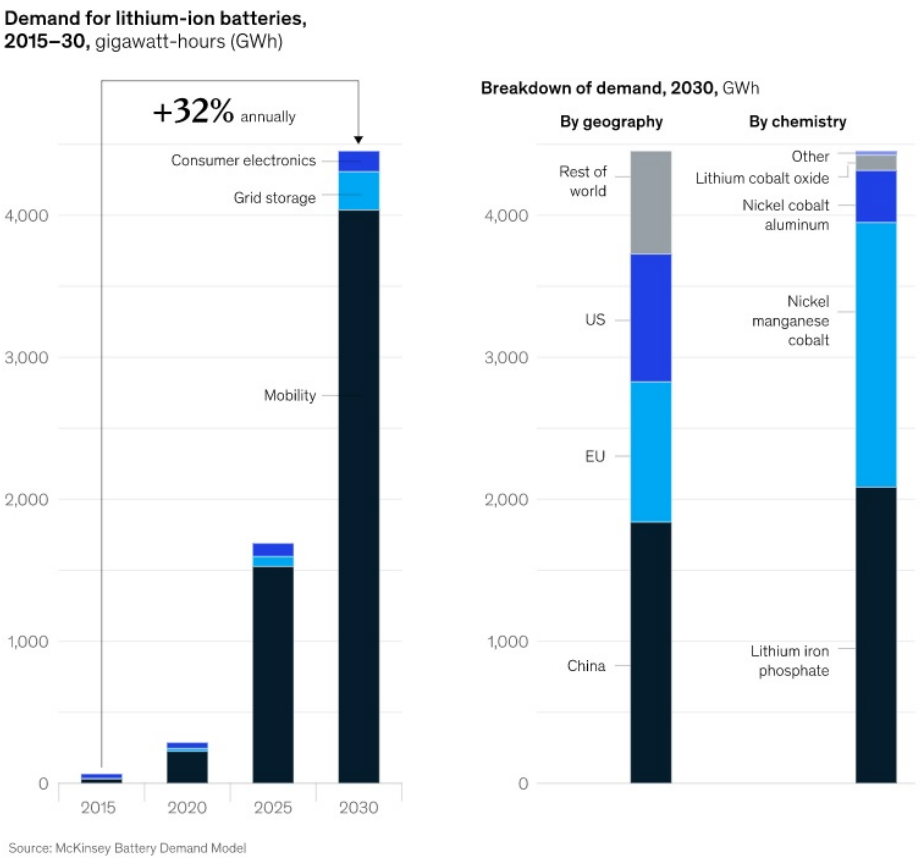

Figure 2.5: Lithium Ion demand [14]

The same might be stated for contemporary LIB uses in Grid Storage applications, albeit Lithium Iron Phosphate, LFP-based chemistry has had a large market share in this sort of application during the previous decade. The industry, on the other hand, is devoted to creating cobalt-free cathodes. It is worth noting that the cathode generally restricts cell capacity and hence LIB performance because it has a lower capacity than the graphite anode and is the most costly material in a LIB, resulting in its establishment as a critical LIB component and the topic of much study. [14].

2.2.3. Li-ion Battery aging

Before modelling physics , it is essential to understand aging in LIBs in detail . The causes of battery degradation mechanisms, associated degradation modes, and the subsequent effects on the battery are shown in the diagram in Figure 2.6

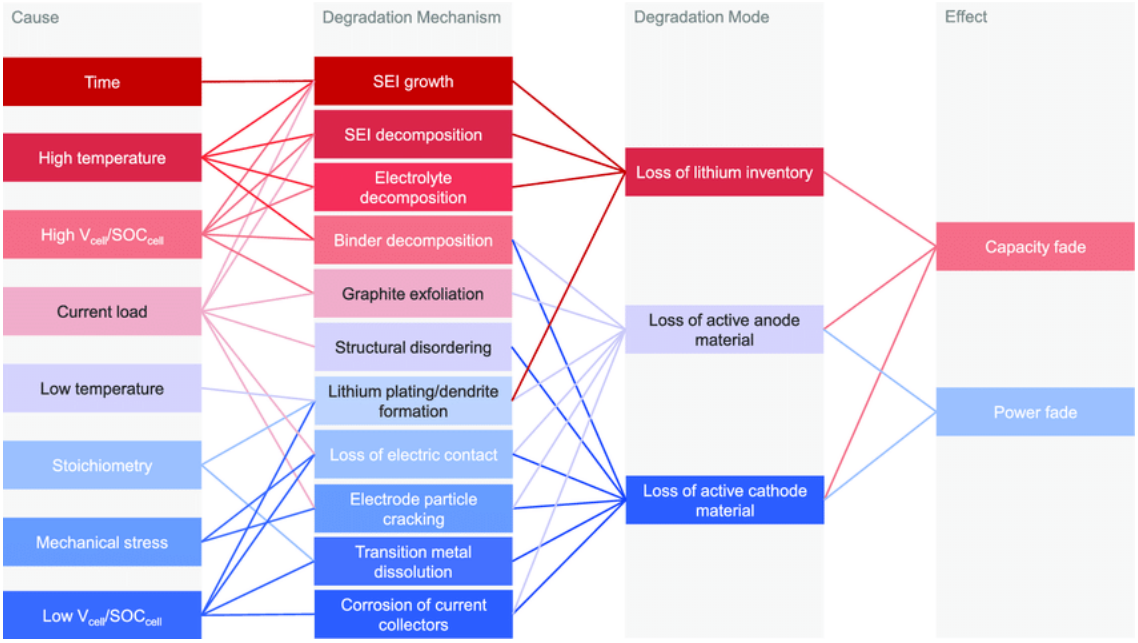

Figure 2.6: Different battery degradation mechanisms [24][23] [25]

The degradation of LIBs occurs during both cycling and idle states, and is caused by physical stress and chemical side reactions [23][26]. In addition, many factors influence battery degradation, such as cell chemistry, cell design, pack design,and operating conditions. LIB aging is commonly categorized into three different aging modes[27].

- Loss of Lithium Inventory (LLI) :It indicates the loss of active lithium ions, which are no longer accessible for active battery operation. LLI can be caused by parasitic side reactions such surface film formation, decomposition processes, and lithium plating. LLI is linked to capacity fading [27].

- Loss of Active Material (LAM) : When a battery is charged and discharged, Li-ion is intercalated, and most electrode materials expand before contracting on de intercalation.The alternating strains in the electrodes caused by these volume expansion-contraction cycles result in fracture propagation. This might result in structural degeneration of the anode or cathode material.LAM has the potential to reduce both power and capacity [27].

- Conductivity Loss (CL) : This is a contact loss caused by electrical component degradation, such as current collector corrosion and binder dissolution. [27].

Aging in a LIB occurs at anode and cathode. The electrolyte is not affected by the battery operation in reference to aging effects.

Anode aging

The negative electrode active materials in most commercial lithium-ion battery cells are made of synthetic or natural graphite.Graphite has a high lithium storage capacity, is affordable and nontoxic, and can be charged and discharged repeatedly. Perhaps most importantly, lithiated graphite has a very low voltage in comparison to a lithium-metal reference. Because cell voltage is equal to the positive-electrode potential minus the negative-electrode potential, this is critical for maximising overall cell voltage. SEI generation, Lithium plating, and mechanical stress are the key anode ageing processes. fig 2.7 depicts a summary of anode ageing in LIBs.

Cause	Effect	Leads to	Enhanced by
Electrolyte decomposition, builds SEI, continuous low-rate reaction	Loss of lithium, impedance rise	**Capacity fade, Power fade**	High temperatures, high SOC (low potential)
Solvent co-intercalation, gas evolution and subsequent cracking formation in particles	Loss of active material (graphite exfoliation), loss of lithium	Capacity fade	Overcharge
Decrease of accessible surface area due to continuous SEI growth	Impedance rise	**Power fade**	High temperatures, high SOC (low potential)
Changes in porosity due to volume changes, SEI formation and growth	Impedance rise, larger overpotentials	Power face	High cycling rate, high SOC (low potential)
Contact loss of active material particles due to volume changes during cycling	Loss of active material	**Capacity fade**	High cycling rate, low SOC
Decomposition of binder	Loss of lithium, loss of mechanical stability	Capacity fade	High SOC (low potential), high temperatures
Current collector corrosion	Larger overpotentials, impedance rise, Inhomogeneous distribution of current and potential	Power fade, Enhances other aging mechanisms	Overdischarge, low SOC (high potential)
Metallic lithium plating and subsequent electrolyte decomposition by metallic lithium	Loss of lithium (loss of electrolyte)	Capacity fade (power fade)	Low temperature, high cycling rates, poor cell balance, geometric misfits

Figure 2.7: Summary of anode aging in LIB [28]

Cathode aging

The cathode is the lithium-containing part of a cell, and the limiting factor during charging as its maximum voltage determines the end of charge voltage.Common cathode chemistries are LCO, LFP, NMC, LMO,and NCA. The main aging mechanisms of cathode materials include surface film formation, mechanical stress, and transition metal dissolution.Fig 2.8 shows the summary of cathode aging in LIBs

Cause	Effect	Leads to	Enhanced by
Phase transitions	Cracking of active particles	Capacity fading	High rates, high/low SOC
Structural disordering	Lithium sites lost and lithium trapped	Capacity fading	High rates, high/low SOC
Metal dissolution and/or electrolyte decomposition	Migration of soluble species,	Capacity fading	High/low SOC, high temperature
	Reprecipitation of new phases,	Power fade	
	Surface layer formation	Power fade	
Electrolyte decomposition	Gas evolution		High temperature
Binder decomposition	Loss of contact	Power fade	
Oxidation of conductive agent	Loss of contact	Power fade	
Corrosion of current collector	Loss of contact	Power fade	High SOC

Figure 2.8: Summary of Cathode aging [28]

Various other degradation mechanisms exist, such as surface cracking,electrolyte drying, gas formation, current collector corrosion, etc.[26]. These mechanisms are not very common and contribute less to the overall aging of the LIB. The table 2.6 provides an overview of the many degradation models

available in the literature. The majority of studies have modelled SEI development as kinetically restricted. When Li-ion is intercalated, the electrode materials expand and compress. These alternating stresses caused by volume expansion and contraction cycles cause fracture formation and material fatigue in the electrodes. When cracks emerge at the electrode's surface, more cyclable lithium leaks out, causing the SEI layer to grow on a greater surface area, [29]. A relationship is established between surface concentrations and deintercalation stress. This is the most often used approach in the literature to mimic crack propagation and active material loss. Li-Plating is represented by disintegration procedures that adhere to typical Butler-Volmer or Tafel kinetcs.

	SEI growth			Crack growth			LAM				Li-plating	Other	
paper	Kinetically Limited	Solvent diffusion Limited	electron tunneling	simplefied correlation	physical stress	physical crack growth	simplified correlation	physical stress	physical crack growth	simplified correlation	dissolution		
Appiah,2016	x										x		x
Ashwin,2016	x												
Barai,2015							x					x	
Cannarella, 2015											x		
Christensen,2005	x	x								x			
Delacourt,2012	x												
Deshpande,2012				x	x	x							
Deshpande,2017				x			x						
Ekstrom,2015	x	x					x						x
Ge,2017												x	
Jin,2017	x			x						x			x
Kamyab,2019	x	x											
Kindermann,2017	x						x				x		
Kupper,2017	x			x									
Kupper,2018	x			x	x		x						
Laredsgoiti,2015					x	x	x						
Legrand,2014			x										
Li,2015												x	
Lin,2013	x			x							x		
Narayanrao,2012				x					x	x			
Ning,2004	x												
Pinson,2013	x	x											
Ploehn,2004		x											
Purewal,2014				x	x	x							
Ramadass,2004	x												
Randall,2012	x												
Safari,2009	x	x											
Safari,2010	x						x						
Safari,2011	x	x											
Single,2017	x	x											
Tahmasbi.,2017	x	x											
Tang,2012	x		x	x									x
Yang,2017	x	x											

Table 2.3: Overview of various degradation models grouped by physical degradation mechanisms
[29]

2.3. Battery Modeling

Batteries are complex electrochemical systems governed by various electrical, thermal factors, and deterioration. Utilizing a battery model to represent cell dynamics is crucial for analyzing battery-based storage systems. These models enable prediction and optimization of system behavior under various circumstances. Advancements in software and processing power have made modeling and simulation tools more efficient and cost-effective. There are four different ways to model LIB performance and deterioration.

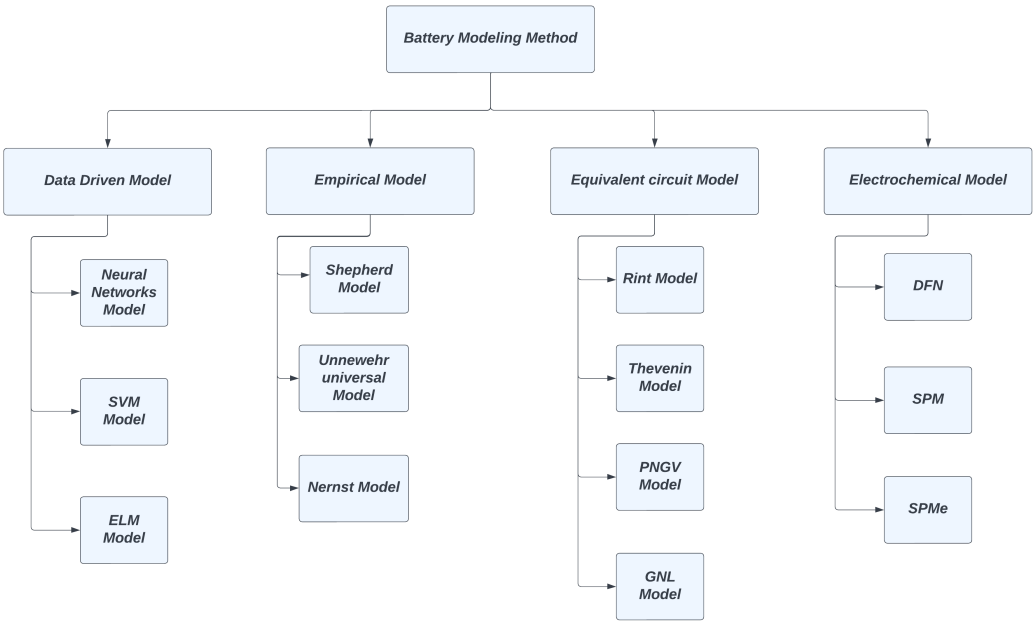

Figure 2.9: Different Battery Modeling Methods [30]

2.3.1. Data Driven Models

Data Driven Models feed an algorithm data for it to be able to use simple parameters like voltage,current and temperature to predict ageing, or combine empirical modeling methods with regression models to predict ageing.The advantage of these approaches is that, the models can be considered as a black box to train the algorithms. Few other data driven techniques available in literature are based on model parameters, such as ohmic resistance, polarization resistance, and polarization capacitance studied by [31], [32], or combine empirical modeling techniques with regression models to predict the SoH used by [33].

A multi layer neural network, known as an Radial Basis Function Neural Network (RBFNN), can use the Gaussian function as the activation function in the hidden layer.These models are used to model the nonlinear relationship of the battery [34]. Support Vector Machine (SVM) reaches an optimal solution more quickly than NN. The SVM is better suited to solve a problem with limited sample size when structural risk reduction is substituted with experiential risk minimization. The SVM is used for simple battery models, which does not include intricate non linearity. Terminal voltage is the product of the two-level SVM structure, where current and SOC are the input vectors [35].

The advantages and disadvantages of Data driven Models are summarised below:

Advantage:

- **Flexibility** These models can adapt to various battery chemistries, designs, and operating conditions without requiring a deep understanding of the underlying physics.
- **Real-World Representation** Data-driven models are based on empirical data, making them well-suited for capturing real-world variations and uncertainties.

Challenges:

- **Data Quality** The precision of data-driven models is strongly dependent on the quality, quantity, and variety of accessible data..
- **Interpretability** Some complicated data-driven models may be difficult to interpret, making it difficult to comprehend the logic behind their forecasts.

2.3.2. Empirical and semi-empirical models (EMs)

Semi-empirical and empirical models curve-fit the relationship of ageing stress components onto empirical degradation data of a specific cell to develop simple mathematical expressions that might forecast ageing. The distinction between the two is that semi-empirical models are physics-motivated, whereas empirical degradation models do not incorporate physical and electrochemical ageing mechanisms, instead relying solely on experimental data to forecast ageing.Because of their simplicity, EMs may be used in a broad range of research, including system-level design challenges, optimisation models, and battery management systems. Furthermore, the mathematical formulae provide an intuitive feel for the influence of various stress conditions [27].

The downside of these models is that their flexibility in terms of operating circumstances is restricted after they have been calibrated with particular data. The usage of the mathematical expressions is thus limited to the operational circumstances used to build the ageing model.Furthermore, the mathematical expressions specified in these models are frequently based on data acquired from accelerated ageing studies and constrained test settings due to a lack of accessible equipment or time.In addition, EMs are prone to oversimplifying the complicated behaviour of LIB ageing and the relationship between stress factors.

2.3.3. Equivalent Circuit Models (ECMs)

The equivalent circuit model characterizes the operational characteristics of a circuit by using a circuit component to form a specific network. It establishes the relationship between external characteristics of a battery and its internal state. This model is intuitive, easy to process, and moderate in computation, making it suitable for simulation experiments and practical engineering applications [36].
G.L Plett in his book Battery Management Systems, Volume 1 - Battery Modeling" [7]used a series of elements including the combined, simple, zero-state hysteresis, one-state hysteresis, and a non-linear enhanced self-correcting (ESC) model to adaptively estimate the battery's SOC. To increase model accuracy for dynamic load profiles, the latter model considered the impacts of current direction, the SOC dependency of open-circuit-voltage (OCV) hysteresis, and the relaxation or charge-recovery effect [37]. In an attempt to model the OCV hysteresis behaviour together with the charge recovery effects, Roscher et al. [38] developed an empirical model whose parameters required offline identification, Huria et al.[39] proposed a mathematical model to describe the dynamics of the large hysteresis levels that exist amongst high-power lithium-ion cells.
Figure 2.6 shows the summary of major ECM models in literature . The Thevenin model is created by adding an extra RC network to the Rint model, which better captures dynamic terminal voltage. The PNGV model, produced by adding a capacitor C_cap, represents OCV fluctuation by discharging current buildup. Increasing the number of RC networks helps to characterise terminal voltage in greater detail, with the PNGV model typically outperforming the Rint and Thevenin models in terms of accuracy. One extra RC network is included in the GNL model to account for the concentration polarisation effect.

Model	Expression
Rint model 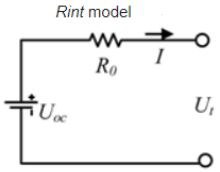	$U_t = U_{oc} - I \cdot R_0$ U_t is the terminal voltage, U_{OC} indicates the OCV. I is the discharging current and R_O is the *Ohm* resistance.
Thevenin model 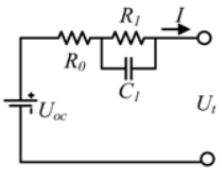	$U_t = U_{oc} - U_1 - I \cdot R_0$ R_1 is the polarization resistance and C_1 is the polarization capacitance, U_1 is the voltage of the RC network.
PNGV model 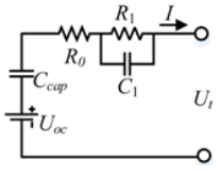	$U_t = U_{oc} - U_{cap} - U_1 - I \cdot R_0$ *Ccap* is the bulk capacitance.
GNL model 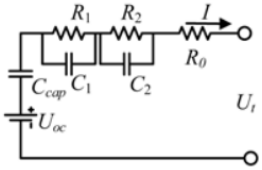	$U_t = U_{oc} - U_{cap} - U_1 - U_2 - I \cdot R_0$ R_2, C_2 are the concentration polarization resistance and capacitance.

Figure 2.10: 1-RC model with Diffusion[30]

Equivalent circuit aging models

The bulk of ECM models do not account for the battery's internal states during operation, such as Li-ion concentration, overpotential, and deterioration. However, attempts have been made to include the dynamics of the battery into ECM models. In [40], for example, a 1-RC model with diffusion resistance illustrated in fig. 2.11 diffusion has been constructed to replicate the battery's diffusion phenomena in the low-frequency region. The time-varying diffusion resistance is calculated using a large quantity of experimental data.

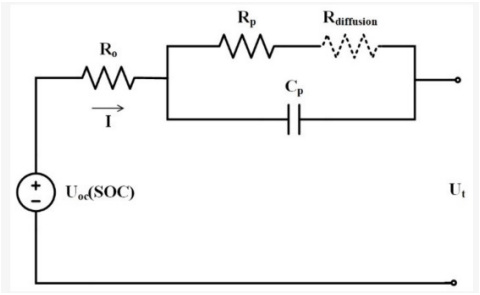

Figure 2.11: 1-RC model with Diffusion[40]

The article [41] proposes a method for measuring SOC and SOP simultaneously using a 1-RC model that accounts for self-discharge. This technique employs a time-based model, as shown in fig. 2.12 discharge, that contains a capacity, self-discharge resistance, and regulated current source in parallel. This model attempts to predict the long-term impacts of battery cycling and calendar ageing on available battery capacity.

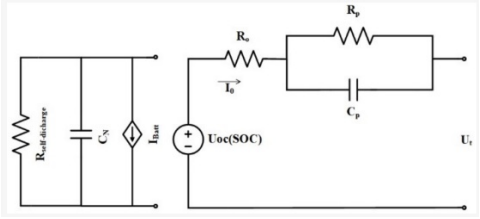

Figure 2.12: 1-RC model with self discharge[41]

The DP model, depicted in Figure 2.13, is a commonly used ECM for estimating SOH. It utilizes two RC networks with distinct time constants to describe the charge transfer process, double-layer effect, and diffusion phenomenon, resulting in better model accuracy than the 1-RC model, particularly at extreme SOC regions. In [42] and [43], a DP model is combined with a two-state thermal model to simulate battery electrical and thermal dynamics, which allows for real-time reflection of the thermal effect on model parameters and improves SOP estimation accuracy at varying temperatures. The authors assess the performance of the DP model with adaptive model parameters in SOC estimation, which yields a SOC error of less than 2% over the entire battery operating range, compared to 3% for the basic 1-RC model.

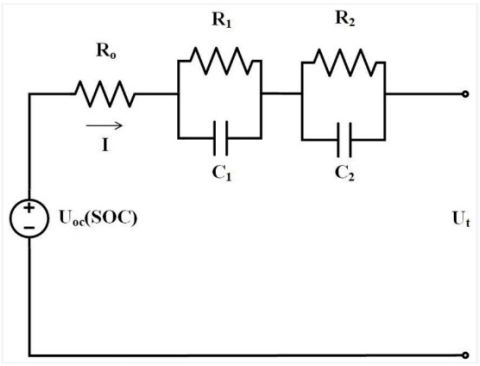

Figure 2.13: Dual Polarisation models[42] [43]

In [44], they suggest an enhanced fractional order model that uses two consecutive resistor-constant phase element networks to accurately reproduce the internal dynamics of a battery across a wide range of frequencies, as depicted in Figure 2.14. While this model's increased complexity improves accuracy, it is also costly to solve for peak discharge and charge current in real-time. To make the model more practical for real-world applications, they only consider the initial state within a memory horizon to affect the battery's electrical behavior at the end of a prediction window and ignore the other states in between. However, this approach may negatively impact the model's accuracy.

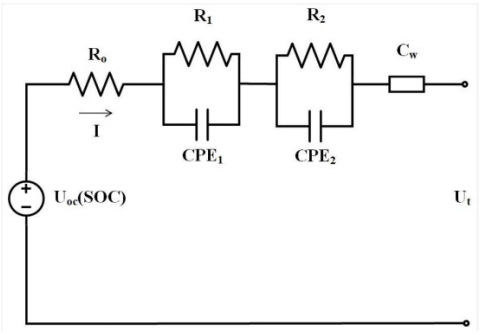

Figure 2.14: 2-RC fractional model with warburg element[44] [43]

Figure 2.15 depicts a full representation of an Equivalent Circuit Network that directly tracks the evolution of species within a cell [45]. This model incorporates complex electrochemical phenomena such as

changeable double layer capacitance, a full current-over potential relation, and over potentials caused by mass transport constraints, which are often removed from online battery performance predictors. The combined electrochemical and thermal model accounts for capacity loss due to a decrease in active species as well as power loss due to an increase in resistive solid electrolyte passivation layers on both electrodes. The model's ability to simulate cell behaviour during dynamic events is proven using traditional battery testing load cycles with current rates up to 20 C and realistic automotive drive cycles.

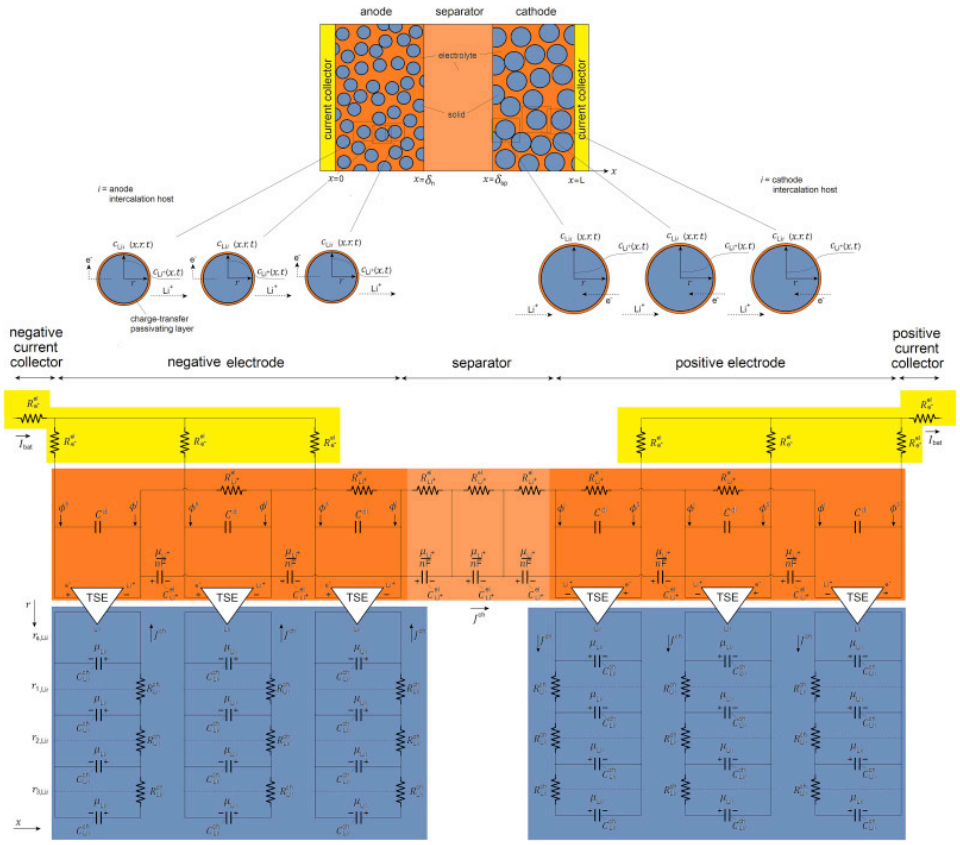

Figure 2.15: A 3 particle pseudo 2-D equivalent circuit network implementation.[45]

2.3.4. Physics based models (PBMs)

PBMs, also called as electrochemical models, are used to simulate the electrochemical and physical processes that occur in a battery. Doyle et al. [46] for the first PBM, which was based on the porous electrode model. The electrochemical model takes into account the internal electrochemical processes, heat transport, ionic diffusion, and other reactions in the battery. It describes the charge and discharge behaviour of lithium-ion batteries at the mechanism level using partial differential equations.

In the electrochemical battery models, pseudo two-dimensional (P2D) model [47], extended single particle (eSPM) model [48], [49] and single particle model(SPM) [50] are three commonly used models for battery performance simulation, but are proposed for different situations. Among them, P2D model has the ability to completely describe the micro-scale kinetics that occurs in a battery. However, due to its significant computational complexity, the application of the rigorous P2D model is very limited, especially for online applications [51]. SPM model and eSPM model can be regarded as approximate solutions for P2D model . These models and their simplified forms [52] [53] [54] [55] have been used in many applications.

Pseudo 2- Dimensional (P2D) Model

The presented model is based on the well-known Pseudo Two-Dimensional (P2D) model, which was originally proposed by Doyle et al. for describing the performance of a lithium anode/solid polymer separator/insertion cathode cell [47]. Fuller et al. subsequently utilized the porous electrode theory to

develop a model for a dual lithium ion insertion cell [56]. This model, referred to as Full Order Model (FOM), can calculate the internal electrochemical states of a cell by solving a group of four PDEs that are coupled by an algebraic closure term.The conductivity of the current collectors is large enough to assume that there are no significant changes at the current collector in the y and z spaces, thus the P2D model assumes the electro-chemical dynamics to be one dimensional [57], specifically the x direction. Small spherical solid particles are fused with the electrolyte to account for the mobility of lithium in both the solid and liquid (electrolyte) phases across one dimension. The variations in lithium concentration within these particles are calculated throughout the radial domain, where r is the particle's radial location. As a result, two dimensions are considered in the model dynamics: the x direction and the pseudo r direction, giving rise to the moniker pseudo 2-dimensional model. While a complete derivation, including boundary conditions, is available in the book of Plett (Chapter 3-4)[7], the equations themselves are outlined below. Figure 2.16a and fig. 2.16b illustrate the various variables within the cell that are employed in the model.

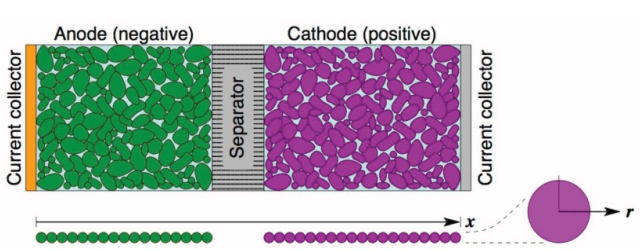

(a) P2D Porous-Electrode Model

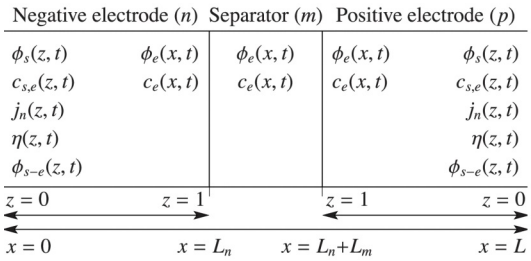

(b) Schematic diagram of Cell locations

Figure 2.16: Variables used to model a PBM [7]

1. **Solid-Phase Charge Conservation**

   The PDE describing charge conservation in the solid electrode particle matrix is

   $$\frac{\partial}{\partial x}\left(\sigma_{\text{eff}}\frac{\partial}{\partial x}\phi_s\right) = a_s j F \tag{2.3}$$

   where ϕ_s is the potential in the electrode solid active material as a function of position and time, σ_{eff} is the effective solid electronic conductivity, a_s is the specific interfacial surface area, j is the flux of lithium moving from the solid to the electrolyte as a function of position and time, and F is Faraday's constant. [58]

   The boundary condition is:
   At the interface of the current collector and the positive electrode, the charge flux is equal to the current density applied to the cell. A_{cell} is the current collector plate area of the cell.

   $$\begin{cases} \left(\sigma_{\text{eff}}\frac{\partial}{\partial x}\phi_s\right)|_{x=0} = I_{app}/A_{cell} \\ \left(\sigma_{\text{eff}}\frac{\partial}{\partial x}\phi_s\right)|_{x=L} = 0 \end{cases}$$

2. **Solid-Phase Mass Conservation**

   The PDE describing mass conservation due to diffusion in the solid is

   $$\frac{\partial c_s}{\partial t} = D_s\left(\frac{\partial^2 c_s}{\partial r^2} + \frac{2}{r}\frac{\partial c_s}{\partial r}\right) \tag{2.4}$$

   where c_s is the concentration of lithium in the electrode solid active material as a function of position and time, and D_s is the solid diffusivity [7]. The equation has a second order dependency with respect to the radial position inside the solid particle r

The boundary conditions of solid-phase mass conservation's are:
At surface of the particle, the flux is equal to the consuming rate of Li-ions due to electrochemical reaction occurring at solid/liquid interface (r=Rs).
At the center of the particle, there is no flux(r=0).

$$\begin{cases} \frac{\partial c_s}{\partial r} r = R_s = -\frac{j_{li}}{D_s} \\ \frac{\partial c_s}{\partial r} = |_{r=0} = 0 \end{cases}$$

The molar flux per electrode j_{li} is considered the input to the P2D model and Rs is the particle radius.

3. **Electrolyte-Phase Mass Conservation**

The PDE describing of mass conservation in the electrolyte is

$$\frac{\partial(\varepsilon_e c_e)}{\partial t} = \frac{\partial}{\partial x} D_{e,\text{eff}} \frac{\partial}{\partial x} c_e + a_s(1 - t_+^0) j_{li} \tag{2.5}$$

where c_e is the concentration of lithium in the electrolyte as a function of position and time,ε_e is the electrolyte volume fraction, and $D_{e,\text{eff}}$, is the effective electrolyte diffusivity [7].
The boundary conditions are:
At the two ends of the cell in x-direction, there is no mass flux, so,

$$\begin{cases} -D_e \frac{\partial c_e}{\partial x}|_{x=0} = 0 \\ -D_e \frac{\partial c_e}{\partial x}|_{x=L_p} = 0 \end{cases}$$

In the separator phase $(0_{sep} < x_{sep} < {}_{sep})$ ε = 1 and j = 0. It can also be seen that there is a second order dependency with respect to the horizontal spacial position x for the evolution of c_e, with time and the direct dependency on the input j.

4. **Electrolyte-Phase Charge Conservation**

The PDE describing charge conservation in the electrolyte is

$$\kappa_{\text{eff}} \frac{\partial}{\partial x} \phi_e = -a_s F j + \frac{2RT(t_+^0 - 1)}{F} \left(1 + \frac{\partial \ln f_\pm}{\partial \ln c_e}\right) \frac{\partial \ln c_e}{\partial x} \tag{2.6}$$

where ϕ_e is the potential in the electrolyte as a function of position and time,κ_{eff} is the effective electrolyte ionic conductivity, R is the universal gas constant, T is absolute temperature, t_+^0 is the transference number of the cation with respect to the solvent in the electrolyte, and $f_\pm$ is the mean molar activity coefficient of the electrolyte [7].

The boundary conditions are:
There is no charge flow in the liquid phase at the cell's end, but the potential in the solution phase and its flux are continuous at the electrode and separator interfaces.

$$\begin{cases} \kappa_{\text{eff}} \frac{\partial}{\partial x} \phi_e|_{x=0} = 0 \\ \kappa_{\text{eff}} \frac{\partial}{\partial x} \phi_e|_{x=L} = 0 \end{cases}$$

5. **Reaction Kinetics**

The Butler–Volmer equation describing reaction kinetics is

$$j_{li} = \frac{i_o}{F} \times \left(\exp\left(\frac{(1-\alpha_n)F}{RT}\eta\right) - \exp\left(\frac{-\alpha_p F}{RT}\eta\right)\right) \tag{2.7}$$

which is approximated to,

$$\eta = \frac{2RT}{F} \ln\left(\sqrt{\left(\frac{j_{li}}{2i_0}\right)^2} + 1 + \frac{j_{li}}{2i_0}\right) \tag{2.8}$$

where $i_o = Fk_s(C_{s,max} - C_{s,surf})^{1-\alpha}(C_{s,surf})^{1-\alpha}(\frac{C_e}{C_{e_0}})^{\alpha}$ denotes the reaction rate. α_n and α_p are the coupling coefficient of the charge transmission in the positive and negative electrodes. They are generally set to 0.5. η denotes the electrochemical reaction overpotential. The solid phase and liquid phase are coupled with the input J_{li} using the butler volmer kinetics.

Electrochemical reaction overpotential also follows the potential balance equation:

$$\eta = \phi_s - \phi_e - U_{ocp} - FR_{film}I_{app} \tag{2.9}$$

Thus there are 5 equation (2 mass transport, 2 charge transport and 1 Butler Volmer equation and 5 unknowns ($\phi_s, \phi_e, C_s, C_e, j$).

Single particle Model (SPM)

The microscale cell model consists of five coupled equations that describe lithium movement, potential, and reaction rate at the solid-electrolyte boundary. However, this model is too complex for control strategies or real-time applications. A lower order model called the Single particle model was developed to simplify the model. The diffusion of lithium inside solid particles is the slowest process, with its dynamic contribution dominating over others. [7][50]. The following assumptions are made to simplify the model:

- In SPM model, both electrodes are considered as spherical particles of active material with equal sizes, due to the fact that it is assumed that the current is uniformly distributed across all particles in the electrode.
- The reactions such as diffusion, transportation, diffusion induced stress will have uniform impact on each particle.[7]
- The dynamics of electrolyte concentration and potential are ignored. [7].

Due to the limitations that electrolyte concentrations are ignored, SPM models do not perform well at high charge/discharge rates [50]. To overcome this issue a new model called SMPe was developed, which has same dynamics as a SPM model with added electrolyte dynamics of a P2D model. The equations defined in SPMe model are explained in the section below. It is hybrid between the two models and performs relatively well at higher C-rates.

Electrolyte Enhanced Single Particle Model (SPMe)

As the major drawback of the SPM model discussed in 2.3.4, is its limitations to work only at low C-rates. The SPMe models takes care of this limitation. The major differences with a P2D model in terms of mathematical description are discussed below.

Solid Phase Dynamics

The PDE describing mass conservation in the solid is

$$\frac{\partial c_s}{\partial t} = \frac{1}{r^2}\frac{\partial}{\partial r}\left(D_s r^2 \frac{\partial c_s}{\partial r}\right) \tag{2.10}$$

where c_s is the concentration of lithium in the electrode solid active material as a function of position and time, and D_s is the temperature dependant solid diffusivity [58]. The major difference between the equation 3.2 is that only the second-order dependency is considered with respect to radial position.

The boundary conditions of solid-phase mass conservation's are:

$$\begin{cases} \frac{\partial C_s}{\partial r} r = R_s = -\frac{j_{Li}}{D_s} \\ \frac{\partial C_s}{\partial r} = |_{r=0} = 0 \end{cases}$$

where j_{Li} is the molar flux at the surface of the sphere at the solid-electrolyte interface.

Electrolyte Phase dynamics

The equations are same as explained in 2.3.4, with and approximation of equation 3.5 to the following

$$j_{li} = \frac{I_{app}}{F a_s L} \tag{2.11}$$

where, a_s = total surface area of particle/ total volume of particle

$$a_s = \varepsilon_s \frac{4\pi R_s^2}{\frac{4}{3}\pi R_s^3} = \frac{3\varepsilon_s}{R_s}$$

2.3.5. PB Model Comparison

Figure 2.17 shows the comparison of 3 performance models (SPM,SPMe and DFN). The simulation is run in pybamm [59] as a part of comparison study for 1 hour with a constant current. As discussed in earlier sections the DFN model is the most complex and accurate model of the three. Figure 2.17 and 2.18 show the snapshots of the change in variables at the halfway and end of the experiments. There is no change in electrolyte concentration in the SPM model as it is assumed to be constant. The SPMe model follows the same curve as the DFN model in electrolyte concentration variation. As this is a discharge cycle, Negative particle concentration drops as lithium ions are moving out of the negative electrode. Same logic applies for the negative electrode potential during the discharge cycle.

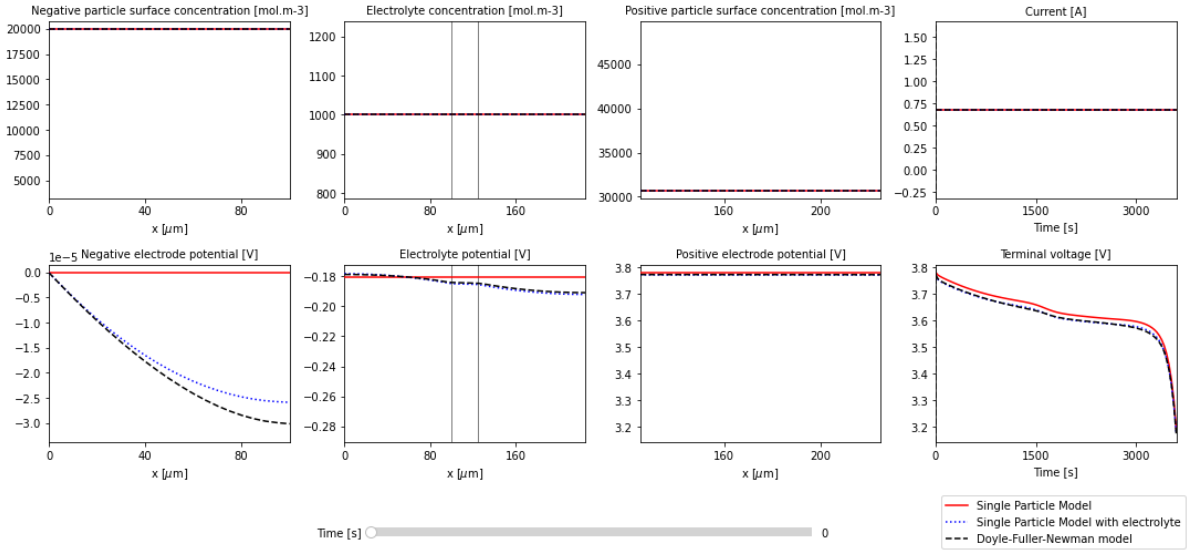

Figure 2.17: Comparison of three performance models

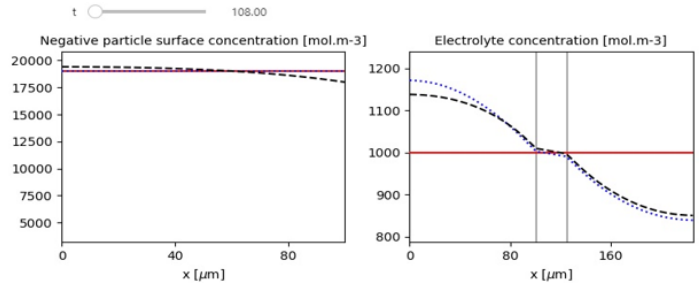

(a) start

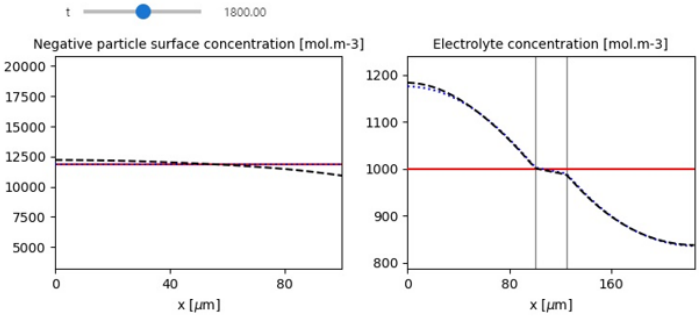

(b) Midway

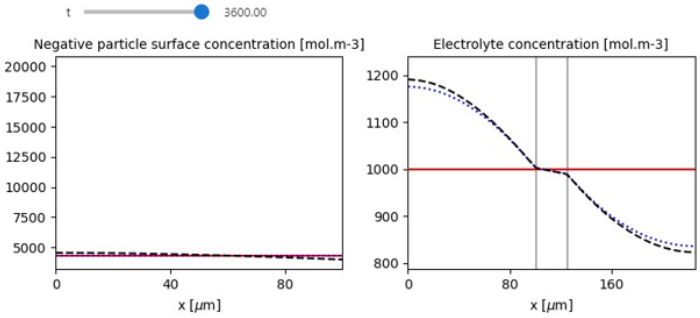

(c) end

Figure 2.18: Comparison of Negative particle surface concentration at various stages of the experiment

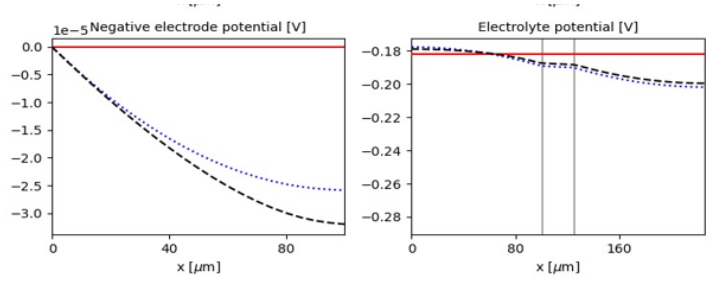

(a) start

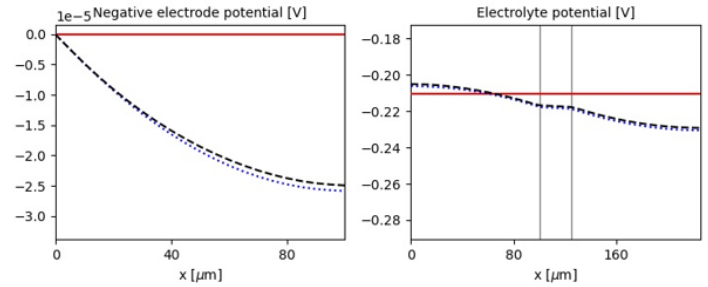

(b) Midway

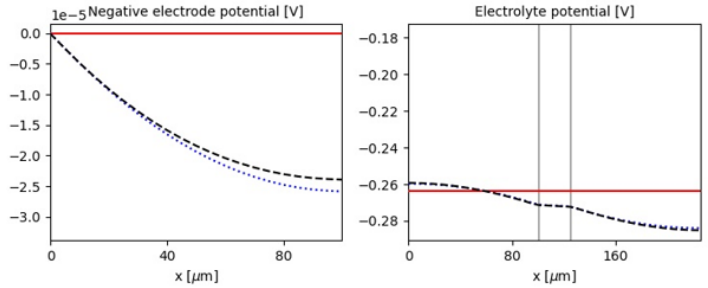

(c) end

Figure 2.19: Comparison of Negative electrode Potential at various stages of the experiment.

The SPMe model is highly accurate for various charge densities, as demonstrated by Luo and colleagues research [60]. They compared terminal voltage at multiple C-rates across the charging/discharging period to models. Figure 3.9 shows deviations between the three performance models for 1C, 3C, and 4C rates. The voltage profile shape is followed for both SP and SPMe models, with lines overlapping throughout the discharging period. The maximum deviation in the voltage profile is around 0.027 V, while the SP model deviates more from the P2D model, with a maximum deviation of around 0.003 V. At 3C discharge, the SP model fails to follow the P2D model, while the SPMe model follows it. At 4C, the SPM model fails to follow the same trajectory as P2D, proving that SPM models are highly inaccurate at higher C-rates.

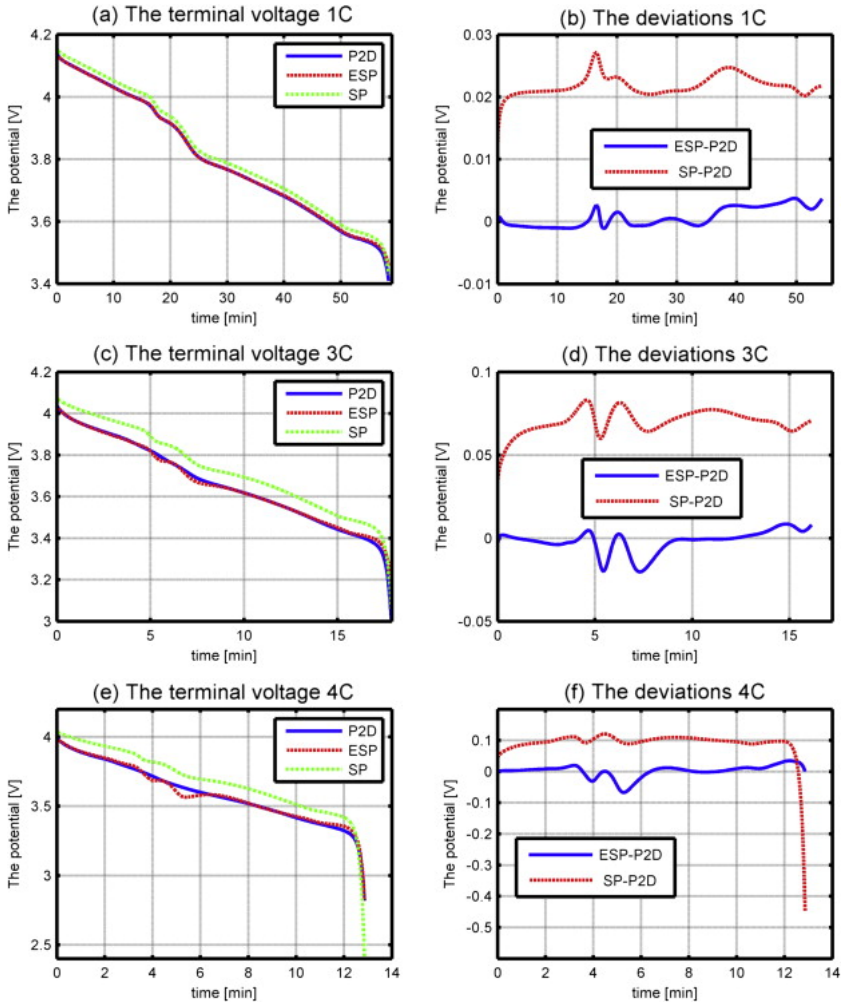

Figure 2.20: Comparison of terminal voltage profiles of three performance models P2D, SP(SPM),SPMe(ESP) at different C-rates [60]

Summary of performance modeling

In this section, the P2D. SPM and SPMe models have been presented in detail and compared with each other in terms of accuracy across a range of charge/discharge current densities,as well as the computational complexity of each model. For the P2D model, it was shown that while it has the highest accuracy, it cannot be used due to the high computational complexity, making it infeasible for real time control applications.The SPM and SPMe significantly lower computational time than the P2D model. Among SPM and SPMe, the SPMe showed the highest accuracy even at high C-rates. As a result, the best trade-off achieved between accuracy and computational complexity is the SPMe model. Even though SPMe model is accurate and fast compared to P2D also known as DFN model. It still cannot be used for real time applications as the equations are coupled and the simulation times are high enough. The model also requires considerable amount of memory to process which is not available in a processor of a BMS system of a car. or any other embedded-systems. Therefore, simplified reduced order model is discussed in in section 3.2, which converts the coupled ordinary difference equations into transfer functions which can be transformed into state space equations which are essential for real time estimation and tracking.

This thesis makes use of the SPMe model equations as a input for the Reduced order model discussed in Chapter 3.

3

Mathematical Modelling and Implementation

In this Chapter a process of modelling a LIB using a ROM is discussed. Section 3.1 discuses the flowchart of the thesis. Section 3.2 dwells into the process of modelling a ROM and converting the physics based performance model into state space model. Section 3.3 discusses the process to add 3 major aging mechanisms to the ROM. Lastly in section 3.4 Lumped thermal model is included to analyse the effect of cell temperature on various parameters.

3.1. Flowchart of the Thesis

This aim of this thesis is to build online estimators to estimate the SOH of a battery in real-time. These estimators,uses filtering techniques that requires the performance model and aging model in state space form. Thus the need to build a Reduced order Model (ROM), which is the final product an existing physics based performance model into linearised state space model.
The modeling process begins with selecting an appropriate PBM. The PBM acts as a validation for the results of ROM model. The PBM model used to validate are modelled in pybamm [59], which is an open source battery modeling platform. The discussion about the different PBMs based on accuracy and processing time is explained in Section 2.3.5. SPMe model was chosen as an input for the ROM. Then the model is transformed into state space model using the DRA process explained in Section 3.2. The output of the ROM are Current, Voltage, Temperature, SOC, Capacity. The ROM model used for this thesis work is adapted from work of G.L Plett [7]. Additional aging model is implemented based on the work by Xing Jin [8]. The equations provided by the Jin model are particularly chosen , as the model is simple to convert into linear state space model and only uses output states of the performance model (e.g -SOC, Voltage, Temperature, and Capacity AH) as input for calculating aging losses. A lumped thermal model is added to vary the temperature of the cell due to cyclic conditions based on the equations discussed in [29]
The final part of the thesis is to develop an estimators using filtering techniques that can estimate major aging mechanisms and predict the SOH and SOP of a LIB (explained in Chapter 4). These estimators are model based estimators as the input for the estimators are the noisy output from the ROM aging models. Experimental validation of a PBMs with aging is an complex process, which requires destructive methods to parameterise, 35 initial parameters required to model a PBM and few additional parameter's for the aging models. The aim of the thesis was to develop online estimators, and experimental validation would be an independent project on its own. Therefore, model based estimators are develop in this thesis work. Figure 3.1 shows the process flow of the thesis.

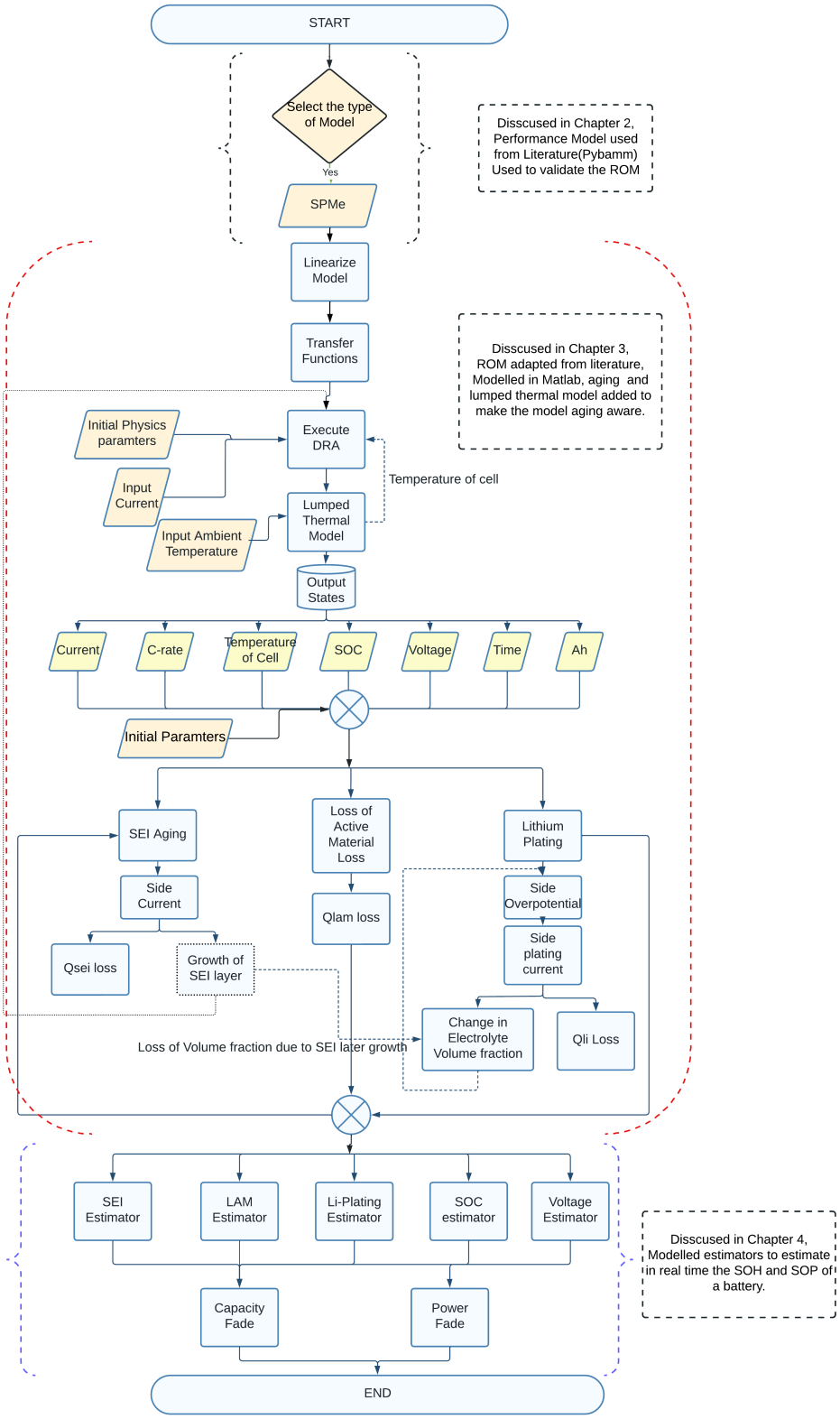

Figure 3.1: Flowchart of the Thesis

3.2. Reduced order models

The coupled PDE models developed in Chapter 2 are helpful for comprehending a cell's operation and may be used to investigate design elements that might be a performance constraint for the cell. With-

out having to construct several experimental cells, cell shapes, particle sizes, and material properties may be changed in simulation to optimize a cell's features. However, these models are too intricate for real-time battery management. They are, for instance, "infinite dimensional." There are an unlimited number of x- and r-dimensional variables for each point in time t that need to be solved. This means that for each x and r location, the values of $c_s(x, r, t)$, $c_e(x, t)$, $\phi_s(x, t)$, and $\phi_e(x, t)$ must be determined. Therefore, there is a need to create cell-level ODEs that retain as the fidelity of the continuum-scale PDEs, with their order reduced to finite space.

This section covers how to turn physics-based models into transfer functions, which are subsequently transformed into the state-space form using a realization procedure.

3.2.1. Linear state Space models overview

In this section, the process to generate Linear state space models is discussed. Figure , is flowchart showing the steps required to obtain a linear state space model.

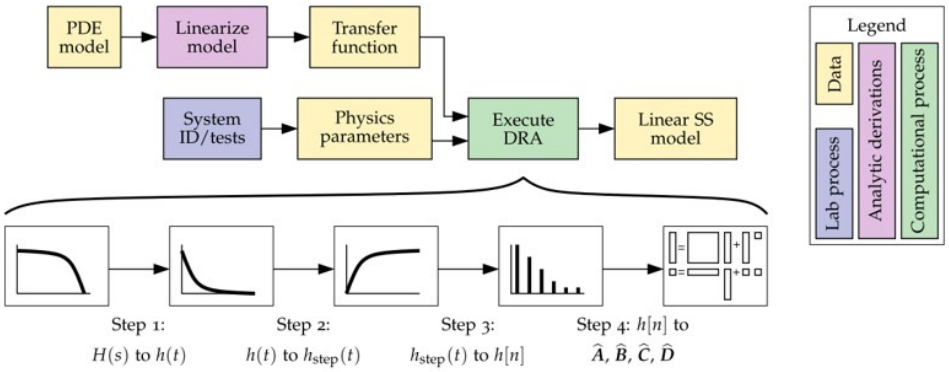

Figure 3.2: Depiction of Procedural steps used to compute linear state- space model [7]

The steps are as follows:

1. A PDE battery model is used as the first starting point. This thesis takes into account the SPMe model dynamics covered in Chapter 2. Fourier transform methods are used to linearize five nonlinear continuum equations into discrete time system models.
2. These discrete temporal models are then transformed into unique transfer functions.
3. Transfer functions are transformed into state space models, which may be used to real-time control, using the DRA (Discrete Realisation Algorithm) approach. In later portions of this chapter, the DRA procedure is covered.
4. The DRA procedure is independent of the kind of cell chemistry, and cell physics parameters are supplied to the DRA algorithm as needed.

Transfer functions

As discussed in 2.3.4, there are 5 equations that define the electro-chemistry of a cell(mass and charge transport in solid electrode, mass and charge transport in electrolyte and butler volmer equation that couples the solid phase and liquid phase kinetics). The 5 unknowns are ($\phi_s, \phi_e, C_s, C_e, j$). The input to the cell is the current I_{app}. Therefore, all the 5 unknown variables should have transfer functions that relates to the applied current I_{app}. The derivation of the transfer functions is beyond the scope of this report and the detailed derivations can be found in the book [7] chapter 5 and 6, which is the basis of this reduced order model used in this thesis. The equations can be found in Appendix A.4.
These 5 transfer functions can be combined into a single input (I_{app}) multiple output response array, which is the basis input for a DRA process as seen in fig. 3.2.

3.3. DRA process

Given a (possibly single-input multi output) continuous-time transfer function H(s) in the Laplace domain such that Y(s) = H(s)U(s), and a sampling period, T_s, the resultant state space realization is,

$$x[k+1] = \tilde{A}x[k] + \tilde{B}u[k] \tag{3.1}$$

$$y[k] = \tilde{C}x[k] + \tilde{D}u[k] \tag{3.2}$$

In the context of the reduced order models U(s) is the input current I_{app} and the output matrix, is given by

$$H(s) = \begin{bmatrix} \frac{C_{e,k}(x,s))}{I_{app}(s)} \\ \frac{\phi_s(z,s)}{I_{app}(s)} \\ \frac{\phi_e(z,s)}{I_{app}} \\ \frac{\tilde{C}_{s,e}(z,s)}{I_{app}} \\ \frac{J(z,s)}{I_{app}(s)} \end{bmatrix} \tag{3.3}$$

where 'k'is the sampling instant. In this formulation, e.q 3.1 captures the dynamics of the system, and e.q 3.2 describes the linearized system output .

3.3.1. Ho−Kalman algorithm and Hankel matrices

Before, the DRA process is discussed it is necessary to have a understanding of the Ho-kalman algorithm [61]. A discrete ,unit-pulse response of a given linear state-space system g in the discrete time-domain can be expressed as

$$g_k = \begin{cases} D, k = 0 \\ CA^{k-1}B, k = 1, 2, 3... \end{cases}$$

where A, B, C, D are state space matrices and D is gathered from the system response at time step zero.The resultant transfer function response can be formulated into a block Hankel matrix [7] of Markov parameters.
The block hankel matrices corresponds to a subset domain of discrete-time impulse responses.

$$\mathscr{H}_{k,m} = \begin{bmatrix} g_1 & g_2 & g_3 & \cdots & g_m \\ g_2 & g_3 & g_4 & \cdots & g_{m+1} \\ g_3 & g_4 & g_5 & \cdots & g_{m+1} \\ \vdots & \vdots & \vdots & \ddots & g_{m+1} \\ g_k & g_{k+1} & g_{k+2} & \cdots & g_{m+k-1} \end{bmatrix}$$

The block hankel matrices also follows, the relationship of

$$\mathscr{H}_{k,m} = \mathscr{O}\mathscr{C}$$

where $\mathscr{O}$ is the observability matrix and $\mathscr{C}$ is the controllability matrix.

$$\mathscr{O} = \begin{bmatrix} C \\ CA \\ CA^2 \\ \vdots \\ CA^{k-1} \end{bmatrix}$$

and

$$\mathscr{C} = \begin{bmatrix} B & AB & A^2B & \cdots & A^{m-1}B \end{bmatrix}$$

The final state space representations are then calculated via

$$\tilde{A} = \mathscr{O}^{+}\mathscr{H}_{k,m+1}\mathscr{C}^{+}$$

$$\tilde{B} = \mathscr{C}[1:n, 1:m]$$

$$\tilde{C} = \mathscr{O}[1:p, 1:n]$$

where n and p are the state-space output size and $\mathscr{H}_{k,m+1}$ denotes the forward shift of block Hankel matrix.

DRA steps

The four steps in DRA process followed by the book of Plett [7] are summarized below,

- STEP1: To obtain an approximation to the continuous-time impulse response h(t), sample the continuous-time transfer function H(s) in the frequency domain at a high rate and perform the inverse discrete Fourier transform (IDFT) on the samples.
- STEP2: Use h(t) to approximate the continuous-time step response h step(t), also sampled at the high rate.
- STEP3: Compute the discrete-time unit-pulse response values g_k with inter-sample period T_s from the continuous-time step response h step(t), assuming a sample and hold circuit connected to the system input.
- STEP4: Generate a discrete-time state-space realization using the deterministic Ho–Kalman algorithm. This algorithm returns the reduced order A, B, and C matrices from the discrete-time unit pulse response sequence in Step 3. The order of the system is determined from the ordered singular values of the Hankel matrix computed as part of the algorithm. The D matrix is found by the initial value theorem.

A detailed explanation of each step can be found in [7] chapter 5.

3.4. Aging Models

Until now, the report discussed physics based performance model of a Li-ion battery. The state space equations achieved via reduced order models provide ideal states and do not consider any degradation. In real life cells degrade with time and usage and the aging is non-linear. Therefore to calculate the SOH of a battery it is necessary to include degradation mechanisms.

Figure 3.3, shows the state space visualisation of the battery model with aging. Here the upper loop is the state space representation of the performance model where, the States and the outputs are a function of θ and the input k .The aging model is represented as a function of θ. the changes in the aging model are send an feedback to the performance model to update the states. Real systems have noise in them and are processed in the system itself to give noisy output. The use of Filters kF_x and KF_θ are discussed in detailed in Chapter 4

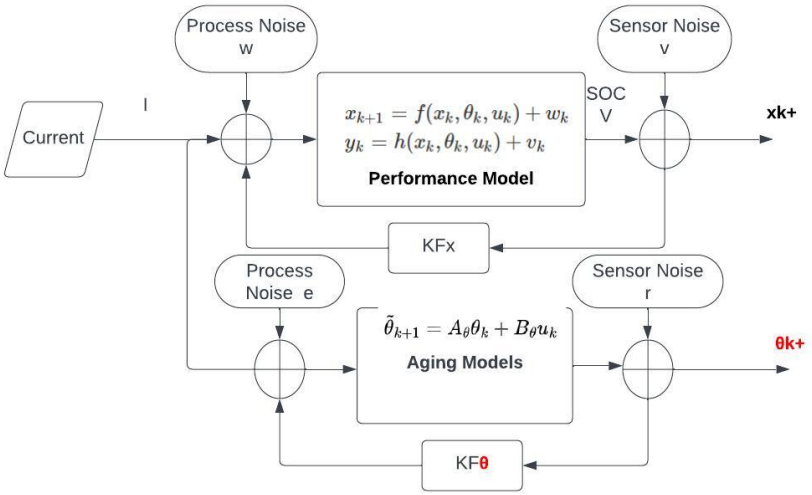

Figure 3.3: State space visualization of battery modeling

The three dominant degradation mechanisms that affect battery aging are (1) SEI layer Growth (2) Lithium Plating (3) Loss of active material. The degradation models used in this report are based on

the studies conducted by [8],[9] and [62].

3.4.1. SEI layer formation sub-model

It is commonly acknowledged that the SEI layer formation on the anode is one of the primary causes of capacity loss for a cell with a carbon or graphite-based anode [62]. The generalised side reaction at the graphite/SEI interface is represented as follows:

$$S + 2e^- + 2Li^+ + 2e^- \rightleftharpoons P \tag{3.4}$$

where P is the reduction by-product that creates the SEI layer and S is the solvent reactant.

The porosity of the SEI film is rather high. Despite the fact that it contributes an ionic resistivity R_film that enhances cell resistance, lithium may still enter and exit the particle via the film. Furthermore, as solvent diffuses through the layer during charge, the SEI layer continues to slowly increase, despite the fact that the film makes it more difficult for solvent to reach the particle surface and form further SEI since there is adequate porosity for some solvent to flow through. Furthermore, lithium intercalation into the graphite negative electrode causes the lattice volume to grow, extending and finally fracturing the SEI layer and exposing more active material to the electrolyte as seen in fig 3.4

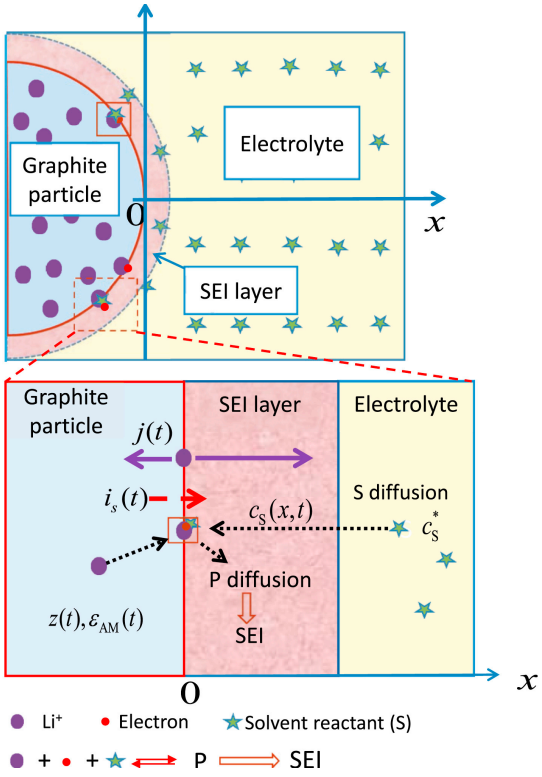

Figure 3.4: Schematic diagram of SEI layer formation on the graphite electrode [62]

The rate of side reaction current growth is proportional to the rate of SEI layer growth or capacity loss caused by Q_sei layer expansion. Because the products are a mixture of numerous species, averaged mass and density constants are utilised to study the creation and evolution of the SEI film. According to this model [8], SEI layer creation is irreversible in nature, and so the SEI layer grows with each cycle. Furthermore, SEI layer development is solely taken into account on the graphite electrode. The cathode's side effects are ignored.

SEI layer formation is related to the side reaction current density, i_st via the equation .

$$Q_{sei} = \int i_{st} A_{cell} dt \tag{3.5}$$

$i_s t$ is calculated as

$$i_{st} = \frac{K_{sei} * e^{\frac{-E_{sei}}{RT}}}{2(1 + \lambda\theta_{sei})\sqrt{t}} \tag{3.6}$$

where λ

$$\lambda = \frac{c_s\sqrt{D_s}}{c_p\sqrt{D_p}}$$

$$\theta_{sei} = exp[\frac{n_{sei}F}{RT}(\eta_k + U_n^{OCP} - U_s^{OCP})]$$

, where U_n^{OCP} is a function of SOC, while U_s^{OCP} is set to be 0.4 V against Li/Li+.

Kinetic overpotential is calculated via,

$$\eta_k = \frac{2RT}{F} sinh^{-1} \frac{I_{app}}{2a_s A_{cell} L_n i_o} \tag{3.7}$$

The $\sqrt{t}$ in the denominator, denotes that SEI layer growth is much higher for a fresh battery than an aged battery.According to [9], the SEI layer that has already developed on the electrode tends to passivate the electrode against further layer formation. A little amount of electrolyte can still seep over the SEI layer, react at the surface of the electrode material, and produce fresh SEI layer due to the porous nature of the SEI film. A decreased rate of SEI layer production will result from the continually expanding SEI layer because it will slow down electrolyte solvent migration across it to the active material/SEI layer interface [9]. The rate of SEI layer thickness growth is given by,

$$\frac{\delta_{\text{SEI}}}{dt} = \frac{i_{st} M_{sei}}{2F\rho_{sei}} \tag{3.8}$$

where ρ_{sei} [kg m3] is the average density of the constituent compounds and M_{sei} [kg mol] is the average molecular weight of the SEI layer's constituent chemicals. This makes it possible to determine the entire film resistance as,

$$R_{film} = \frac{\delta_{sei}}{k_p} \tag{3.9}$$

, where k_p is the conductivity of the SEI film and δ_{sei} is SEI layer formed due to SEI side current.

Table 3.1: Parameters used for SEI degradation Modelling [9]

Parameter	Units	Value
K_{sei}	$\frac{1}{\sqrt{s}}$	6684.8
E_{sei}	$\frac{J}{mol}$	39146
i_o	$\frac{A}{m^2}$	0.05
λ	unitless	5.51 e-5
k_p	unitless	2.00E-06
M_{sei}	$\frac{kg}{mol}$	0.162
ρ_{sei}	$\frac{kg}{m^3}$	1690

3.4.2. Active Material Loss SUB-model(LAM)

Another significant process of degradation that has been noted in experimental research is active material loss [63]. According to [63], [64], mechanical stress caused by lithium intercalation inside the active material particles may also lead to electrode particle breakage or structural degradation, which may eventually cause the active material to be lost or isolated. According to [62],[9] the rate of lithium loss because the active material is isolated is represented as,

$$\frac{dQ_{Li,loss}}{dt} = \frac{d\varepsilon_{am}}{dt}.V.z.c_{Li,max} \tag{3.10}$$

, where,

$$\frac{d\varepsilon_{am}}{dt} = -k(t)|I_{app}| \tag{3.11}$$

, and

$$k(t) = k_{am}^{0} exp(\frac{-E_{am}}{RT}) \tag{3.12}$$

, where $z = \frac{c_{li}}{c_{li,max}}$ or $z = SOC.(z_{100\%} - z_{0\%}) + z_0$. $z_{100\%}$ refers to SOC at 100% and z_0 refers to SOC at 0%.

At the start, or in case of a new cell, the total lithium inventory is given by,

$$Q_{li,0} = \int_0^t \varepsilon_{am,0}.V.z_{100\%}.C_{li,max}dt \tag{3.13}$$

The percentage of capacity loss due to active material loss is given by,

$$Q_{am} = \frac{Q_{li,loss}}{Q_{li,0}} = \int_0^t k_{am} exp(\frac{-E_{am}}{RT}).SOC.|I_{app}|dt \tag{3.14}$$

. Here, $SOC.I_{app}$ depicts the total lithium available at any given instance.

Table 3.2: Parameter's used for LAM degradation Modelling [9]

Parameters	Units	Value
K_{am}	$\frac{1}{\sqrt{s}}$	0.0137
E_{am}	$\frac{J}{mol}$	39500

3.4.3. Lithium Plating sub model

Lithium plating is not regarded as a prominent degrading process since it occurs seldom, in contrast to SEI layer development caused by cell manufacturer-specified terminal voltage restrictions. However, cell terminal voltage is a poor predictor of internal potentials, especially at low temperatures or when charging at high C-rates, and can result in lithium plating. In the present model, both SEI formation and lithium plating are viewed as anode side reactions. Thus, as shown in Fig 3.5 , a total of three electrochemical processes may take place in the anode [32].

- Main intercalation reaction of lithium ions into the graphite electrode during charging/discharging.
  $C_6 + Li^+ e^- \leftrightarrow LiC_6$
- The side reaction causes fresh SEI to increase as a result of the electrolyte solvent diffusing over the surface layer.
  $S + 2e^- + 2Li^+ + 2e^- \rightleftharpoons P$
- If the local anode potential becomes negative (with respect to pure Li electrode), lithium deposition would occur.
  $Li^+ e^- \leftrightarrow Li(s)$

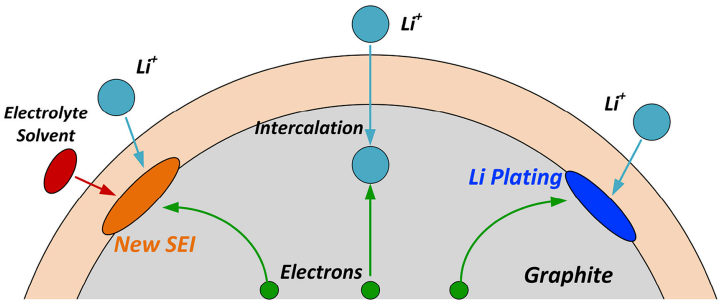

Figure 3.5: Schematic diagram of electrochemical reactions occurring at the anode during cell charging [32]

The overportential due to side reaction is given by,

$$\eta_s(x,t) = \phi_s(x,t) - \phi_e(x,t) - U_{li}^{OCP} - FR_{film}.j_{tot}(x,t) \tag{3.15}$$

where total current density is given by
$J_{tot} = j_{app} + j_{sei} + j_{li}$.
The side reaction for lithium plating only occurs at spatial locations in the negative electrode where $\eta_s(x,t) < 0$ from $x = x_0$ to $x = L_n$. Refer fig 2.16b for cell locations.The local side-reaction overpotential of a lithium-ion cell diminishes over time as it is being charged. It is not constant across the electrode; rather, the value close to the separator tends to fall more quickly than at other points. Additionally, it demonstrates that plating does not require a cell to be at 100% SOC. SOC is therefore only one important variable; whether plating takes place is ultimately determined by the local overpotential as shown in fig 3.6[7].

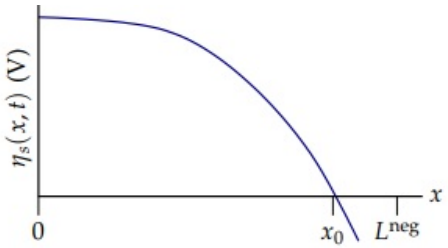

Figure 3.6: Schematic illustrating overpotential during charge across the negative electrode [7]

Lithium plating does not occur during discharge as most of the side reaction happens only at negative electrode(anode). We neglect side reactions at cathode as anode aging is the most dominant part of cell aging. So side reaction overpotential is always greater than zero during discharge. Even if reversible aging is considered, the consumed Li which forms product layer on anode releases its Li+ ions during discharge, which increases the overall overpotential during discharge phase.

In this report the model used by [62] is used to calculate Li-plating. The reason for choosing this model is that it only requires output states of the reduced order model to calculate aging, and does not require to make changes in the initial transfer functions of the reduced order model.

the capacity loss due to lithium plating is given by,

$$Q_{li,loss} = \int_0^t j_{li} A_{cell} dt \tag{3.16}$$

, where,the lithium deposition reaction current is given by,

$$j_{li} = a_s i_{0,li} exp[\frac{-\alpha_{li} F}{RT} \eta_{li}(x,t)] \tag{3.17}$$

to calculate J_{li}, the overportential during charging is given by,

$$\eta_{li}(L_n,t) = \frac{I_{app} L_n}{2\sigma^{eff} A_{cell}} - \frac{E(t)}{3} L_n^2 + \frac{2RT}{F} sinh^{-1} \frac{I_{app}}{2a_s A_{cell} L_n i_o} + U_n^{OCP} \tag{3.18}$$

where, E(t) is a intermediate variable given by,

$$E(t) = -[\frac{k_D^{eff}}{c_e} \frac{\beta\epsilon_e - (1 - t_o^+)}{D_e^{eff} F} + 1] \frac{I_{app}(t)}{K^{eff} A_{cell} L_n} \tag{3.19}$$

The degradation due to SEI layer growth calculated as an output in e.q 4.4.1and Li-plating are interrelated by the equation,

$$\frac{d\varepsilon_e}{dt} = -a_s \frac{d\delta_{sei}}{dt} \tag{3.20}$$

As the SEI layer thickness increases, the electrolyte volume fraction ε_e drops and lowers the $\eta_{li}(L_n,t)$ in process. Therefore, a increase in SEI layer is favourable for Li-plating to occur easily. The detailed derivation of these equations can be found in [8].

3.4.4. Results of variation of C-rates with CC charging

The aging models were simulated at various C-rates during the fast Charging of a new NMC cell at various C-rates as seen in Figure 3.7 and 3.9. The cell is charged from 0% SOC to 100% SOC. In figure 3.7 SEI aging does not start from zero. This is due to the fact that for SEI layer formation is highest at high SOC, as there are more lithium ions to form side reactions. Starting from an completely discharged cell, it takes some time till there are enough Li-ions for the side reaction to take place. This is also seen in figure 3.8 where the side reaction current for a completely discharged cell while charging (a) in comparison to the SEI side current during a discharge cycle (b).

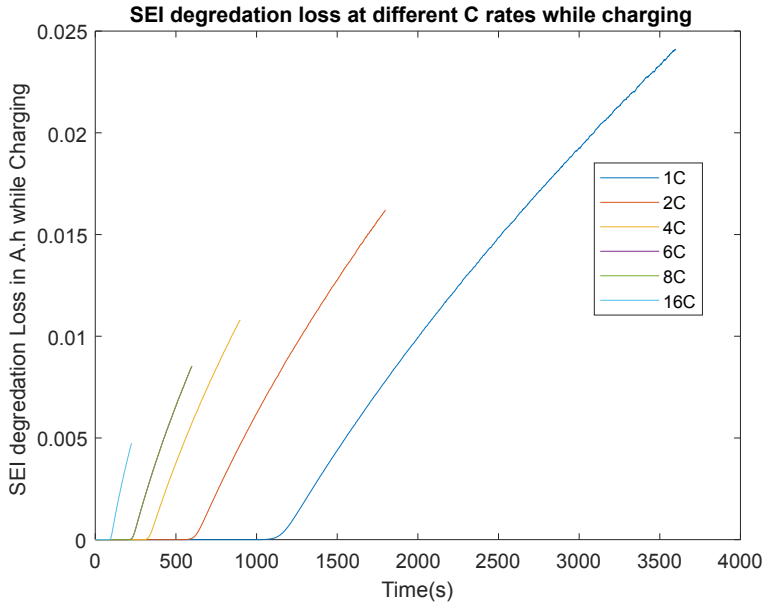

Figure 3.7: Comparison SEI loss with different C-rates for CC charging

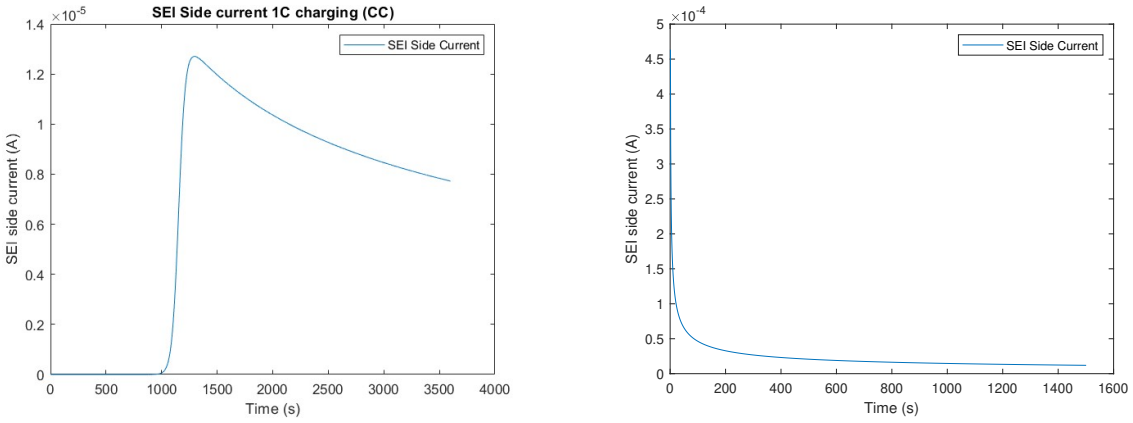

(a) Side reaction current i_{st} for a fully discharged cell during charging

(b) Side reaction current i_{st} for a fully charged cell during discharging

Figure 3.8: Side reaction current i_{st} comparison

The loss of capacity due to LAM is same irrespective of different C-rates as depicted in Fig 3.9 (a). The faster the C-rate of charging the shorter the charging time. For loss of capacity due to LIP aging is shown in fig 3.9 (b), a semi-log scale is used for the y-axis, as the rate of degradation's are very high for 4C compared to 1C and cannot be compared on a normal scale. Finally in fig 3.9 (c) the Capacity fade of the cell is shown at different C-rates. As expected the cell degrades faster at higher C-rates.

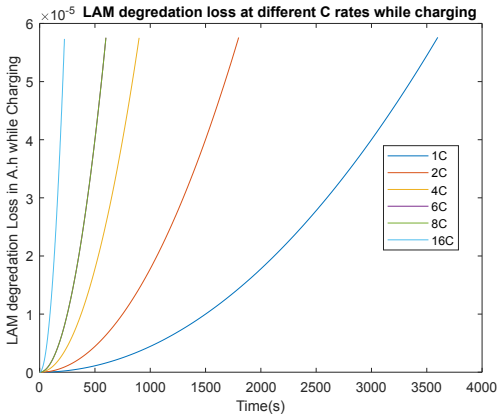

(a) Comparison LAM loss with different C-rates for CC charging

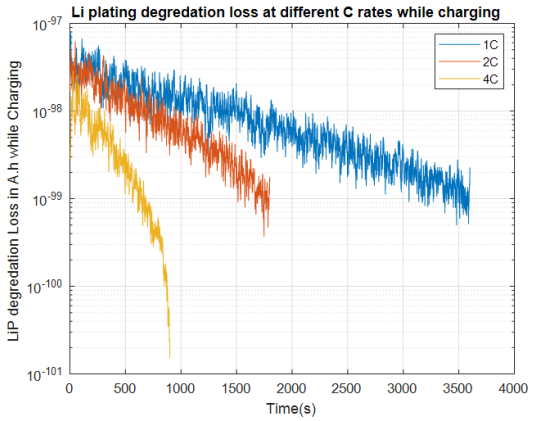

(b) Comparison LIP loss with different C-rates for CC charging

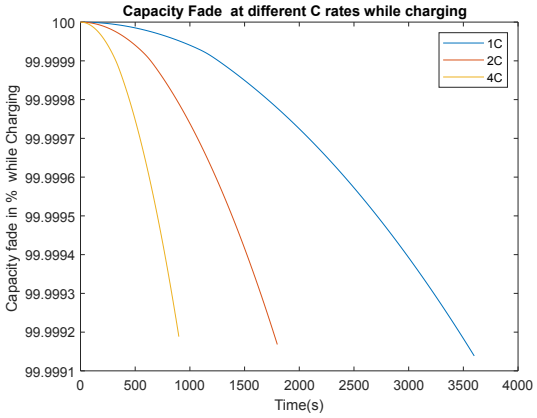

(c) Comparison SOH with different C-rates for CC charging

Figure 3.9: Comparison of effects of C-rates while CC charging

Variation of C-rates during discharge

Figure 3.10 shows the effect of C-rates on aging characteristics during a 1 UUDS discharge cycle for a NMC cell. The general trend is followed where, higher C-rates causes faster Capacity loss of the cell.

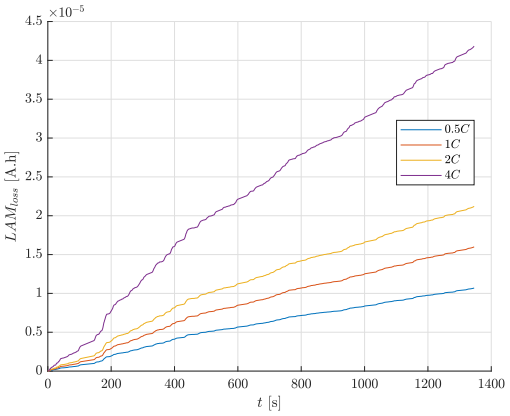

(a) Variation of LAM Loss with different C-rates

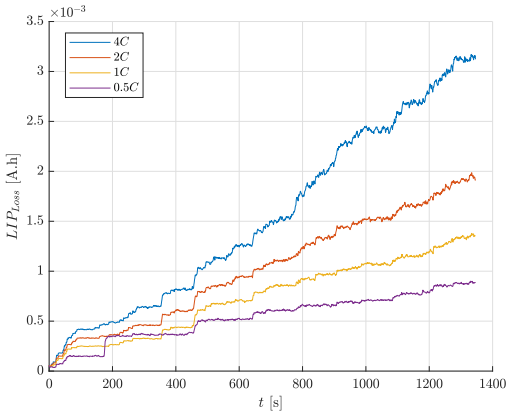

(b) Variation of LIP Loss with different C-rates

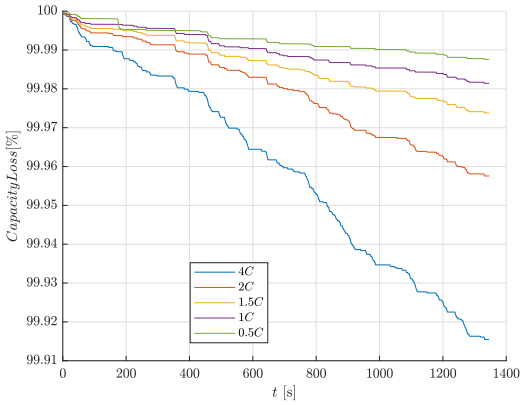

(c) Variation of Capacity loss with different C-rates

Figure 3.10: Effect of C-rates on the aging models

3.5. Lumped Thermal Model

Until now all the modeling was assumed at constant temperature. In a real application thermal effects play a major role in cell degradation and must be taken seriously. A lumped thermal model is described by the following energy balance equation:

$$\rho A_{cell} C_p \frac{dT}{dt} = i^2 R_{tot} + i(\eta_n - \eta_p) + i.T.\frac{\partial U}{\partial t} - hA_{cell}(T - T_{amb}) \tag{3.21}$$

, where, $\rho A_{cell} C_p \frac{dT}{dt}$ is the total heat generated in the cell, which leads to the rise in temperature. $i^2 R_{tot}$ is ohmic heat generated per unit volume due to contact resistance between the electrodes and the current collectors. The second term $i(\eta_n - \eta_p)$ is the reaction heat generated due to change in over potentials. $i.T.\frac{\partial U}{\partial t}$ is the reversible heat generation due to entropy change in the active material of electrodes during intercalation/de-intercalation of lithium. It is also defined as the change in SOC of the cell. This term is usually very small, as the rate of change in SOC or entropy change is very small and is neglected for this model. the last term is the rate of convective heat removal from the cell. The convective heat transfer co-efficient h defines the rate of cooling applied to the battery and is usually an control state to the BMS system.

Temperature dependence of model parameters is crucial in understanding the physical and chemical characteristics of cells during high C-rate operation. The electrolyte diffusivity and conductivity temperature dependencies are obtained from [65], with temperature significantly impacting reaction kinetics constant k_i and solid phase diffusion coefficient D_i. An Arrhenius' law temperature dependency is a typical strategy.

$$k_i = k_i^{ref} exp\left[\frac{E_k}{R}\left(\frac{1}{T} - \frac{1}{T_{amb}}\right)\right] \tag{3.22}$$

$$D_i = D_i^{ref} exp\left[\frac{E_D}{R}\left(\frac{1}{T} - \frac{1}{T_{amb}}\right)\right] \tag{3.23}$$

Thermal models are also crucial in pack level model to understand the cell-to cell temperature variations.

Table 3.3: Parameters used for Temperature Modelling

Parameter	Units	Value
ρ	kg m-3	2107
C_p	J/ kg K	1172
k_t	W/m K	0.4
h	W m-2	10

Figure 3.11(a) shows the temperature profile of a NMC cell for 1 UDDS discharge cycle. and Figure 3.11 (b) shows the variation of C-rates on the temperature rise in a NMC cell. There is a major jump in temperature 2C to 4C discharging, while the temperature does not rise a lot during low C-rates.

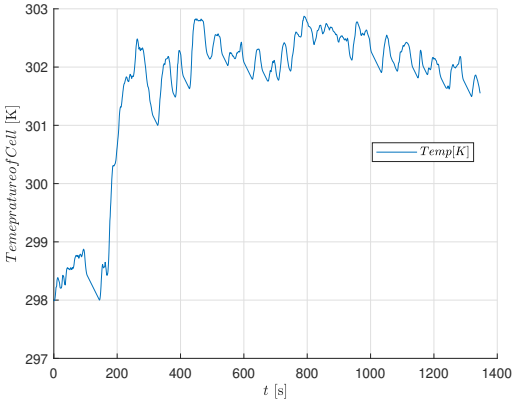

(a) Temperature of a NMC cell during 1 UDDS discharge cycle

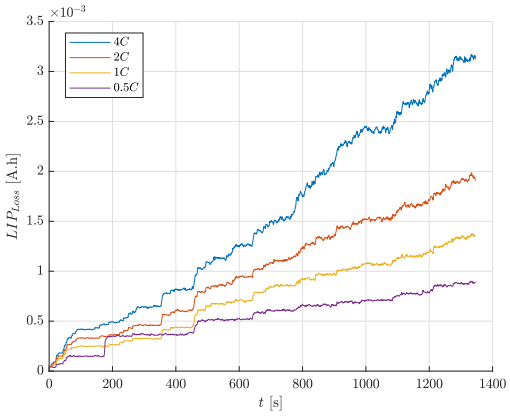

(b) Effect of C-rates on the temperature of a NMC cell during 1 UDDS discharge cycle

Figure 3.11: Effect of C-rates on the lumped thermal model

3.6. Summary

This chapter begin with the the explanation of the flow of the thesis. Then the process of converting a ROM into state space model is explained, followed by explanation of the aging models and the lumped thermal model used to build a complete model of a Lithium ion cell. The model of the cell build in this chapter acts a input for the estimators discussed in chapter 4.

4

Online state estimators

Chapter 2 describes the modelling approaches and Chapter 3 explained the methods to model a reduced order model with main degradation mechanisms. This chapter uses the model developed as input to develop an algorithm to estimate the states of the battery in real time. Section 4.1 discusses the need for real time estimation, followed by a review of different online estimation methods available in literature. Section 3.1 explains the flow of the thesis in detail. The further sections then explains the various estimators in detail.

4.1. Need for real time estimation

In previous chapters, the report discussed a reduced-order model able to predict the internal variables of a cell in addition to its voltage.This paradigm is particularly suited for implementation in a microcontroller since allocation processing power and memory space is low. To assist in computing cell SOC, SOH, available energy and power, and other metrics, we may think about employing this ROM directly in a BMS or any other online estimators. But before the ROM predictions can be regarded as precise and relevant, deployment in a real-world application brings several additional factors that need to be handled. It must be specifically acknowledged that the models were created using flawed assumptions and that it must take into account various aspects of the battery system as a whole in which the cell functions.

The generic form of a linear state space model is given by,

$$x_{k+1} = A_k x_k + B_k u_k + w_k$$
$$y_k = C_k x_k + D_k u_k + v_k$$

where, x_k is the state of the system and y_k is the output. A, B, C, D are the values of the matrices of the state space. Given this model several issues arise while trying to implement it:

- **Cell to cell variations**
  Even those built by the same firm or utilising the same type of battery differ slightly. Because manufacturing procedures are never perfect, the completed product frequently contains material and assembly inhomogeneities. This effect may appear insignificant, but when the initial total-capacity dispersion across cells is considered, it can be demonstrated that there are significant differences between the predictions of voltage and internal electrochemical variables and the actual cell behaviours. As a result, the model may not hold true for a group of cells and may produce inaccurate findings. In terms of state space variables, the derived A, B, C, D matrix may differ between cells since states might change depending on the initial conditions.
- **ROMs and degradation models are not perfect**
  The transfer functions used in the ROM model are very precise approximations of the primary models, but they are still approximations. THE DRA method is not without restrictions, and the linerisation of non-linear connections generates certain inaccuracies. The thermal model employed is a one-dimensional average estimate of the temperature within the cell. Because of linearisation and assumptions made when simplifying the models, the values of the state space

matrices estimated via modelling may differ from the true values in the context of state space models.

- **Errors in inputs**
  The current and internal temperature sensors can have measurement noise and this error propagate throughout the model and can amplify the error in the final results. The error in system is processed as an input in every iteration and causes the values of the outputs to changes based on the noise in the system.

All these factors mentioned above create a need to have a method that can reduce this errors and adapt with changing initial conditions. Filtering is a method that deals with error reduction and correction. This chapter discusses the most popular of these filters called kalman filters in detail. The report makes use of the Kalman filter and its variants to predict in real time the states of the battery.

4.2. Different estimators in literature

The current battery's ability to produce a certain performance in comparison to its capacity to do so when it was in its initial state is known as SOH. According to the equation below [66], the battery SOH is calculated by dividing the current capacity by the nominal capacity;

$$SOH = \frac{Q_{act}}{Q_{nom}}$$

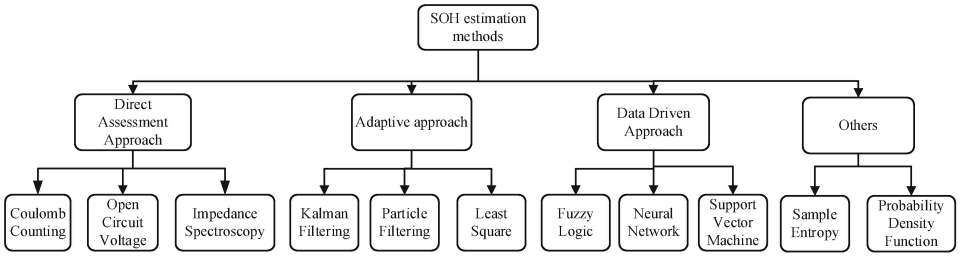

Figure 4.1: Classification Of SOH estimation methods [1]

Direct assessment approach

Coulomb counting

The coulomb counting (CC) method is used to calculate the SOC of the battery. Instead of providing an absolute SOC, coulomb counting provides a relative change in SOC. The amount of Ah that have left or been received by the battery may be measured by measuring the current over a specific time step.

$$SOC_t = SOC_{t-1} + \frac{\eta I(t)}{Q_n}\Delta t \tag{4.1}$$

By dividing the discharge value by the rated capacity, the coulomb counting method is utilised to calculate battery SOH. DOD, or depth of discharge, is used to calculate the amount of charge discharged in relation to the battery's rated capacity. In each charge and discharge cycle, charging and discharging efficiency compensate for DOD, while re calibration eliminates accumulated impacts. CC consumes little power but has a large estimate inaccuracy of roughly 10% [1].

OCV based estimation

OCV-based SOH estimation method can be performed online and offline, with extensive laboratory tests examining the relationship between SOH and OCV. Guo et al. [67] monitored charging curves to evaluate capacity fade, and the electrochemical model (ECM) and constant current-constant voltage charging method assessed SOH using transformation function and non-linear least square method. The estimation error of SOH at all stages of life is under 3%.

Impedance spectroscopy method

This is an experimental method of calculating SOH.Impedance spectroscopy is used to estimate SOH using wide frequency spectrum. ECM parameters are computed using 16 parameters, and particle swarm optimization (PSO) is used to determine parameters[68].

Data driven methods

Fuzzy logic processes complex and nonlinear systems using a fuzzy rule set, divided into crisp and fuzzy sets. Crisp sets assign specific values, while fuzzy sets categorize uncertainty. Accurate prediction of system health (SOH) relies on selecting the appropriate membership function (MF).Detailed information can be found in [69].

Neural network (NN) is a robust algorithm for predicting SOH in complex non-linear systems, requiring minimal battery characteristics information. However, high computational cost is a drawback [70].

4.3. Adaptive filters

Kalman filters are based on a framework named 'sequential probabilistic inference'[58]. Using a model of the system being described and feedback of the real response of that system, the filters adjust the internal states of the model to make the predictions converge to better results.An effective approach that can precisely predict battery SOH is the Kalman filter (KF) and extended Kalman filter (EKF) . In case of non-linear systems, the unscented kalman filter (UKF) are used instead of the KFs.In cases where parameter and states are to be updated simultaneously a dual Kalman filter (DKF) is used. In this thesis use of Kalman filter and dual Kalman filter is made to predict the SOH of a battery in real time.

4.3.1. Kalman filters

In this section the general algorithm of a filtering process is discussed. The idea of a filter is to estimate the unmeasured state x_k of a corresponding physical system in real time in a dynamic environment, given knowledge of the system's measured input/output signals. In the context for this report, x_k can be any state like SOC of the cell or the SOH of a battery. The input u_k is the applied current. ω_{k-1} is the process noise, which can be considered as a noise in measurement of current .υ_k is output sensor noise or the noise in predicting the desired noise.

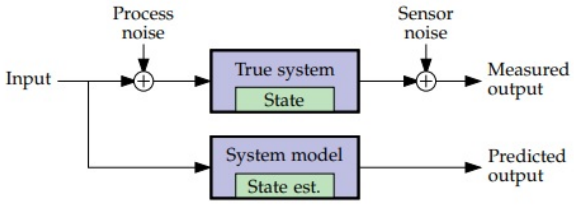

Figure 4.2: A physical system with noise [7]

As seen in figure 4.2 the system measured output can never match the predicted output as long as there is noise in system. The important thing of noise is that, all physical systems new or old have some level of noise in them. The noise level can change when the system gets older, and its the responsibly of the filter to update the assumed system model as a feedback to increase the accuracy of the predicted output.

Given below is the algorithm for a linear kalman filter.The discrete-time Kalman filter computes two different estimates of the state and covariance matrix for each sampling interval. The first estimate, $\tilde{x}_k^-$,is based on the prior state estimate as computed in the previous iteration, $\tilde{x}_{k-1}^+$, propagated forward in time one sample interval using a model of system dynamics. It is computed before any system measurements are made, and is denoted by superscript "**–**".

The Kalman filter is initialized with the best available information on the state and error covariance. This need not be accurate as the filter should be able to converge to real value in few iterations.

Algorithm 1 Summary of the Kalman filter estimator

Linear state-space Model
$x_{k+1} = A_k x_k + B_k u_k + w_k$
$y_k = C_k x_k + D_k u_k + v_k$

Initialization

For k = 0 set

$\hat{x}_0^+ = \mathbb{E}[x_0]$

$\Sigma_{\tilde{x},0}^+ = \mathbb{E}\left[(x_0 - \hat{x}_0^+)(x_0 - \hat{x}_0^+)^T\right]$

Computation

For k = 1,2,...compute

State estimate time update $\hat{x}_k^- = A_{k-1}\hat{x}_{k-1}^+ + B_{k-1}u_{k-1}$

Error covariance time update $\Sigma_{\tilde{x},k}^- = A_{k-1}\Sigma_{\tilde{x},k-1}^+ A_{k-1}^T + \Sigma_\omega$

Kalman gain matrix $L_k = \Sigma_{\tilde{x},k}^- C_k^T \left[C_k \Sigma_{\tilde{x},k}^- C_k^T + \Sigma_v\right]^{-1}$

State estimate measurement update: $\hat{x}_k^+ = \hat{x}_k^- + L_k\left[y_k - (C_k\hat{x}_k^- + D_k u_k)\right]$

Error covariance measurement update $\Sigma_{\tilde{x},k}^+ = (I - L_k C_k)\Sigma_{\tilde{x},k}^-$

The kalman filter algorithm is divided into two phases as seen in fig 4.3. The prediction phase is based on the initialization the system state and covariance is estimated based on the input u_k and the output is predicted . It is divide into 3 steps. 1a - is called the state estimate, where the estimate is done based on previous values. 1b- Updates the covariance or uncertainty based on previous iteration values. 1c- is where the output is predicted based on the estimated state.

In second phase which is know as innovation or correction phase. It is subdivide into 3 steps 2a updates the gain based on the predicted covariance, followed by a predicted state value based on the measured output in 2b. 2c -is where the covariance is updated based on the gain and previous step covariance. The kalman filter is an iterative process and the goal is to reduce the gain and converge the uncertainty or covariance to a stable value.

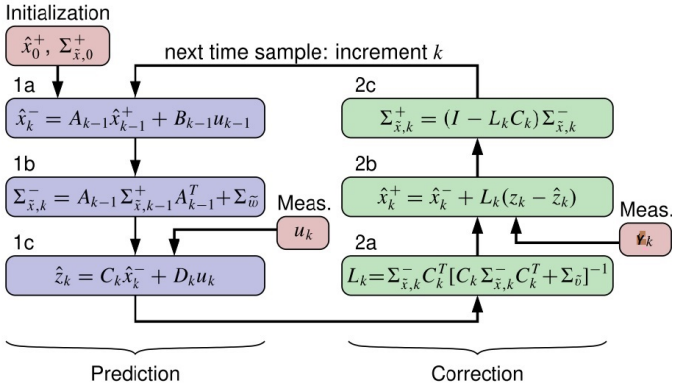

Figure 4.3: Single linear Kalman visualization [7]

To summarise,the Kalman filter provides a theoretically elegant and time-proven method to process measurements of system input and output to produce an intelligent real-time estimate of a dynamic system's state. The equations are easy to implement in a micro-controller setup in an actual BMS of a vehicle.

Till now we discussed only a linear kalman filter . But as we will see in section4.4 the SOC of the battery is used as an input to calculate the LAM aging, while the change in SEI layer causes the internal resistance of the cell to increase which results in a change in the cell voltage and power fade. So, there is a need to have a feedback loop with the performance model as well. This can be achieved via the use of a Dual kalman filter.

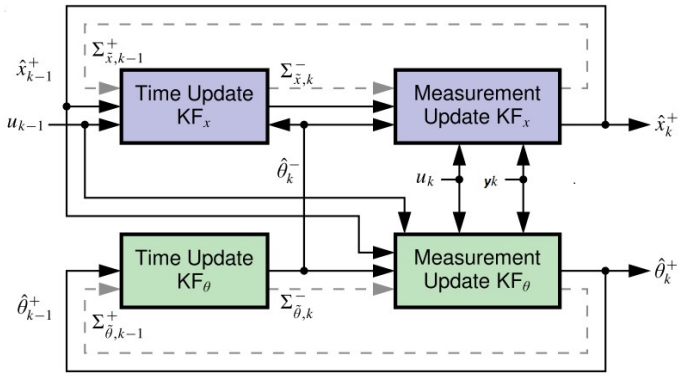

Figure 4.4: Dual Kalman visualization. Solid lines represent state and parameter vector signal flow and dashed grey lines represent error covariance matrix signal flow [7]

The process essentially comprises two Kalman filters running in parallel one adapting the state and one adapting parameters with some information exchange between the filters. In the model the SOC and Voltage are updated via the upper loop of KF_x and the Aging models are updated via the lower loop of KF_θ. The algorithm for a dual kalman filter is given below.

Algorithm 2 Summary of the dual Kalman filter estimator

For State Updates

$x_{k+1} = A_k x_k + B_k u_k + w_k$, where, $x_{k+1} = f(x_k, u_k|\theta_k)$

$y_k = C_k x_k + D_k u_k + v_k$, where, $y_k = g(x_k, u_k|\theta_k)$

For Parameter Updates

$\tilde{\theta}_{k+1} = A_\theta \theta_k + B_\theta u_k + r_k$, where the output $d_k = g(x_k, u_k|\theta_k) + e_k$

Initialization

For k = 0 set

$\hat{x}_0^+ = \mathbb{E}[x_0]$
$\Sigma_{\tilde{x},0}^+ = \mathbb{E}\left[(x_0 - \hat{x}_0^+)(x_0 - \hat{x}_0^+)^T\right]$

$\hat{\theta}_0^+ = \mathbb{E}[\theta_0]$
$\Sigma_{\tilde{\theta},0}^+ = \mathbb{E}\left[(\theta_0 - \hat{\theta}_0^+)(\theta_0 - \hat{\theta}_0^+)^T\right]$

Computation

For k = 1,2,...compute

Time Update for the weight filter
$\hat{\theta}_k^- = \hat{\theta}_{k-1}^-$

$\Sigma_{\tilde{\theta},k}^- = \Sigma_{\tilde{\theta},k-1}^+ + \Sigma r$

Time update for the state filter

$\hat{x}_k^- = A_{k-1}\hat{x}_{k-1}^+ + B_{k-1}u_{k-1}$

$\Sigma_{\tilde{x},k}^- = A_{k-1}\Sigma_{\tilde{x},k-1}^+ A_{k-1}^T + \Sigma_\omega$

Measurement update for the state filter

$\Sigma_{\tilde{x},k}^- C_k^T \left[C_k \Sigma_{\tilde{x},k}^- C_k^T + \Sigma_\upsilon\right]^{-1}$

$\hat{x}_k^+ = \hat{x}_k^- + L_k\left[y_k - C_k\hat{x}_k^- D_k u_k\right]$

$\Sigma_{\tilde{x},k}^+ = (I - L_k C_k)\Sigma_{\tilde{x},k}^-$

Measurement update for the weight filter

$L_k^\theta = \Sigma_{\tilde{\theta},k}^- C_k^{\theta^T}\left[C_k^\theta \Sigma_{\tilde{\theta},k}^- C_k^\theta + \Sigma_e\right]^{-1}$
$\hat{\theta}_k^+ = \hat{\theta}_k^- + L_k\left[y_k - C_k^\theta\hat{\theta}_k^- + D_k u_k\right]$
$\Sigma_{\tilde{\theta},k}^+ = (I - L_k^\theta C_k^\theta)\Sigma_{\tilde{\theta},k}^-$

Here, ω_k, υ_k, r_k and e_k are the noise in the system.

4.4. Estimators

Having introduced the general framework, the contribution of this thesis is to calculate various states of the battery system in real time. To achieve this, all the states should be brought into a generic form of State space equation for Kalman filter to be applied. This is true for a linear kalman filter as the equations of the aging models have linear relationship.

4.4.1. SOH estimator

The aim of this thesis is to estimate the SOH of a battery in real-time. In order to so, we need to estimate the aging in the battery in real-time. As discussed in earlier sections the major degradation mechanisms considered in the reduced order model are 1. SEI degradation 2. Loss of active material 3.Lithium plating.
We need to get the equations discussed in 3.4 in state space form. The dynamics to get the aging models in state space form is discussed below.

SEI aging estimator

SEI layer formation is related to the side reaction current density, i_s via the equation .

$$Q_{\text{SEI}} = \int i_{st} A_{cell} dt$$

$i_s t$ calculation is discussed in section 3.4.1. It is evident that the calculation of i_{st} side current is a function of the applied current I_{app} seen in e.q 3.6 and e.q 3.7. Thus the whole SEI aging is a function of I_{app}. In state space form,

$$Q_{\text{SEI}_{k+1}} = Q_{\text{SEI}_k} + i_{st} A_{cell} \delta t$$

and growth of SEI layer is given by,

$$\frac{d\text{SEI}}{dt} = \frac{i_{st} M_{\text{SEI}}}{2F\rho_{\text{SEI}}}$$

can be written as

$$dsei_{k+1} = dsei_k + \frac{i_{st} M_{\text{SEI}}}{2F\rho_{\text{SEI}}} dt$$

As, we are only calculating a single state x_k and y_k will be the same. So we have multi output single input filter, where,

$$\tilde{A} = \begin{vmatrix} 1 & 0 \\ 0 & 1 \end{vmatrix}, \tilde{B} = \begin{vmatrix} dt \\ \frac{M_{\text{SEI}}}{2F\rho_{\text{SEI}}} \end{vmatrix}, \tilde{C} = 1, \tilde{D} = 0 \tag{4.2}$$

The final state space model for SEI degradation is then,

$$\begin{vmatrix} Q_{\text{SEI}_{k+1}} \\ dsei_{k+1} \end{vmatrix} = \begin{vmatrix} 1 & 0 \\ 0 & 1 \end{vmatrix} \begin{vmatrix} Q_{\text{SEI}_k} \\ d\text{SEI}_k \end{vmatrix} + \begin{vmatrix} dt \\ \frac{M_{\text{SEI}}}{2F\rho_{\text{SEI}}} \end{vmatrix} i_{st} \tag{4.3}$$

As the estimators are model based, measurement error was introduced in the ROM SEI aging model to replicate real measurement cases, where there is always some noise in the experimental setup in the form of process noise and measurement noise (sensor noise). As applied current is only variable input for the model, a 2% process noise is introduced to input Current I_{app}. This causes noise propagation throughout the system. Table shows the propagation of noise in the system.

Table 4.1: Noise propagation in SEI sub model

	Noise	**Units**
Input Current	2%	unitless
Maximum Noise in Current (absolute)	4.2	[A]
Maximum noise in θ_{sei}	1.53*e-05	unitless
Maximum Noise in overpotential	0.27	[V]
Maximum Noise in side current (i_{st})	1.1965*e-05	[A]
Maximum Noise in Qsei	5%	[A.h]
Maximum Noise in Qsei (absolute)	1.28*e-06	[A.h]
Maximum Noise in d_{sei}	5%	unitless
Maximum Noise in dsei (absolute)	1.2*e-12	[m]

Algorithm 3 Initialization of SEI estimator

Linear state-space Model
$x_{k+1} = \tilde{A}_k x_k + \tilde{B}_k u_k + w_k$
$y_k = \tilde{C}_k x_k + \tilde{D}_k u_k + v_k$

Here,
The sate equation matrix $\tilde{A}, \tilde{B}, \tilde{C}, \tilde{D}$ take the value as given in e.q 4.2.

$u_k = i_{st}$ (Noisy side current as input)

Initialization

For k = 0 set

Set Σ_ω = 1e-05 (The process noise covariance should be close in magnitude as the maximum noise in input u_k for the noise to remain within uncertainty bounds)

Similarly, Set Σ_υ = 1e-06 (The sensor noise covariance should be close in magnitude as the maximum noise in estimation of Output Q_{sei} for the noise to remain within the uncertainty bounds). For dsei,Σ_υ is initialized to a value of 1e-12.

$\hat{x}_0^+ = Q_{sei_0}$ (The initial value of SEI loss, for a new battery it is set to 0)

$\Sigma_{\tilde{x},0}^+ = 1e-6$ (Initial uncertainty determines how fast the filter can converge to a stable value. For tuning this value, different high and low values uncertainties were tested. The filter converged faster when the uncertainty was in same magnitude as the output State Q_{sei}. For dsei $\Sigma_{\tilde{x},0}^+ = 1e-12$

Computation (Same process as discussed in Algorithm 1)

For k = 1,2,...compute

State estimate time update $\hat{x}_k^- = A_{k-1}\hat{x}_{k-1}^+ + B_{k-1}u_{k-1}$

Error covariance time update $\Sigma_{\tilde{x},k}^- = A_{k-1}\Sigma_{\tilde{x},k-1}^+ A_{k-1}^T + \Sigma_\omega$

Kalman gain matrix $L_k = \Sigma_{\tilde{x},k}^- C_k^T \left[C_k \Sigma_{\tilde{x},k}^- C_k^T + \Sigma_\upsilon\right]^{-1}$

State estimate measurement update: $\hat{x}_k^+ = \hat{x}_k^- + L_k \left[y_k - C_k \hat{x}_k^- D_k u_k\right]$

Error covariance measurement update $\Sigma_{\tilde{x},k}^- = (I - L_k C_k)\Sigma_{\tilde{x},k}^-$

Results

The results of the Qsei estimator for 1 charge balanced UDDs cycle is discussed. The charged balanced UDDS cycle is a special case of drive cycle, where the starting SOC and the end SOC is kept constant. This is achieved via large amount of regenerative braking. This special drive cycle is used as it covers discharge during acceleration and charging during braking. So aging behaviour for both charging and discharging can be analysed in one cycle. Figure 4.5 shows the estimation Q_{sei} loss with zoomed in image of the estimator. The red line depicts the noisy output of the ROM SEI Model and the blue line is the estimator predicted output. The dotted lines are the confidence bounds of the estimator. They tell us we have high confidence that the true value lies between $\hat{x}_k^+ \pm 3\sqrt{\Sigma_{\tilde{x},k}^+}$ or 3σ bounds.

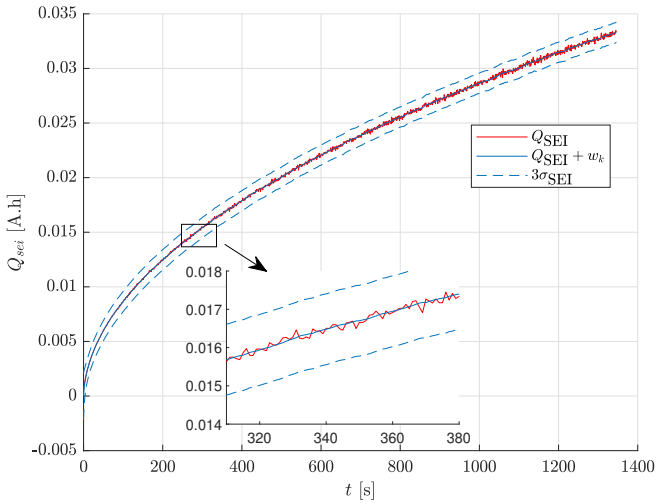

Figure 4.5: Estimation of SEI degradation for a fresh cell with noisy inputs and confidence bounds

Figure 4.6 (a) shows the error between the noisy output from the ROM Model and the estimated output by the estimator. The error start from zero as the estimator was correctly initialized and the absolute value error increases as the noise in the system accumulated during the cycle.Figure 4.6 (b) shows the percentage error for the estimator. The estimator is finely tuned and the percentage error between the estimated value and the model output lies with a maximum of 1.49 % and a minimum of -1.87 % . The uncertainty of the estimator takes 7 secs to converge to a stable value.

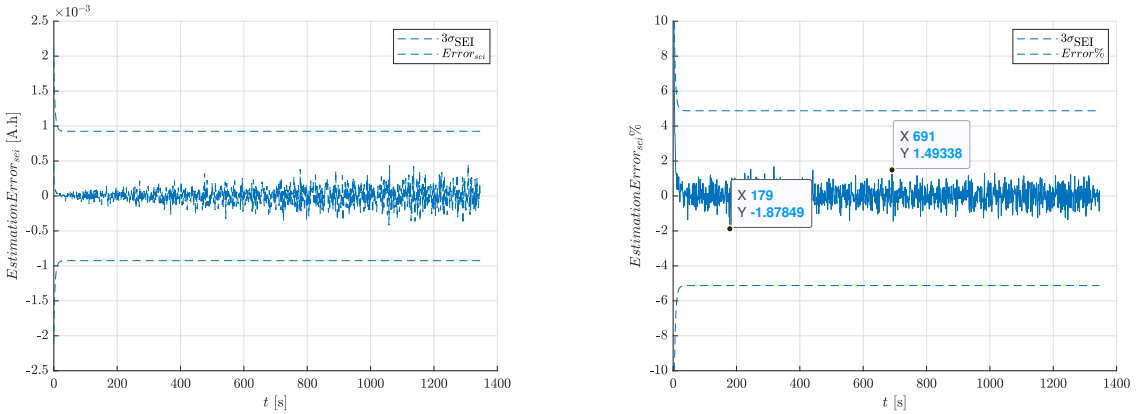

(a) Estimation of SEI error (absolute)

(b) Estimation of SEI error in percentage

Figure 4.6: Estimation OF SEI error

Figure 4.7 shows the dsei estimator result with a zoomed in view. The red line represents the noisy ROM model output and the blue line depicts the estimator output. Dotted lines represent the confidence

bounds of the estimator. The estimator output underestimates the SEI thickness at start and can be seen Figure 4.8 (a) and (b). This is due to fact that, even in a fresh battery there is still a small initial layer of thickness, which causes the initial internal resistance. The initial guess to the estimator is taken as zero. So, the estimator tries to correct the difference in initial few seconds. It takes 27 seconds for the uncertainty to converge to a stable value. The maximum error in the stable phase is 1.5% and a minimum of -1.6% for the entire cycle.

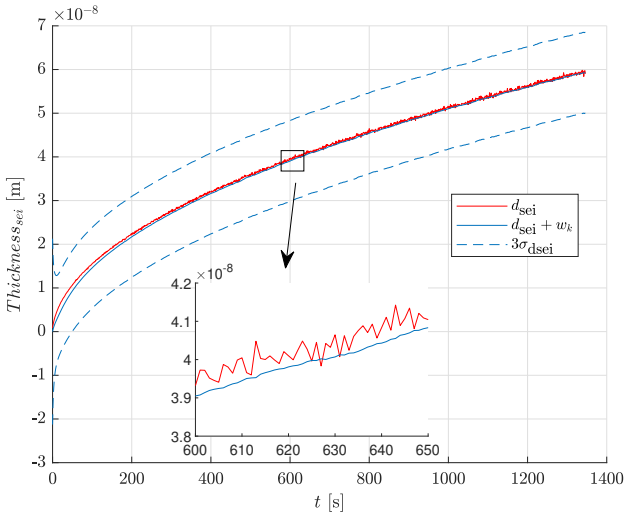

Figure 4.7: Estimation of SEI layer thickness for a fresh cell with noisy inputs and confidence bounds

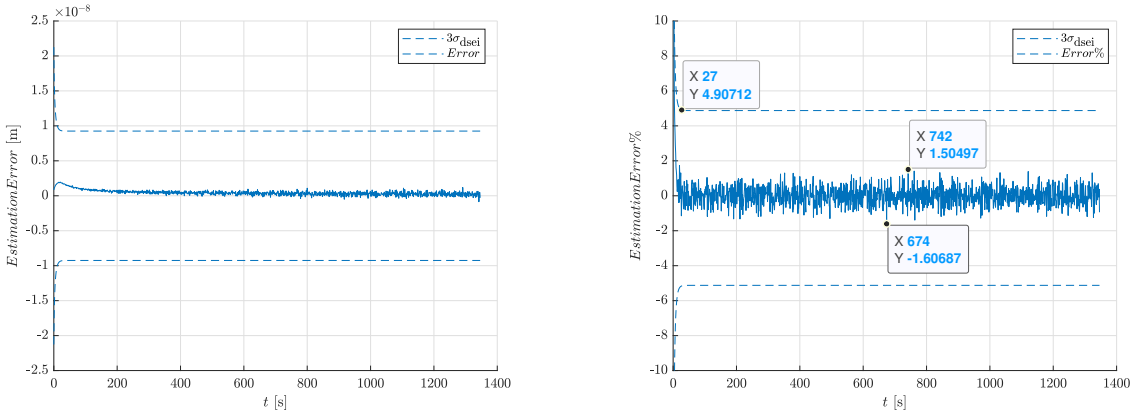

(a) Estimation of dsei error (absolute)

(b) Estimation of dsei error in percentage

Figure 4.8: Estimation OF dsei error

Loss of active material estimator

Similar to the SEI estimator, the LAM estimator has only one output state so, the, state space equation is given as,

$$Q_{am_{k+1}} = Q_{am_k} + k_{am} exp(\frac{-E_{am}}{RT}).SOC.|I_{app}|\Delta t \tag{4.4}$$

where,

$$\tilde{A} = 1, \tilde{B} = \frac{-E_{am}}{RT}.SOC.dt, \tilde{C} = 1, \tilde{D} = 0$$

SOC is taken as an input from performance model. this makes the system into a dual kalman filter which will be discussed in sections below.

Similar to the Qsei estimator discussed above, the applied current is introduced with a process noise of 2%. This causes noise propagation in the sub model.

Table 4.2: Noise propagation in LAM sub model

	Noise	**Units**
Input Current	2%	unitless
Maximum Noise in Current (absolute)	4.2	[A]
Maximum noise Qam (absolute)	4.74*e-6	[A.h]
Maximum Noise in Qam	2%	unitless

In case of LAM estimator, the estimator is more sensitive and takes more time to converge as it has an feedback loop with SOC estimator and the error in SOC affects the LAM estimator. Similar to SEI estimator, the initialization of LAM estimator is done by setting $u_k = I_{app}$ (Noisy input current). Σ_ω = 1e-12 (This is kept so low to reduce the error in system as the error multiplies due to feedback loop with SOC estimator). Σ_v = 1e-6.$\hat{x}_0^+ = Q_{Lam_0}$ (The initial value of LAM loss, for a new battery it is set to 0).

Results

Figure 4.9 shows the LAM estimator with zoomed view. The red line shows the Noisy ROM model output, while the blue line represents the estimated Qam. The output of the ROM LAM sub model is extra noisy due to two changing inputs of I_{app} and SOC amplifying the noise in the model. Figure 5.2a (a) shows the absolute error in the system and Figure 5.2a (b) represents the percentage error with a maximum of 0.3% and min of -0.3%. The LAM estimator is slow to converge, but is more accurate than all other estimators.

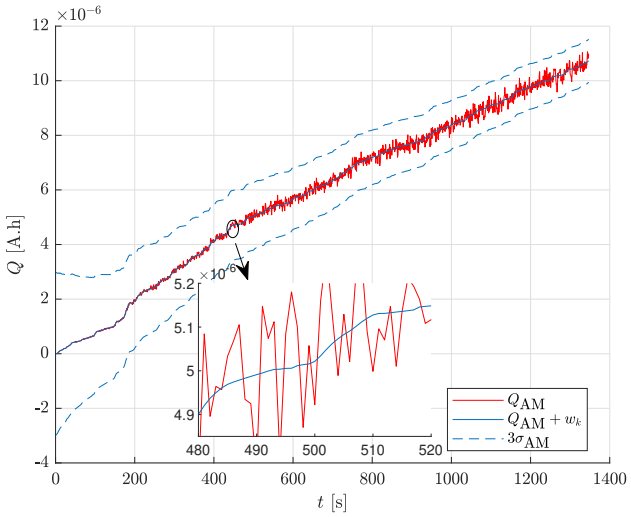

Figure 4.9: Estimation of LAM degradation for a fresh cell with noisy inputs and confidence bounds

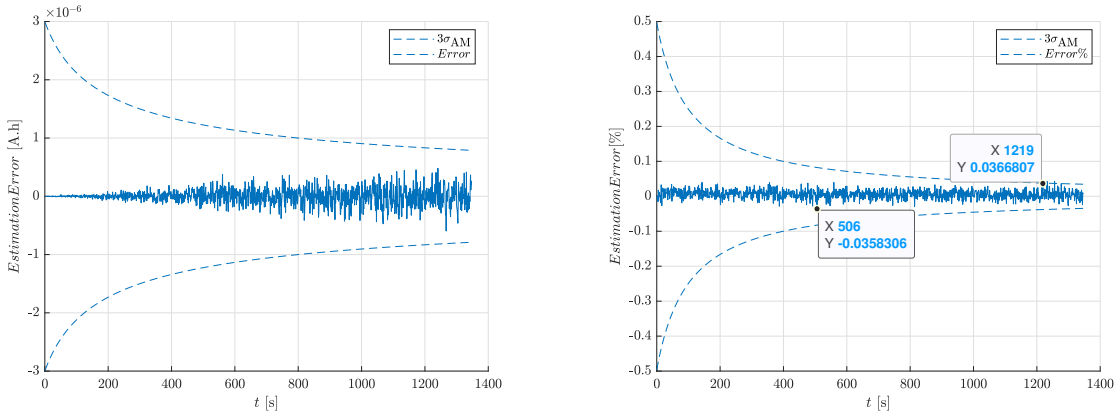

(a) Estimation of LAM error

(b) Estimation of LAM error in percentage

Figure 4.10: Estimation of LAM error

Li-plating estimator

Li-plating sub model estimator is calculated in the same way as done for the above cases,

$$Q_{Li,k+1} = Q_{Li,k} + J_{li} A_{cell} dt$$

, where,

$$\tilde{A} = 1, \tilde{B} = A_{cell} dt, \tilde{C} = 1, \tilde{D} = 0$$

where $J_l i$ is the lithium plating side current which is dependent on the applied current I_{app} discussed in e.q 4.24, e.q 4.25 and e.q 4.26.

The SEI growth sub model and the Li-plating model are related to each other by the Eq. 4.27. So the dsei calculated in 'k' iteration is used as an input to estimate Li-plating for 'k+1' iteration.
Similar to estimators discussed above, the applied current is introduced with a process noise of 2%. This causes noise propagation in the sub model. Table 4.3 describes the error propagation in LIP sub model.

Table 4.3: Noise propagation in LIP sub model

Variables	Noise	Units
Input Current	2%	unitless
Maximum Noise in Current (absolute)	4.2	[A]
Maximum Noise in overpotential	-0.0542	[V]
Maximum Noise in side current (j_{li})	1.20*e-05	[A]
Maximum Noise in Qli	5%	unitless
Maximum Noise in Qli (absolute)	6.94*e-4	[A.h]

The LIP estimator is initialized with $u_k = j_{st}$ (Noisy side current density as input).Σ_ω = 1e-07.Σ_v = 1e-08.$\hat{x}_0^+ = Q_{lip_0}$ (The initial value of LIP loss, for a new battery it is set to 0). The initialization of LIP estimator required smaller magnitude of process and sensor noise as the noise from the SEI estimator due to growth of SEI layer being linked to change in Volume fraction for the lithium plating estimator, generates additional noise.

Results of LIP Estimator

Figure 4.11 shows the results of LIP estimator, with red lines showing the noisy output of the ROM LIP sub model. The estimator predicts the aging properly and the error seen in Figure 4.12 (a) and (b) are within the uncertainty bounds. The absolute error increases more towards the end as the balanced UDDS cycle as high regenerative braking at the end to recover the lost SOC, thus higher charging current is applied which increases the rate of Lithium plating in the model and thus more error.

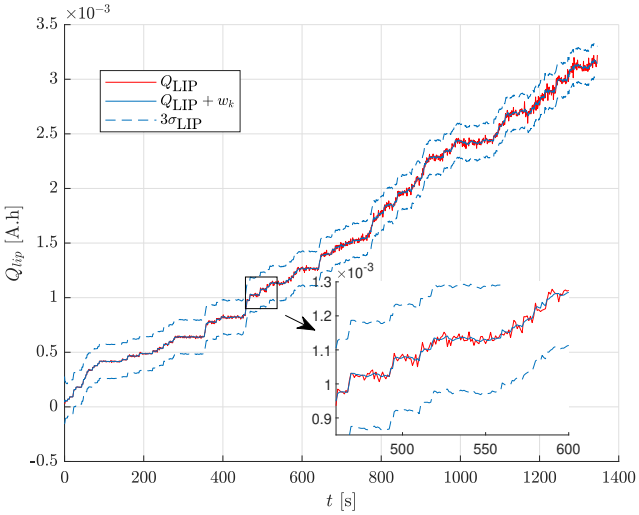

Figure 4.11: Estimation of Li-Plating degradation for a fresh cell with noisy inputs and confidence bounds

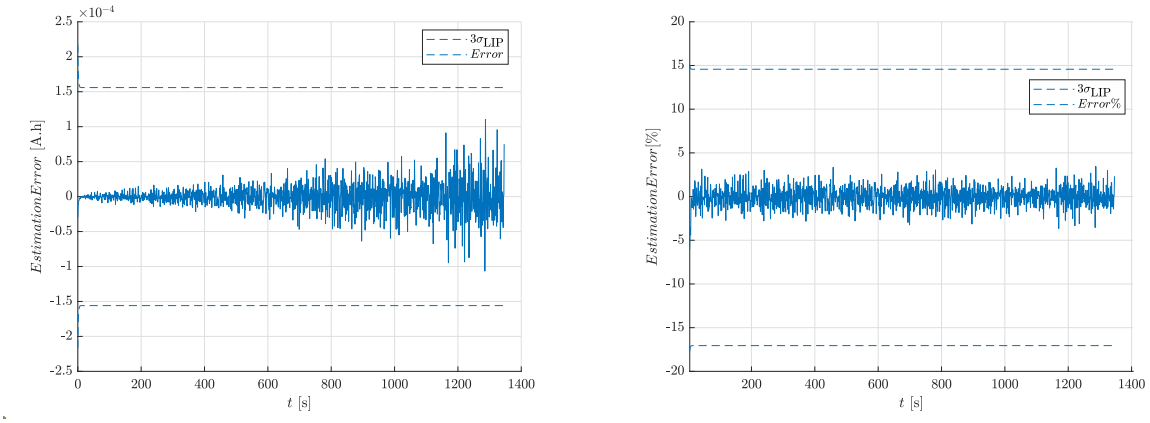

(a) Estimation of Li-Plating error

(b) Estimation of Li-Plating error in percentage

Figure 4.12: Estimation of Li-Plating error

SOH estimator

The final goal of this thesis was to build a SOH estimator. The SOH estimator answer the first research sub question of 'How to estimate the SOH of a cell in real-time using adaptive control techniques? Summing up all the predicted value of the aging estimator, we get capacity loss for a cell. Figure 4.13 (a) shows the capacity loss for a single UDDS drive cycle in absolute terms, while Figure 4.13 (b) shows the estimation of Capacity loss in percentage for a fresh cell in 1 UDDs drive cycle. The total loss in Capacity in a single cycle is 0.045% or 3.2*10-4 A.h.

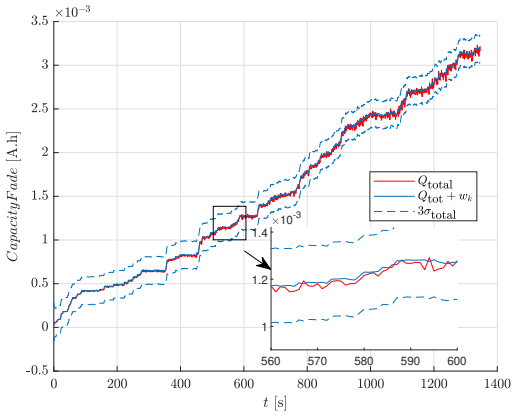

(a) Estimation of Capacity loss for a fresh cell with noisy inputs and confidence bounds

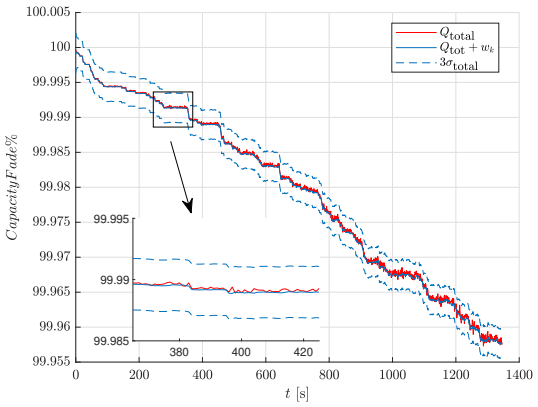

(b) Estimation of Capacity loss in relation to a fresh cell with no degradation capacity

Figure 4.13: Estimation of Capacity loss (SOH estimator)

State of Power (SOP)

SOP is the available power to be charged or discharged from the battery. Instantaneous power delivered by a cell is given by $P = V * I$. As we have introduced 2% noise in measuring the current. The Voltage also deviates as the resistance of the cell changes due to change in thickness of SEI layer, which is predicted by the Voltage estimator. Thus the power delivered by the cell will vary from an ideal cell. Figure 4.14 (a) shows the estimated Power by the estimators with noisy inputs vs Actual Power from ROM model. Figure 4.14(b) shows the estimated Power delivered relative to an ideal cell. The maximum power delivered is 103% and minimum is 95.3% relative to an ideal cell.

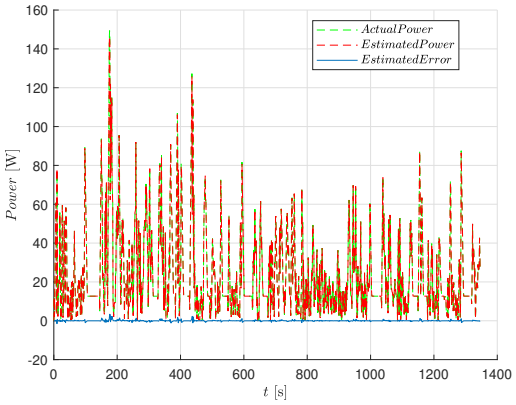

(a) Estimated Power delivered by a fresh cell

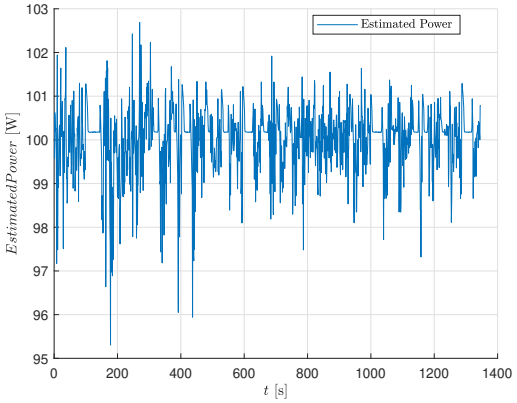

(b) Estimated Power delivered by a fresh cell with noisy inputs relative to an ideal cell

Figure 4.14: Estimated Power delivered by a fresh cell with noisy inputs

4.4.2. SOC estimator

As discussed in chapter 3,Cell state of charge can be related either to the total amount of lithium in the negative electrode or to the total amount in the positive electrode.

The cell SOC can be calculated as

$$SOC = \frac{\theta_{avg} - \theta_0}{\theta_{100} - \theta_0} \tag{4.5}$$

where, $\theta_{avg} = \frac{c^{neg}_{s,avg}}{c^{neg}_{smax}}$. State of charge varies linearly as the stoichiometry of the negative electrode varies between x0% and x100% (or, equivalently, as the stoichiometry of the positive electrode varies

between y0% and y100%).
In this Case, as the state and output is same so x_k and y_k is the same. A filter is now, reduced to

$$y_k = C_k x_k + z_0$$

where,

$$\tilde{A} = 0, \tilde{B} = 0, \tilde{C} = \frac{C_{s,k}}{C_s^{max}(\theta_{100}^{neg} - \theta_0^{neg})}, \tilde{D} = z_0$$

and, z_0 is the initial condition of SOC, generally given as an input. For the estimation of SOC, we will require concentrations of the electrodes online. The measurements available from a cell in real-time are current (I_{app} and Voltage (V). So using only current and Voltage we should be able to estimate concentrations. This is achieved by two methods:

Current as input
In this method, using the transfer function given in equation A.4, the ROM can provide the required concentrations $c_{s,avg}$ as a output, which can be used by the estimator to calculate SOC.

Current and voltage as input In this method, $c_{s,avg}$ is calculated by using the Voltage and Current as input. The Voltage is given by the relationship,

$$\begin{aligned}\text{Voltage} = \text{Difference in Over Potential of electrodes} + \text{Difference in Open circuit Potential} \\ + \text{Electrolyte Potential} + \text{Film Resistance}\end{aligned}$$

Here,voltage is the measured value . The difference in electrolyte potential is very small (in the order of $10^(-2)$) and can be neglected. The Over Potential can be calculated by the transfer function A.6, which is a function of input current (I_{app}. The remaining variable is the difference in open circuit variables which are a function of θ_{avg} as given in equation and . Thus θ_{avg} can be calculated by this way, to then estimate SOC.

Figure 4.14, shows the SOC estimation for a fresh battery with noisy inputs and confidence bounds. The red line is the noisy SOC output and $Qsoc + wk$ is the predicted value by the estimator. The confidence bounds provide a limit to the accuracy of the estimator. Figure 4.15(a) shows the error in the system and 4.15(b) depicts the percentage error for the estimator. It is to be noted that the estimator performs well within the error bounds with an maximum error of 1.8%. The confidence interval converge to a stable value within first few cycles.

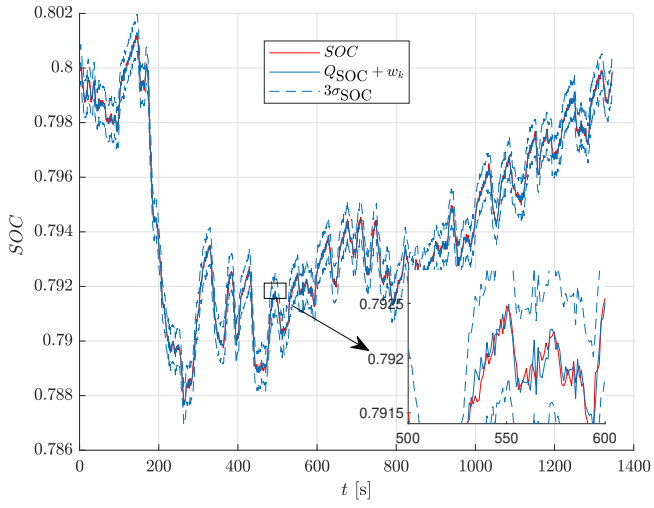

Figure 4.15: Estimation of SOC for a fresh cell with noisy inputs and confidence bounds

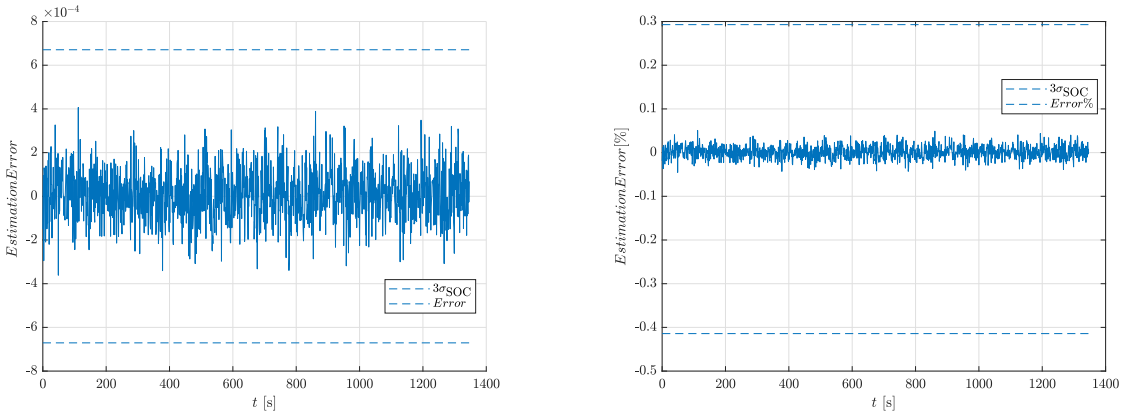

(a) Estimation of SOC error(absolute)

(b) Estimation of SOC error in percentage

Figure 4.16: Estimation of SOC error

4.4.3. Voltage estimator

The voltage of a cell is calculated as

$$V_{cell} = \eta^{pos} - \eta^{neg} + \phi_e^{pos} - \phi_e^{neg} + U_{ocp}^{pos} - U_{ocp}^{neg} - FR_{film}I_{app} \tag{4.6}$$

as per e.q 4.16 the resistance of the cell is update every iteration as the thickness of the SEI layer increases. So a feedback of SEI layer is provided that updates the R_{film} every iteration.
Figure 4.17 shows the estimation of Voltage with zoomed in view. The red line shows the noisy output of the ROM model and blue line is the predicted estimator output. As seen in figure 4.18 (a) and (b) there is extra noise in the system and the error goes beyond the the uncertainty bounds at some instances. The voltage estimator is thus 93% accurate within the 3σ bounds. The maximum estimation error is 4.8% and the minimum error is -2.6%.

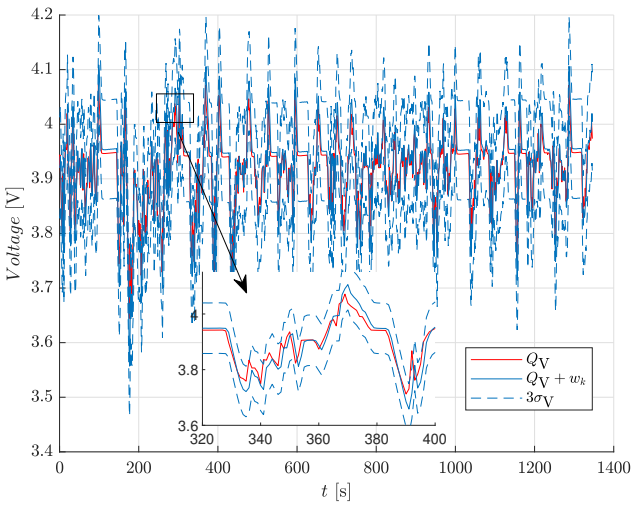

Figure 4.17: Estimation of Voltage for a fresh cell with noisy inputs and confidence bounds

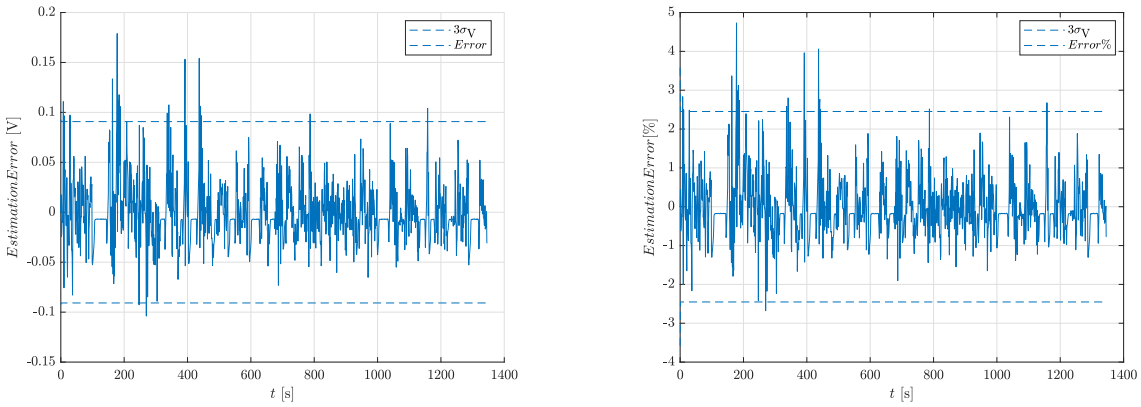

(a) Estimation of Voltage error

(b) Estimation of Voltage error in percentage

Figure 4.18: Estimation of Voltage error

4.5. Summary

In this chapter, the algorithms to estimate the aging of a cell in real time using Kalman filtering methods is discuused. To estimate the states like SOC and Voltage and aging parameters simultaneously a dual Kalman filter algorithm is implemented. All the estimators predict the states and the outputs accurately, with maximum percentage error < 5%. The total capacity loss in one UDDS drive cycle was estimated to be 0.045%.

5

Adaptability of the estimators

In Chapter 4, the algorithm to estimate the states of the battery in real time was discuused. In this chapter the ability of the estimators to adapt to various changing conditions is explored.

5.1. Changing Initial Conditions

In this section the answer to the second research sub-question 'How fast can the estimator react to changing initial states of the cell?'is answered. Till now the all the results were validated for a new cell. In real life scenarios the cell may age and the initial conditions for the estimators may not be the same. Thus the estimator accuracy and speed needs to be validated for various cases, with a fresh and old cell.

Case1 :Fresh Cell

In this case as seen in fig. 5.1, the estimator is run for 5-UDDS charge depleting drive cycles. The initial estimate for the estimators are the same as for the ROM aging models.The convergence times for the various estimators are shown in Figure 4.19. The major takeaway from this case is that the estimators takes 6 seconds to come to estimate the true SOH for a fresh cell. Also, running for a longer cycles, the loss due to Li-plating which is the major contributor to the overall aging of the cell, plateaus, as the formation of additional SEI thickness layer, prevents extra plating to occur.

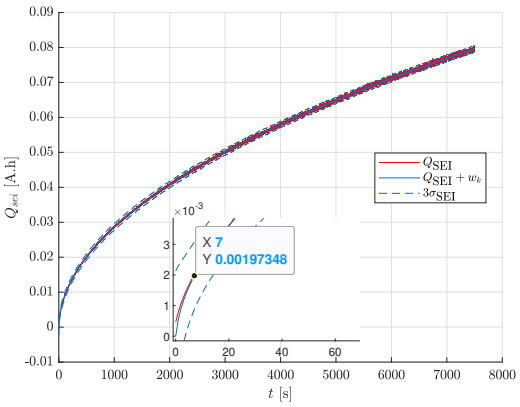

(a) Convergence time of SEI estimator for a fresh cell

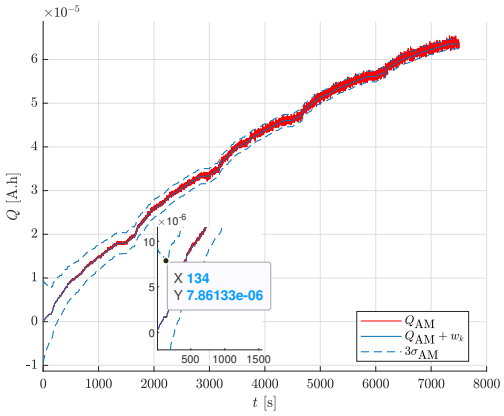

(b) Convergence time of LAM estimator for a fresh cell

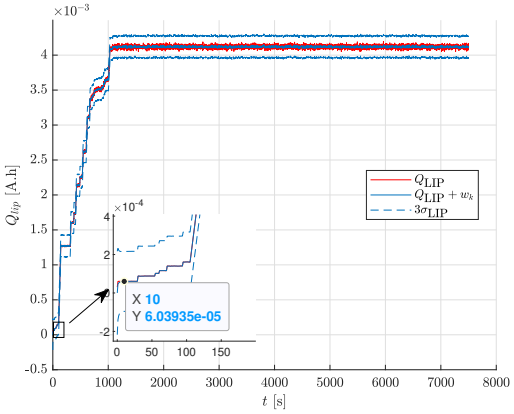

(c) Convergence time of LIP estimator for a fresh cell

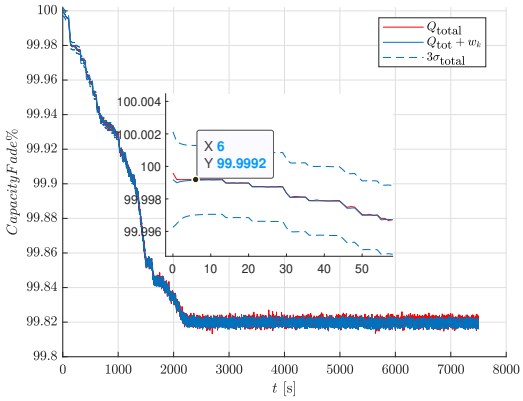

(d) Convergence time of SOH estimator for a fresh cell

Figure 5.1: Convergence time of estimators for a fresh cell

5.1.1. Initial guess of a 5-UDDS cycle old cell to a fresh cell

In this case an cell is run for 5-UUDS cycles at 1C , but the estimators are initialized with the conditions of a new cell. This is done to check how long the estimator takes to recognise and adapt to the changing conditions. Figure 4.20 shows the various estimators convergence times. Figure 4.20 (d) shows the SOH estimator takes 21 secs to adapt to the different initial conditions. This is fast enough to be used in real-time scenarios.

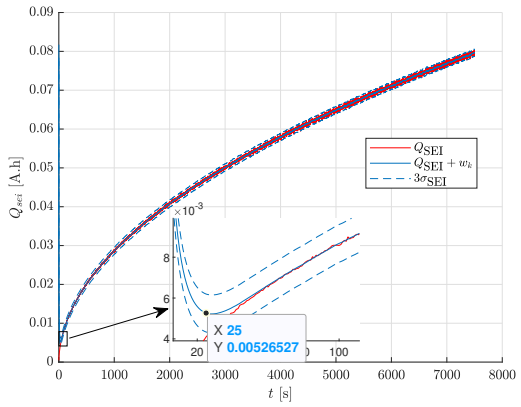

(a) Convergence of SEI estimator time of a fresh cell with an initial guess of a used battery for 5-UUDS cycle

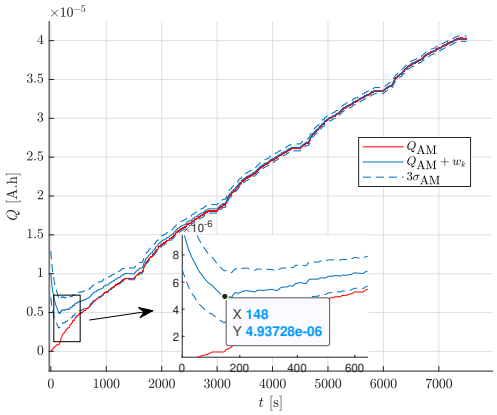

(b) Convergence of LAM estimator time of a fresh cell with an initial guess of a used battery for 5-UUDS cycle

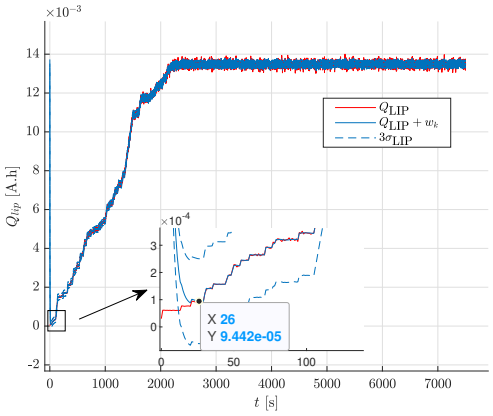

(c) Convergence of LIP estimator time of a fresh cell with an initial guess of a used battery for 5-UUDS cycle

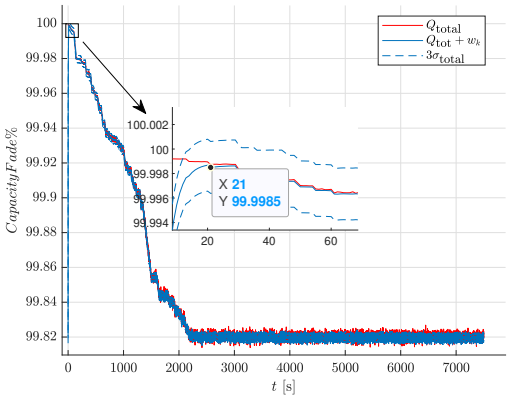

(d) Convergence of SOH estimator time of a fresh cell with an initial guess of a used battery for 5-UUDS cycle

Figure 5.2: Convergence of estimator times of a fresh cell with an initial guess of a used battery for 5-UUDS cycle

Table 5.1 shows the estimators times with different initial conditions of a fresh and old cells. The highest time taken is by the LAM estimator. This is due to the fact that LAM estimator has 2 noisy inputs (SOC and Current), thus the noise in the system is high and the estimator takes more time to converge. Even with a old cell that has undergone aging for few UDDS cycles, the estimator is able to adapt to the changing conditions in 15-20 secs. This proves the robustness of the estimators in real-time applications.

Table 5.1: Convergence of estimators for various cases.

		Fresh Cell	**Old Battery(5-UUDS)**
	Time	(sec)	(sec)
Fresh Cell	SOH	6	21
	SEI	7	45
	dsei	6	40
	LAM	134	181
	LIP	10	21
5-UDDS at 1C	SOH	16	3
	SEI	21	2
	dsei	26	2
	LAM	120	29
	LIP	26	3
5-UDDS at 2C	SOH	21	15
	SEI	27	18
	dsei	27	11
	LAM	126	164
	LIP	27	18
10- UDDS	SOH	29	18
	SEI	32	18
	dsei	29	19
	LAM	149	144
	LIP	28	17

5.1.2. Parameter estimation

In this section, the final research sub question : 'Can the estimators be adapted to concurrently estimate both the states and the time varying cell parameters in case of an old cell? How fast can this be achieved in context of real-time estimations?' is answered.

The research contribution provided in this thesis report will act as a stepping stone to achieving a digital twin of a Li-ion cell as a part of future projects. In the case of a digital twin, all states and parameters should adapt to different initial conditions. The idea is to update the initial parameters as per different initial conditions. This is possible by using the dual Kalman filter to estimate the parameters and states in parallel for a degradation model.

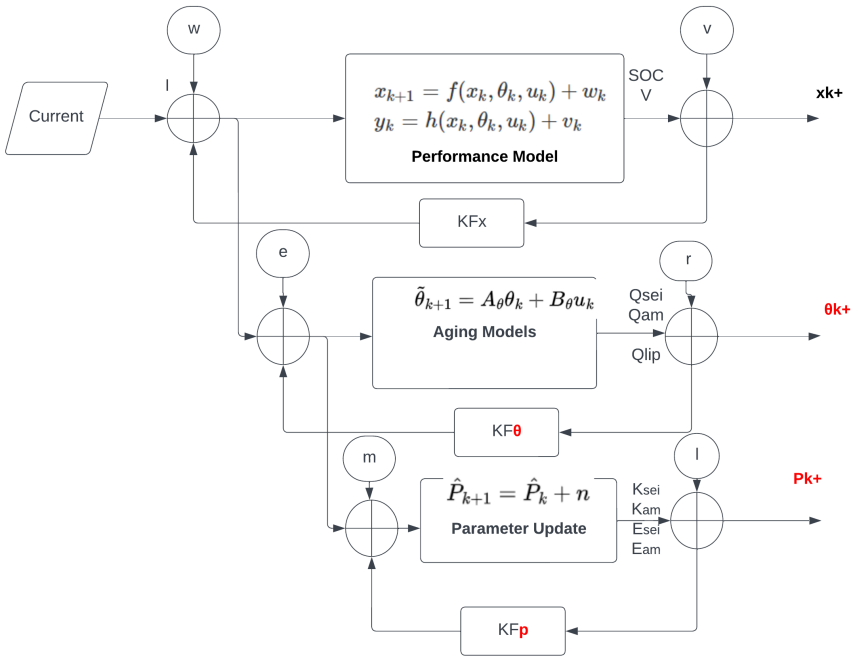

Figure 5.3: State space visualisation of the complete estimation process

Figure 5.3, shows the state space visualisation of the complete process used in parameter estimation. Here The first loop is the state space representation of the performance model where, the States and the outputs are a function of θ and the input k .The aging model is represented as a function of θ. the changes in the aging model are send an feedback to the performance model to update the states. The final loop is the parameter update where the input parameters used to calculate the aging models are updated. Real systems have noise in them and are processed in the system itself to give noisy output. w, e, m are the process noise in the system and v, r, l are the sensor noise for each of the models. The process comprises of three Kalman filters running in parallel. The first filter KF_x estimating and updates SOC and Voltage. The second filter KF_θ estimates and updates the aging states and the final Kalman filter KF_p estimates and updates the parameters.

5.1.3. SEI aging Model parameter update

The total loss SEI aging is as discussed in section 3.4.1 is given as.

$$Q_{sei,k+1} = Q_{sei_k} + \frac{K_{sei} * e^{\frac{-E_{sei}}{RT}}}{2(1 + \lambda\theta_{sei})\sqrt{t}_k} \tag{5.1}$$

Here, K_{sei}, E_{sei}, λ are all initial parameters, which were taken to be constants, to calculate the SEI aging. With time, these parameters tend to change slowly, as the cell ages. Also, these parameters are calculated in literature via various tests performed for a fresh cell under specific control environment. These parameters may not hold true for a aged cell. Here we have to use a dual extended Kalman filter, as the relationship between the parameters and aging models is non-linear.

Algorithm 4 Process to update parameters

For state-space aging models.
$\theta_{k+1} = f(\theta_k, u_k|P_k) + e_k,$

where P_k are the parameters to be updated.

In case of SEI Model, the relationship is as shown in equation 5.1,

For Parameter Updates, we need to find a relationship between aging model and the parameters, given by the C_k^P

where, $C_k^P = \frac{\partial f(\theta_k, u_k|P_k)}{\partial P}|_{P=\hat{P_k^-}}$

The partial differentiation for all the 3 parameters gives,
$C_k^{Ksei} = \frac{e^{\frac{-E_{sei}}{RT}}}{2(1+\lambda\theta_{sei})\sqrt{t}}$

$C_k^{Esei} = \frac{e^{\frac{-E_{sei}}{RT}}}{2(1+\lambda\theta_{sei})\sqrt{t}} * \frac{-K_{sei}}{RT}$

$C_k^{\lambda_{sei}} = \frac{-K_{sei} * e^{\frac{-E_{sei}}{RT}} * \theta_{sei}}{2\sqrt{t}(1+\lambda\theta_{sei})^2}$

Initialization (same as the initialisation done for SEI estimator in Algorithm 3)

Computation

For k = 1,2,...compute

Time Update for the parameter filter

$\hat{P}_k^- = \hat{P}_{k-1}^-$

$\Sigma_{\tilde{P},k}^- = \Sigma_{\tilde{P},k-1}^+ + \Sigma m$

Time update for the state aging filter

$\hat{\theta}_k^- = A_{k-1}\hat{\theta}_{k-1}^+ + B_{k-1}u_{k-1}$

$\Sigma_{\tilde{\theta},k}^- = A_{k-1}\Sigma_{\tilde{\theta},k-1}^+ A_{k-1}^T + \Sigma_e$

Measurement update for the state filter

$L_k^\theta = \Sigma_{\tilde{\theta},k}^- C_k^T \left[C_k \Sigma_{\tilde{\theta},k}^- C_k^T + \Sigma_r\right]^{-1}$

$\hat{\theta}_k^+ = \hat{\theta}_k^- + L_k \left[y_k - C_k \hat{x}_k^- D_k u_k\right]$

$\Sigma_{\tilde{\theta},k}^+ = (I - L_k C_k)\Sigma_{\tilde{\theta},k}^-$

Measurement update for the Parameter filter

$L_k^P = \Sigma_{\tilde{P},k}^- C_k^{P^T} \left[C_k^P \Sigma_{\tilde{P},k}^- C_k^P + \Sigma_l\right]^{-1}$

$\hat{P}_k^+ = \hat{P}_k^- + L_k \left[y_k - C_k \hat{x}_k^- D_k u_k\right]$

$\Sigma_{\tilde{P},k}^+ = (I - L_k^P C_k^P)\Sigma_{\tilde{P},k}^-$

5.1.4. LAM aging Model parameter update

For the LAM aging model, as discussed, there are 2 parameters that needs to be updated, K_{am} and E_{am}.
As discussed in section 3.4.2, the total LAM loss is given by,

$$Q_{am,k+1} = Q_{am,k} + k_{am} exp(\frac{-E_{am}}{RT}).SOC_k.|I_{app}|dt \tag{5.2}$$

Similar to the process followed for SEI aging parameter update, the partial differentiation for all the 2 parameters gives,

$$C_k^{K_{am}} = exp(\frac{-E_{am}}{RT}).SOC_k.|I_{app}|dt$$

$$C_k^{E_{am}} = \frac{-K_{am}}{RT} * exp(\frac{-E_{am}}{RT}).SOC_k.|I_{app}|dt$$

5.1.5. Results

SEI parameters

Figure 5.4 shows the change in the value of K_{sei}, a constant parameter assumed for modelling SEI aging. Different initial conditions are provided to the estimator with a 5, 10,50 UDDS drive cycle old aged cell outputs as the input to the estimator. The estimator converges to a new constant value after a few iteration. Table 5.2 describes the time taken by the estimator and the new updated parameter value for each case of drive cycle runs. The parameter does not change a lot with aged cells. Even though, the change is very small in absolute terms, in a large battery pack this variation multiples with the number of cells and cause large variations in a estimation between a new battery and a old one. The estimator used in this research is model based, and the values of the constants are taken form literature. In a experimental scenario, any random value of the constant can be assumed and the algorithm developed can then be use to converge to the real value.

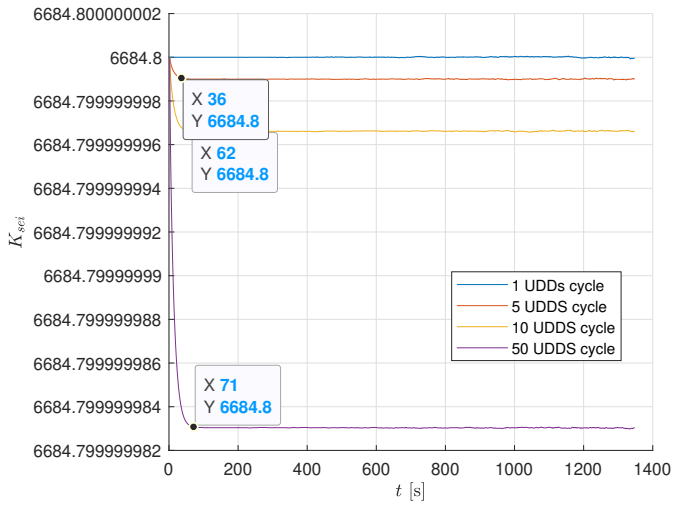

Figure 5.4: K_{sei} parameter variation with different initial conditions

Table 5.2: K_{sei} Variation with different initial conditions

K_{sei}	New Value	% change	Convergence (sec)
Actual	6684.8	0	0
1 UDDS	6684.79999999996	-5.98638E-13	0
5 UDDS	6684.79999999901	-1.48163E-11	36
10 UDDS	6684.7999999966	-5.08706E-11	62
50 UDDS	6684.79999998303	-2.53863E-10	71

In case of E_{sei} the convergence is fast and value increase with aged cells as seen in figure 5.5. Table 5.3 shows the variation of E_{sei} and the percentage change with different age d cells.

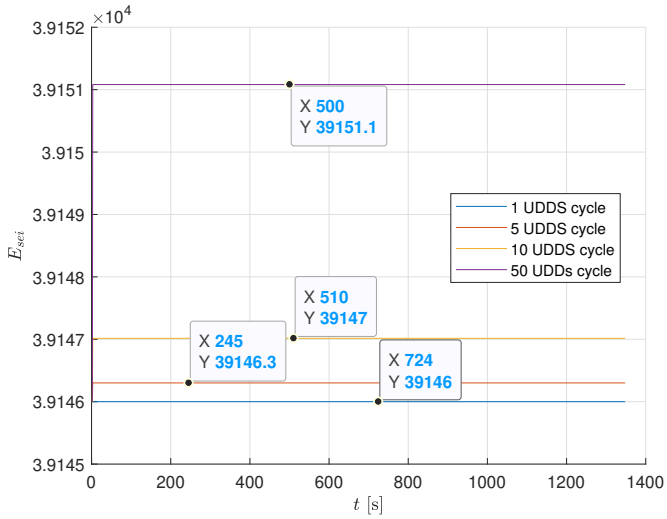

Figure 5.5: E_{sei} parameter variation with different initial conditions

Table 5.3: E_{sei} Variation with different initial conditions

E_{sei}	New Value	% change	Convergence (sec)
Actual	39146	0	0
1 UDDS	39146	0	1
5 UDDS	39146.3	0.000767	1
10 UDDS	39147.02	0.002596	1
50 UDDS	39151.08	0.012986	1

Similar to the other two par maters, $\lambda - sei$ is updated with different aged cell inputs as seen in fig. 5.6 and table 5.4 shows the % change in the value of the parameter. The convergence times are comparable to the time taken by K_{sei}.

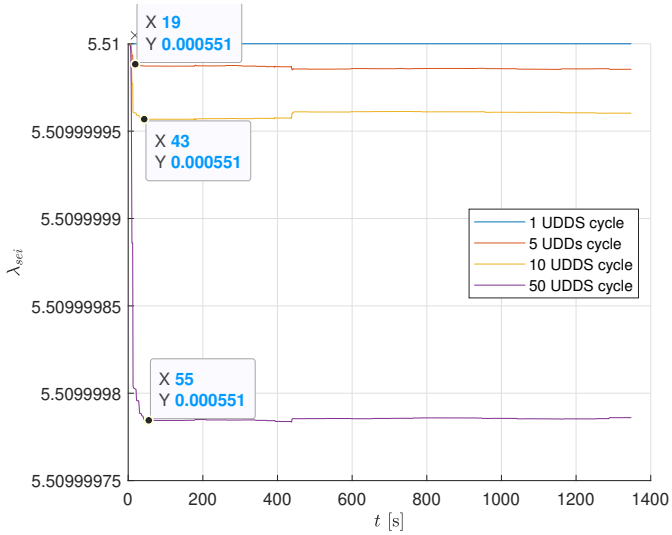

Figure 5.6: λ_{sei} parameter variation with different initial conditions

Table 5.4: λ_{sei} Variation with different initial conditions

λ_{sei}	New Value	% change	Convergence (sec)
Actual	5.5e-5	0	0
1 UDDS	5.5099e-5	0	1
5 UDDS	5.50985e-5	-2.64614E-07	19
10 UDDS	5.50960e-5	-7.20557E-07	43
50 UDDS	5.50870e-5	-3.88333E-06	55

LAM Parameter Update

in case of the parameter of LAM estimator, there is direct relationship between the estimated SOC and the applied current I_{app}, and due to these 2 noisy inputs, the parameter takes a long time to converge. In some scenarios it does not converge to a constant value as seen in figure5.7 and figure 5.8. The table for convergence and % are not made as the value of the parameter keeps changing throughout the drive cycle.

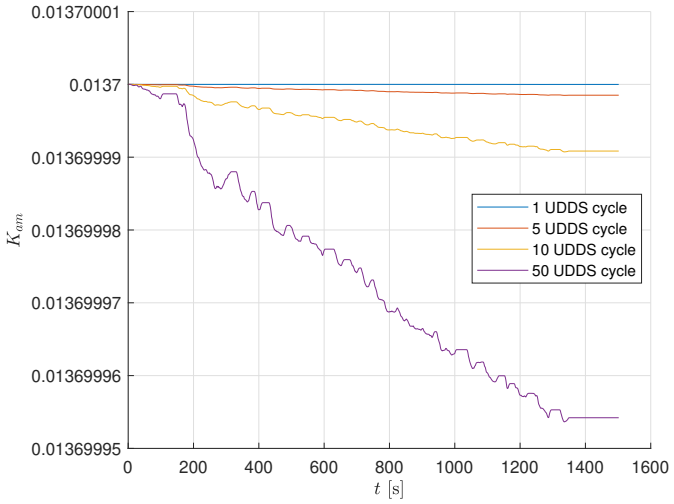

Figure 5.7: K_{am} parameter variation with different initial conditions

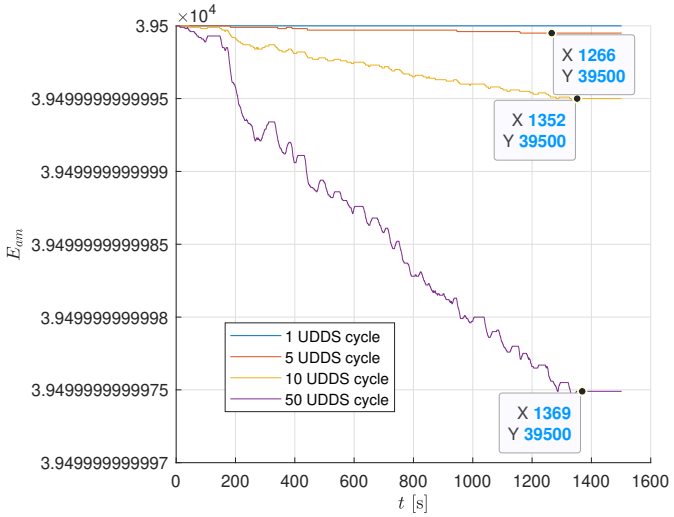

Figure 5.8: E_{am} parameter variation with different initial conditions

5.2. Summary

In this chapter, the adaptability of the estimators with changing initial conditions is discuused. The adaptability of the estimator is judged based on the convergence times with different aged cells. The SOH estimator is able to adapt to new condition in 15-20 seconds, which is acceptable for real-time applications. In later half, a new concept of using 3 kalman filters running in parallel to update the parameters of the aging models is discussed.

6

Conclusions

The aim of this research was to develop algorithms for online state of health estimation using a multi-physics reduced order models, that takes into account major degradation mechanisms and a lumped thermal model. Here the outcomes of the research questions introduced in chapter 1.2 are discuused in detail:

1. **How to estimate the SOH of a battery in real-time using adaptive control techniques ?**
   To estimate the SOH of a battery in real-time, an adaptive filtering technique called dual Kalman filters was used as discussed in Chapter 4. The culmination of the five estimators resulted in the prediction of SOH of a battery in real-time. The estimators which took noisy input form the ROM model were compared with the output of the ROM model. The SOH estimator predicted the SOH of a battery with a maximum percentage error of $<$ 5% for a 2% noisy input of applied current. All the estimators, except the Voltage estimator have there error with the confidence bounds. The Voltage estimator predicts the output with a confidence of 93%.

2. **How fast can the estimator react to changing initial states of the battery?**
   To check the robustness of the estimators and there application in a real life scenario, the estimators were provided with an initial conditions of an aged cell. Even with a old cell that has undergone aging for few UDDS cycles, the estimator is able to adapt to the changing conditions in 15-20 secs.

3. **Can the estimators be adapted to concurrently estimate both the states and the time varying cell parameters in case of an old cell? How fast can this be achieved in context of real-time estimations?**
   Section 5.1.2 in Chapter 5, a novel idea using 3 Kalman filters to parallel update the time varying cell parameters along with the estimation of states is developed. The convergence time of the parameter estimators is slower compared to aging estimators, with the maximum time of 62 secs required for the K_{sei} parameter to converge compered to the 32 secs required by SEI estimator to adapt and converge to a new value.

6.1. Recommendations for future work

The presented thesis work lays a ground work for creating a Digital twin of a battery that can predict in real time the health of a battery pack and can be implemented in Battery management systems(BMS).This section lists the areas where further investigation can be done.

1. All the estimators are build for a cell level system. The system can be extended to pack level systems taking into account cell to cell variations.

2. The current work of online estimators are model based estimators. The estimators are compared with the output of the ROM model. In future and experimental validation of this work can be taken up.

3. The initial parameters used in modelling, are taken form literature.The experimental validation of the parameters used for Physics based models is an extensive work and requires destructive techniques to verify the initial parameters. This can be a master thesis on its own.

4. Lastly, the final aim of this work is to apply the concept in a real life scenario. This can be done by implementing the algorithm used in the estimators in a micro-controller, and track the data with sensors to verify the results with a real battery pack.

References

[1] M.S. Hossain Lipu et al. “A review of state of health and remaining useful life estimation methods for lithium-ion battery in electric vehicles: Challenges and recommendations”. In: *Journal of Cleaner Production* 205 (2018), pp. 115–133. ISSN: 0959-6526. DOI: https://doi.org/10.1016/j.jclepro.2018.09.065. URL: https://www.sciencedirect.com/science/article/pii/S0959652618327793.

[2] Vinodkumar Etacheri et al. “Challenges in the development of advanced Li-ion batteries: a review”. In: *Energy Environ. Sci.* 4 (9 2011), pp. 3243–3262. DOI: 10.1039/C1EE01598B. URL: http://dx.doi.org/10.1039/C1EE01598B.

[3] Remus Teodorescu et al. “Smart Battery Technology for Lifetime Improvement”. In: *Batteries* 8.10 (Oct. 9, 2022), pp. 169–169. DOI: 10.3390/batteries8100169. URL: https://lens.org/007-706-509-348-405.

[4] Dezhen Yang et al. “A Digital Twin-Driven Life Prediction Method of Lithium-Ion Batteries Based on Adaptive Model Evolution”. In: *Materials* 15.9 (2022). ISSN: 1996-1944. DOI: 10.3390/ma15093331. URL: https://www.mdpi.com/1996-1944/15/9/3331.

[5] Michael Grieves. “Digital twin: manufacturing excellence through virtual factory replication”. In: *White paper* 1.2014 (2014), pp. 1–7.

[6] Abel Sancarlos et al. “From ROM of Electrochemistry to AI-Based Battery Digital and Hybrid Twin”. In: *Archives of Computational Methods in Engineering* 28.3 (Feb. 27, 2020). https://sam.ensam.eu/handle/10985/20776 ; https://link.springer.com/article/10.1007/s11831-020-09404-6, pp. 979–1015. DOI: 10.1007/s11831-020-09404-6. URL: https://lens.org/011-180-971-191-269.

[7] Gregory L.” ”Plett. *”Battery Management Systems, Volume 1 - Battery Modeling”*. 2th ed. USA: ”Artech House”, 2015.

[8] Xing Jin. “Aging-Aware optimal charging strategy for lithium-ion batteries: Considering aging status and electro-thermal-aging dynamics”. In: *Electrochimica Acta* 407 (2022), p. 139651. ISSN: 0013-4686. DOI: https://doi.org/10.1016/j.electacta.2021.139651. URL: https://www.sciencedirect.com/science/article/pii/S0013468621019356.

[9] Xing Jin et al. “Physically-based reduced-order capacity loss model for graphite anodes in Li-ion battery cells”. In: *Journal of Power Sources* 342 (2017), pp. 750–761. ISSN: 0378-7753. DOI: https://doi.org/10.1016/j.jpowsour.2016.12.099. URL: https://www.sciencedirect.com/science/article/pii/S037877531631802X.

[10] Marcelo A. Xavier et al. “A Computational Framework for Lithium Ion Cell-Level Model Predictive Control Using a Physics-Based Reduced-Order Model”. In: *IEEE Control Systems Letters* 5.4 (2021), pp. 1387–1392. DOI: 10.1109/LCSYS.2020.3038131.

[11] Hao Mu and Rui Xiong. “Chapter 1 - Modeling, Evaluation, and State Estimation for Batteries”. In: *Modeling, Dynamics and Control of Electrified Vehicles*. Ed. by Hui Zhang, Dongpu Cao, and Haiping Du. Woodhead Publishing, 2018, pp. 1–38. ISBN: 978-0-12-812786-5. DOI: https://doi.org/10.1016/B978-0-12-812786-5.00001-X. URL: https://www.sciencedirect.com/science/article/pii/B978012812786500001X.

[12] Qian Wang et al. “A critical review of thermal management models and solutions of lithium-ion batteries for the development of pure electric vehicles”. In: *Renewable and Sustainable Energy Reviews* 64 (2016), pp. 106–128. ISSN: 1364-0321. DOI: https://doi.org/10.1016/j.rser.2016.05.033. URL: https://www.sciencedirect.com/science/article/pii/S1364032116301435.

[13] Yuejiu Zheng et al. “Investigating the error sources of the online state of charge estimation methods for lithium-ion batteries in electric vehicles”. In: *Journal of Power Sources* 377 (2018), pp. 161–188. ISSN: 0378-7753. DOI: https://doi.org/10.1016/j.jpowsour.2017.11.094. URL: https://www.sciencedirect.com/science/article/pii/S037877531731594X.

[14] J-M Tarascon and Michel Armand. “Issues and challenges facing rechargeable lithium batteries”. In: *nature* 414.6861 (2001), pp. 359–367.

[15] Yuanzheng Long et al. “Molten lithium metal battery with Li4Ti5O12 cathode and solid electrolyte”. In: *eTransportation* 16 (2023), p. 100235. ISSN: 2590-1168. DOI: https://doi.org/10.1016/j.etran.2023.100235. URL: https://www.sciencedirect.com/science/article/pii/S2590116823000103.

[16] Bruce Dunn, Haresh Kamath, and Jean-Marie Tarascon. “Electrical Energy Storage for the Grid: A Battery of Choices”. In: *Science* 334.6058 (2011), pp. 928–935. DOI: 10.1126/science.1212741. eprint: https://www.science.org/doi/pdf/10.1126/science.1212741. URL: https://www.science.org/doi/abs/10.1126/science.1212741.

[17] Naoki Nitta et al. “Li-ion battery materials: present and future”. In: *Materials Today* 18.5 (2015), pp. 252–264. ISSN: 1369-7021. DOI: https://doi.org/10.1016/j.mattod.2014.10.040. URL: https://www.sciencedirect.com/science/article/pii/S1369702114004118.

[18] Zachary P Ding Yuanli. “Automotive Li-Ion Batteries: Current Status and Future Perspectives”. In: *Electrochemical Energy Reviews* 2.1 (2019), pp. 1–28. ISSN: 2520-8136. DOI: https://doi.org/10.1007/s41918-018-0022-z.

[19] Manh-Kien Tran et al. “Comparative Study of Equivalent Circuit Models Performance in Four Common Lithium-Ion Batteries: LFP, NMC, LMO, NCA”. In: *Batteries* 7.3 (2021). ISSN: 2313-0105. DOI: 10.3390/batteries7030051. URL: https://www.mdpi.com/2313-0105/7/3/51.

[20] Yu Miao et al. “Current Li-Ion Battery Technologies in Electric Vehicles and Opportunities for Advancements”. In: *Energies* 12.6 (2019). ISSN: 1996-1073. DOI: 10.3390/en12061074. URL: https://www.mdpi.com/1996-1073/12/6/1074.

[21] Fredrick Omenya et al. “Comparative Study Nickel Rich Layered Oxides: NMC 622, NMC 811 and NCA Cathode Materials for Lithium Ion Battery”. In: *ECS Meeting Abstracts* MA2018-01.3 (Apr. 2018), p. 531. DOI: 10.1149/MA2018-01/3/531. URL: https://dx.doi.org/10.1149/MA2018-01/3/531.

[22] Buchmann, I. (2021). *Batteryuniversity*. 2023. URL: https://batteryuniversity.com/article/bu-205-types-of-lithium-ion.

[23] Xuebing Han et al. “A review on the key issues of the lithium ion battery degradation among the whole life cycle”. In: *eTransportation* 1 (2019), p. 100005. ISSN: 2590-1168. DOI: https://doi.org/10.1016/j.etran.2019.100005. URL: https://www.sciencedirect.com/science/article/pii/S2590116819300050.

[24] Christoph R. Birkl et al. “Degradation diagnostics for lithium ion cells”. In: *Journal of Power Sources* 341 (2017), pp. 373–386. ISSN: 0378-7753. DOI: https://doi.org/10.1016/j.jpowsour.2016.12.011. URL: https://www.sciencedirect.com/science/article/pii/S0378775316316998.

[25] Carlos Pastor-Fernández et al. “Critical review of non-invasive diagnosis techniques for quantification of degradation modes in lithium-ion batteries”. In: *Renewable and Sustainable Energy Reviews* 109 (2019), pp. 138–159. ISSN: 1364-0321. DOI: https://doi.org/10.1016/j.rser.2019.03.060. URL: https://www.sciencedirect.com/science/article/pii/S136403211930200X.

[26] J. Vetter et al. “Ageing mechanisms in lithium-ion batteries”. In: *Journal of Power Sources* 147.1 (2005), pp. 269–281. ISSN: 0378-7753. DOI: https://doi.org/10.1016/j.jpowsour.2005.01.006. URL: https://www.sciencedirect.com/science/article/pii/S0378775305000832.

[27] Wiljan Vermeer, Gautham Ram Chandra Mouli, and Pavol Bauer. “A Comprehensive Review on the Characteristics and Modeling of Lithium-Ion Battery Aging”. In: *IEEE Transactions on Transportation Electrification* 8.2 (2022), pp. 2205–2232. DOI: 10.1109/TTE.2021.3138357.

[28] Gregory L. Plett. “Extended Kalman filtering for battery management systems of LiPB-based HEV battery packs: Part 2. Modeling and identification”. In: *Journal of Power Sources* 134.2 (2004), pp. 262–276. ISSN: 0378-7753. DOI: https://doi.org/10.1016/j.jpowsour.2004.02.032. URL: https://www.sciencedirect.com/science/article/pii/S037877530400360X.

[29] Jorn M. Reniers, Grietus Mulder, and David A. Howey. “Review and Performance Comparison of Mechanical-Chemical Degradation Models for Lithium-Ion Batteries”. In: *Journal of The Electrochemical Society* 166.14 (Sept. 2019), A3189. DOI: 10.1149/2.0281914jes. URL: https://dx.doi.org/10.1149/2.0281914jes.

[30] Jinhao Meng et al. “Overview of Lithium-Ion Battery Modeling Methods for State-of-Charge Estimation in Electrical Vehicles”. In: *Applied Sciences* 8.5 (2018). ISSN: 2076-3417. DOI: 10.3390/app8050659. URL: https://www.mdpi.com/2076-3417/8/5/659.

[31] Haihong Pan et al. “Novel battery state-of-health online estimation method using multiple health indicators and an extreme learning machine”. In: *Energy* 160 (2018), pp. 466–477. ISSN: 0360-5442. DOI: https://doi.org/10.1016/j.energy.2018.06.220. URL: https://www.sciencedirect.com/science/article/pii/S0360544218312854.

[32] Duo Yang et al. “State-of-health estimation for the lithium-ion battery based on support vector regression”. In: *Applied Energy* 227 (2018). Transformative Innovations for a Sustainable Future – Part III, pp. 273–283. ISSN: 0306-2619. DOI: https://doi.org/10.1016/j.apenergy.2017.08.096. URL: https://www.sciencedirect.com/science/article/pii/S0306261917311169.

[33] Kailong Liu et al. “Modified Gaussian Process Regression Models for Cyclic Capacity Prediction of Lithium-Ion Batteries”. In: *IEEE Transactions on Transportation Electrification* 5.4 (2019), pp. 1225–1236. DOI: 10.1109/TTE.2019.2944802.

[34] Mohammad Charkhgard and Mohammad Farrokhi. “State-of-charge estimation for lithium-ion batteries using neural networks and EKF”. In: *IEEE transactions on industrial electronics* 57.12 (2010), pp. 4178–4187.

[35] Jinhao Meng, Guangzhao Luo, and Fei Gao. “Lithium polymer battery state-of-charge estimation based on adaptive unscented Kalman filter and support vector machine”. In: *IEEE Transactions on Power Electronics* 31.3 (2015), pp. 2226–2238.

[36] Shunli Wang et al. “Chapter 2 - Electrical equivalent circuit modeling”. In: *Battery System Modeling*. Ed. by Shunli Wang et al. Elsevier, 2021, pp. 47–94. ISBN: 978-0-323-90472-8. DOI: https://doi.org/10.1016/B978-0-323-90472-8.00008-1. URL: https://www.sciencedirect.com/science/article/pii/B9780323904728000081.

[37] S. Nejad, D.T. Gladwin, and D.A. Stone. “A systematic review of lumped-parameter equivalent circuit models for real-time estimation of lithium-ion battery states”. In: *Journal of Power Sources* 316 (2016), pp. 183–196. ISSN: 0378-7753. DOI: https://doi.org/10.1016/j.jpowsour.2016.03.042. URL: https://www.sciencedirect.com/science/article/pii/S0378775316302427.

[38] Michael A. Roscher and Dirk Uwe Sauer. “Dynamic electric behavior and open-circuit-voltage modeling of LiFePO4-based lithium ion secondary batteries”. In: *Journal of Power Sources* 196.1 (2011), pp. 331–336. ISSN: 0378-7753. DOI: https://doi.org/10.1016/j.jpowsour.2010.06.098. URL: https://www.sciencedirect.com/science/article/pii/S0378775310010852.

[39] T. Huria, G. Ludovici, and G. Lutzemberger. “State of charge estimation of high power lithium iron phosphate cells”. In: *Journal of Power Sources* 249 (2014), pp. 92–102. ISSN: 0378-7753. DOI: https://doi.org/10.1016/j.jpowsour.2013.10.079. URL: https://www.sciencedirect.com/science/article/pii/S037877531301745X.

[40] Shuoqin Wang et al. “Power prediction from a battery state estimator that incorporates diffusion resistance”. In: *Journal of Power Sources* 214 (2012), pp. 399–406. ISSN: 0378-7753. DOI: https://doi.org/10.1016/j.jpowsour.2012.04.070. URL: https://www.sciencedirect.com/science/article/pii/S037877531200804X.

[41] Guangzhong Dong, Jingwen Wei, and Zonghai Chen. “Kalman filter for onboard state of charge estimation and peak power capability analysis of lithium-ion batteries”. In: *Journal of Power Sources* 328 (2016), pp. 615–626. ISSN: 0378-7753. DOI: https://doi.org/10.1016/j.jpowsour.2016.08.065. URL: https://www.sciencedirect.com/science/article/pii/S0378775316310746.

[42] Changfu Zou et al. “Power capability prediction for lithium-ion batteries using economic nonlinear model predictive control”. In: *Journal of Power Sources* 396 (2018), pp. 580–589. ISSN: 0378-7753. DOI: https://doi.org/10.1016/j.jpowsour.2018.06.034. URL: https://www.sciencedirect.com/science/article/pii/S037877531830630X.

[43] Mona Faraji Niri et al. “State of Power Prediction for Lithium-Ion Batteries in Electric Vehicles via Wavelet-Markov Load Analysis”. In: *IEEE Transactions on Intelligent Transportation Systems* 22.9 (2021), pp. 5833–5848. DOI: 10.1109/TITS.2020.3028024.

[44] Changhe Liu et al. “State of power estimation of lithium-ion battery based on fractional-order equivalent circuit model”. In: *Journal of Energy Storage* 41 (2021), p. 102954. ISSN: 2352-152X. DOI: https://doi.org/10.1016/j.est.2021.102954. URL: https://www.sciencedirect.com/science/article/pii/S2352152X21006691.

[45] Marie-Therese von Srbik et al. “A physically meaningful equivalent circuit network model of a lithium-ion battery accounting for local electrochemical and thermal behaviour, variable double layer capacitance and degradation”. In: *Journal of Power Sources* 325 (2016), pp. 171–184. ISSN: 0378-7753. DOI: https://doi.org/10.1016/j.jpowsour.2016.05.051. URL: https://www.sciencedirect.com/science/article/pii/S0378775316305973.

[46] Mehdi Jafari, Khalid Khan, and Lucia Gauchia. “Deterministic models of Li-ion battery aging: It is a matter of scale”. In: *Journal of Energy Storage* 20 (2018), pp. 67–77. ISSN: 2352-152X. DOI: https://doi.org/10.1016/j.est.2018.09.002. URL: https://www.sciencedirect.com/science/article/pii/S2352152X18303098.

[47] Marc Doyle, Thomas F. Fuller, and John Newman. “Modeling of Galvanostatic Charge and Discharge of the Lithium/Polymer/Insertion Cell”. In: *Journal of The Electrochemical Society* 140.6 (June 1993), p. 1526. DOI: 10.1149/1.2221597. URL: https://dx.doi.org/10.1149/1.2221597.

[48] Weilin Luo et al. “An approximate solution for electrolyte concentration distribution in physics-based lithium-ion cell models”. In: *Microelectronics Reliability* 53.6 (2013), pp. 797–804. ISSN: 0026-2714. DOI: https://doi.org/10.1016/j.microrel.2012.11.002. URL: https://www.sciencedirect.com/science/article/pii/S0026271412005100.

[49] James Marcicki et al. “Design and parametrization analysis of a reduced-order electrochemical model of graphite/LiFePO4 cells for SOC/SOH estimation”. In: *Journal of Power Sources* 237 (2013), pp. 310–324. ISSN: 0378-7753. DOI: https://doi.org/10.1016/j.jpowsour.2012.12.120. URL: https://www.sciencedirect.com/science/article/pii/S0378775313000694.

[50] Meng Guo, Godfrey Sikha, and Ralph E. White. “Single-Particle Model for a Lithium-Ion Cell: Thermal Behavior”. In: *Journal of The Electrochemical Society* 158.2 (Dec. 2010), A122. DOI: 10.1149/1.3521314. URL: https://dx.doi.org/10.1149/1.3521314.

[51] Vijayasekaran Boovaragavan, S. Harinipriya, and Venkat R. Subramanian. “Towards real-time (milliseconds) parameter estimation of lithium-ion batteries using reformulated physics-based models”. In: *Journal of Power Sources* 183.1 (2008), pp. 361–365. ISSN: 0378-7753. DOI: https://doi.org/10.1016/j.jpowsour.2008.04.077. URL: https://www.sciencedirect.com/science/article/pii/S0378775308008409.

[52] Saeed Khaleghi Rahimian, Sean Rayman, and Ralph E. White. “Extension of physics-based single particle model for higher charge–discharge rates”. In: *Journal of Power Sources* 224 (2013), pp. 180–194. ISSN: 0378-7753. DOI: https://doi.org/10.1016/j.jpowsour.2012.09.084. URL: https://www.sciencedirect.com/science/article/pii/S0378775312015054.

[53] Xiaoyu Li et al. “A simplified multi-particle model for lithium ion batteries via a predictor-corrector strategy and quasi-linearization”. In: *Energy* 116 (2016), pp. 154–169. ISSN: 0360-5442. DOI: https://doi.org/10.1016/j.energy.2016.09.099. URL: https://www.sciencedirect.com/science/article/pii/S036054421631369X.

[54] Guodong Fan et al. “Modeling of Li-Ion Cells for Fast Simulation of High C-Rate and Low Temperature Operations”. In: *Journal of The Electrochemical Society* 163.5 (Feb. 2016), A666. DOI: 10.1149/2.0761605jes. URL: https://dx.doi.org/10.1149/2.0761605jes.

[55] Ali Jokar et al. “An Inverse Method for Estimating the Electrochemical Parameters of Lithium-Ion Batteries”. In: *Journal of The Electrochemical Society* 163.14 (Oct. 2016), A2876. DOI: 10.1149/2.0191614jes. URL: https://dx.doi.org/10.1149/2.0191614jes.

[56] Thomas F. Fuller, Marc Doyle, and John Newman. “Simulation and Optimization of the Dual Lithium Ion Insertion Cell”. In: *Journal of The Electrochemical Society* 141.1 (Jan. 1994), p. 1. DOI: 10.1149/1.2054684. URL: https://dx.doi.org/10.1149/1.2054684.

[57] Paulo Kemper, Shengbo Eben Li, and Dongsuk Kum. “Simplification of pseudo two dimensional battery model using dynamic profile of lithium concentration”. In: *Journal of Power Sources* 286 (2015), pp. 510–525. ISSN: 0378-7753. DOI: https://doi.org/10.1016/j.jpowsour.2015.03.134. URL: https://www.sciencedirect.com/science/article/pii/S0378775315005583.

[58] E. Miguel et al. “Electrochemical Model and Sigma Point Kalman Filter Based Online Oriented Battery Model”. In: *IEEE Access* 9 (2021), pp. 98072–98090. DOI: 10.1109/ACCESS.2021.3095620.

[59] Valentin Sulzer et al. “Python Battery Mathematical Modelling (PyBaMM)”. In: *Journal of Open Research Software* 9.1 (2021), p. 14. DOI: 10.5334/jors.309.

[60] Weilin Luo et al. “A new extension of physics-based single particle model for higher charge–discharge rates”. In: *Journal of Power Sources* 241 (2013), pp. 295–310. ISSN: 0378-7753. DOI: https://doi.org/10.1016/j.jpowsour.2013.04.129. URL: https://www.sciencedirect.com/science/article/pii/S0378775313007398.

[61] Ahmed H. Sameh and Walter L. Heimerdinger. “On the identification of multi-output linear time-invariant and periodic dynamic systems”. In: *Computers & Electrical Engineering* 1.3 (1973), pp. 341–359. ISSN: 0045-7906. DOI: https://doi.org/10.1016/0045-7906(73)90003-7. URL: https://www.sciencedirect.com/science/article/pii/0045790673900037.

[62] Xing Jin and Chang Liu. “Physics-based control-oriented reduced-order degradation model for LiNiMnCoO2 - graphite cell”. In: *Electrochimica Acta* 312 (2019), pp. 188–201. ISSN: 0013-4686. DOI: https://doi.org/10.1016/j.electacta.2019.04.109. URL: https://www.sciencedirect.com/science/article/pii/S0013468619307972.

[63] Mohammadhosein Safari and Charles Delacourt. “Aging of a commercial graphite/LiFePO4 cell”. In: *Journal of The Electrochemical Society* 158 (Oct. 2011), A1123–A1135. DOI: 10.1149/1.3614529.

[64] William H. Woodford, Yet-Ming Chiang, and W. Craig Carter. ““Electrochemical Shock” of Intercalation Electrodes: A Fracture Mechanics Analysis”. In: *Journal of The Electrochemical Society* 157.10 (Aug. 2010), A1052. DOI: 10.1149/1.3464773. URL: https://dx.doi.org/10.1149/1.3464773.

[65] Robert R. Richardson and David A. Howey. “Sensorless Battery Internal Temperature Estimation Using a Kalman Filter With Impedance Measurement”. In: *IEEE Transactions on Sustainable Energy* 6.4 (2015), pp. 1190–1199. DOI: 10.1109/TSTE.2015.2420375.

[66] Yuantao Cui et al. “Thermal and ionic conductivity studies of lithium aluminum germanium phosphate solid-state electrolyte”. In: *Solid State Ionics* 289 (2016), pp. 125–132. ISSN: 0167-2738. DOI: https://doi.org/10.1016/j.ssi.2016.03.007. URL: https://www.sciencedirect.com/science/article/pii/S0167273816300522.

[67] Caihao Weng, Jing Sun, and Huei Peng. “A unified open-circuit-voltage model of lithium-ion batteries for state-of-charge estimation and state-of-health monitoring”. In: *Journal of Power Sources* 258 (2014), pp. 228–237. ISSN: 0378-7753. DOI: https://doi.org/10.1016/j.jpowsour.2014.02.026. URL: https://www.sciencedirect.com/science/article/pii/S0378775314002092.

[68] Shengbo Eben Li et al. “An electrochemistry-based impedance model for lithium-ion batteries”. In: *Journal of Power Sources* 258 (2014), pp. 9–18. ISSN: 0378-7753. DOI: https://doi.org/10.1016/j.jpowsour.2014.02.045. URL: https://www.sciencedirect.com/science/article/pii/S0378775314002298.

[69] M. Landi and G. Gross. “Measurement techniques for online battery state of health estimation in vehicle-to-grid applications”. English. In: *IEEE Transactions on Instrumentation and Measurement* 63.5 (2014). Cited By :76, pp. 1224–1234. URL: www.scopus.com.

[70] Mahammad A. Hannan et al. “Neural Network Approach for Estimating State of Charge of Lithium-Ion Battery Using Backtracking Search Algorithm”. In: *IEEE Access* 6 (2018), pp. 10069–10079. DOI: 10.1109/ACCESS.2018.2797976.

[71] Thomas G. Tranter et al. “liionpack: A Python package for simulating packs of batteries with PyBaMM”. In: *Journal of Open Source Software* 7.70 (2022), p. 4051. DOI: 10.21105/joss.04051. URL: https://doi.org/10.21105/joss.04051.

A

Appendix

A.1. Battery Model parameters (LGM50 5 Ah NMC cell)

Table A.1: List of Whole cell constants LGM50 (NMC cell) 1[7]

Constants			
Parameter	**Name**	**Value**	**Unit**
Electrode Plate Area	A_{cell}	0.1027	[m2]
V_{cell},min	V	2.5	[V]
V_{cell},max	V	4.2	[V]
Q_{cap}	Q	5	[A.h]
Reference Temperature	T_{ref}	298.15	[K]
Catonic Transference Number	t_+^0	0.2594	[unitless]
Activation Energy Electrolyte Diffusivity	E_{De}	0	[J mol-1]
Electrolyte Diffusivity at Tref	De_{ref}	1.77E-10	[m2 s-1]
Activation Energy Electrolyte Conductivity	E_{kappa}	0	[J mol-1]
Initial Concentration of Electrolyte	Ce_0	1000	[mol m-3]

Table A.2: List of LGM50 cell separator parameters [7]

Separator			
Parameter	**Name**	**Value**	**Unit**
Length of Separator	L	0.000012	[m]
Electrolyte Phase Volume Fraction	ϵ_e	0.47	[unitless]
Bruggeman Coefficient for De	De^{brug}	1.5	[unitless]
Bruggeman Coefficient for kappa	k^{brug}	1.5	[unitless]
Bruggeman Coefficient for kappaD	k_d^{brug}	1.5	[unitless]

Table A.3: List of cell parameters for simulation (LGM50) [7]

		Positive Electrode	Negative Electrode	
Parameter	**Symbol**	**Value**	**Value**	**Unit**
Activation Energy Reaction Rate	E_k	17800	35000	[J mol-1]
Normalized reaction rate coefficient	k_{norm}^{ref}	3.544E-11	6.716E-12	[mol m-2 s-1]
Activation Energy Solid Conductivity	E_σ	0	0	[J mol-1]
Solid Phase Conductivity	σ_{ref}	0.18	215	[S m-1]
Activation Energy Solid Diffusivity	E_{Ds}	0	0	[J mol-1]
Solid Diffusivity at Tref	Ds_{ref}	4E-15	3.3E-14	[m2 s-1]
Particle Radius	R_s	0.00000522	0.00000586	[m]
Length of Electrode	L	0.0000756	0.0000852	[m]
Solid Phase Volume Fraction	ϵ_s	0.665	0.75	[unitless]
Electrolyte Phase Volume Fraction	ϵ_e	0.335	0.25	[unitless]
Max Solid Phase Concentration	$C_{s,max}$	22860	33133	[mol m-3]
Electrode Stoichiometry at 0% SOC	θ_0	0.8539	0.0263	[unitless]
Electrode Stoichiometry at 100% SOC	θ_{100}	0.2638	0.910612	[unitless]
Charge Transfer Coefficient	α	0.5	0.5	[unitless]
Film Resistance	R_{film}	0	0	[Ω m2]
Bruggeman Coefficient for De	De^{brug}	1.5	1.5	[unitless]
Bruggeman Coefficient for sigma	σ^{brug}	1	1	[unitless]
Bruggeman Coefficient for kappa	k^{brug}	1.5	1.5	[unitless]
Bruggeman Coefficient for kappaD	k_d^{brug}	1.5	1.5	[unitless]

In the electrolyte, conductivity is a function of concentration:

$$\kappa(c_e) = 4.1253 * 10^{-2} + 5.007 * 10^{-4} c_e - 4.7212 * 10^{-7} c_e^2 + 1.5094 * 10^{-10} c_e^3 - 1.6018 * 10^{-14} c_e^4 \quad \text{(A.1)}$$

For the negative electrode, the open circuit potential function is:

$$U_{ocp}^{neg}(\theta) = -0.16 + 1.32 * \exp(-3\theta) + 10 * \exp(-2000\theta) \quad \text{(A.2)}$$

For the positive electrode, the open circuit potential function is:

$$U_{ocp}^{pos}(\theta) = 4.19829 + 0.0565661 * \tanh(-14.5546\theta + 8.60942) - 0.0275479[\frac{1}{(0.9984 - \theta)^{0.4924}} - 1.901] - 0.15723 * \exp(-0.0473\theta^6) + 0.8102 * \exp[-40(\theta - 0.1338)] \quad \text{(A.3)}$$

A.2. Definitions

There are many ambiguous terms to describe the state and properties of battery cells. This can lead to misinterpretation of the results or comparing results with different properties. In this paragraph the terms used in this thesis will be defined.

1. **State of Health (SOH)**: The state of health (SoH) of a battery is a subjective term and mainly depends on the application. The SoH indicates the state of the battery between the beginning of life (BoL) and end of life (EoL) in percentages. The EoL of a battery is reached when the battery cannot perform according to the minimum requirements. For EV applications this is defined by the battery manufacturers when one of the following conditions has been fulfilled :
    - The capacity of a battery under reference conditions has dropped to 80% compared to the rated capacity under reference conditions. This is known as capacity fading.
    - The maximum power delivered by the battery under reference conditions has dropped to 80% compared to the rated power under reference conditions. This is known as power fading
2. **State of Charge (SOC)**: The state of charge (SoC) indicates the amount of charge in Amp□hours left in the battery. The SoC can be divided into two types: engineering□SoC (e□SoC) and thermodynamic□SoC (t□SoC). The e□SoC is the SoC apparent to the user of the battery and is rate dependent; it is the state of the capacity at a certain discharge rate, so different discharge rates

will result in a different e□SoC at the same amount of charge in the battery. The t□SoC is the SoC of a battery defined by the thermodynamic properties in the cell and can be determined by the open□circuit voltage of the battery; it is the state of the useable capacity in the cell.

3. **Cell Capacity:** The apparent capacity of the cell is the rate dependent capacity experienced by the user. This capacity is strongly dependent on the internal impedance of the cell and varies extensively depending on the operating conditions. On the other hand, the useable capacity is the amount of charge the battery contains and is not rate dependent. It is the theoretically possible amount of charge that can be discharged from a fully charged cell with an infinitely small current for a given minimum cell voltage, so that the voltage drop over the internal resistance becomes close to zero. Both definitions of capacity are dependent on the temperature. Since the internal resistance voltage drop causes the battery to reach the minimum voltage before 0% SoC, it will not be possible to use the complete useable capacity.
4. **Depth of Discharge(DOD) :** The depth of discharge (DoD) of the battery is generally defined as the amount of charge removed from a fully charged cell in percentages. Based on the DoD, the number of possible cycles before the EoL of a cell is estimated.
5. **C-rate** The C□rate is a measure for the current of a battery cell and is scaled to the nominal capacity of a cell stated by the manufacturer at reference conditions. The current level that a battery cell can discharge at depends on the capacity of the battery. A current of 1C means that the battery cell is ideally charged or discharged in one hour, C/2 in two hours and 2C in half an hour. So a current of 1C for a cell with nominal capacity of 160Ah is 160A and 1C for a 10Ah cell is 10A.
6. **Energy Throughput :** The energy throughput is the total amount of energy that can be charged and discharged within the lifetime of batteries [**khojasteh_faria_vale_2021**].

A.3. Additional degradation results of main model (pybamm)

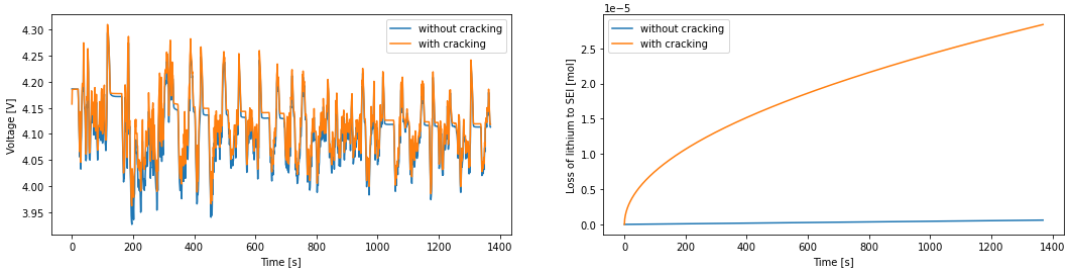

Figure A.1: SEI degradation with and without cracks

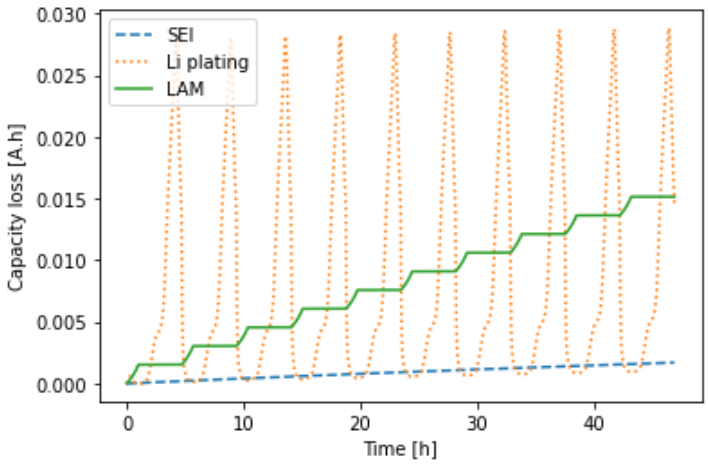

Figure A.2: Comparison of different degradation for 40 hours

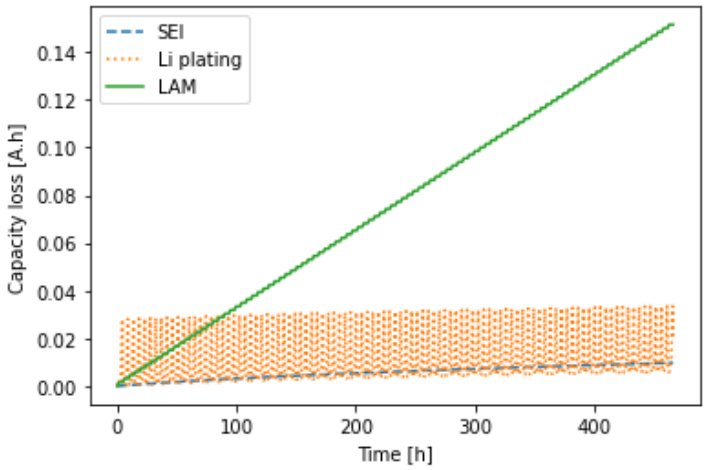

Figure A.3: Comparison of different degradation for 400 hours

A.4. Transfer Functions

$$\frac{\tilde{C}_{s,e}(z,s)}{I_{app}} = \left(\frac{\nu(s)R_s(z-1)}{a_s F L_n A(k^{eff}+\sigma^{eff})} \times \frac{\sigma^{eff}cosh(\nu(s).z)+k^{eff}cosh(\nu(s))}{sinh(\nu(s))} \times \frac{tanh(\beta)}{(tanh(\beta)-\beta)}\right) \tag{A.4}$$

where $\tilde{C}_{s,e}$ is the debaised surface concentration defined as $\tilde{C}_{s,e} = C_{se} - C_{s,0}$ and $\beta = R_s\sqrt{\frac{s}{D_s}}$. 'z' is defined as the spatial electrode location, and 's' is the complex frequency domain. $\nu(s)$ is a dimensionless quantity, defined as

$$\nu(s) = L_n\sqrt{\frac{a_s(\frac{1}{\sigma^{eff}})+(\frac{1}{k^{eff}})}{R_{tot}+|\frac{\partial U_k}{\partial C_{s,e}}|\frac{R_s}{FD_s}(\frac{tanh(\beta)}{tanh(\beta)-\beta})}} \tag{A.5}$$

The reaction flux transfer function can then be derived by combining the results obtained through the linearised Butler–Volmer Eq. 2.7 and solid phase charge conservation Eq. 2.8.

$$\frac{J(z,s)}{I_{app}(s)} = \left(\frac{\nu(s)}{a_s F L_n A(k^{eff}+\sigma^{eff})} \times \frac{\sigma^{eff}cosh(\nu(s).z)+k^{eff}cosh(\nu(s)(z-1))}{sinh(\nu(s))}\right) \tag{A.6}$$

The corresponding solid potential ϕ_s transfer function is,

$$\frac{\phi_s(z,s)}{I_{app}(s)} = -\frac{L_n k^{eff}(cosh(z-1)\nu(s))}{A\sigma^{eff}(k^{eff}+\sigma^{eff})\nu(s)sinh(\nu(s))} - \frac{L_n\sigma^{eff}(1-cosh(z\nu(s)))+z\nu(s)sinh(\nu(s))}{A\sigma^{eff}(k^{eff}+\sigma^{eff})\nu(s)sinh(\nu(s))} \tag{A.7}$$

In order to generate an ionic current representation, integrate electrolyte charge conservation Eq. 3.11 with the prior reaction flux transfer function to determine the electrolyte potential. This procedure results in a two-term representation, which is displayed and discussed in more detail below.

$$\frac{\tilde{\phi_e}(z,s)}{I_{app}} = [\tilde{\phi_e}(z,s)]_1 + [\tilde{\phi_e}(z,s)]_2 \tag{A.8}$$

where the first term is dependent on positive electrode domain, while the second term is determined by the value of $C_e(x,t)$ at any given instance.

The last step is to acquire the electrolyte concentration transfer function, which is the summation of negative electrode reaction flux and positive electrode reaction flux, and is given by,

$$\frac{C_{e,k}(x,s))}{I_{app}(s)} = \frac{1}{s+\lambda_k}\left[\frac{j_k^{neg}(s)}{I_{app}} + \frac{j_k^{pos}(s)}{I_{app}}\right] \tag{A.9}$$

where, λ_k are the eigen values obtained via the root finding method.

A.5. Pack level Modeling

Figure A.4 shows an equivalent circuit with 4 cells in parallel. the circuit also shows internal resistances of the cells and busbar resistances to model to cell to cell variations [71].

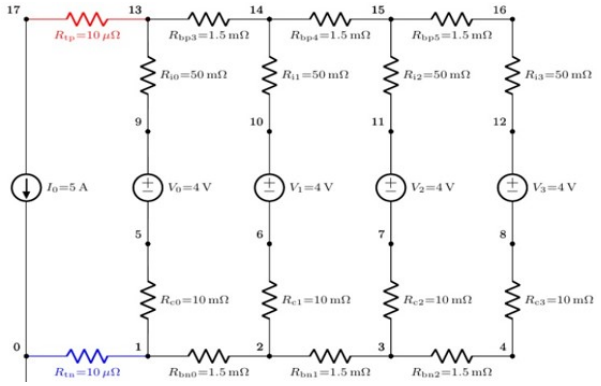

Figure A.4: A circuit diagram of a pack with 4 parallel cells showing internal resistances and busbar resistances

Figure A.5 illustrates the algorithm for solving the coupled system of cells .Each battery's current balance and boundary conditions are predetermined for the following time-step by time-steps.The initial current flow through each DFN model is assumed to be equal to the terminal current scaled by the ratio of the current collector segment length to the total current collector length. The DFN models are all initialised at the same state-of-charge. Under these circumstances, the models are run for a single, extremely brief time step of 1 s, and the local over potentials are divided by the local currents to obtain the local equivalent resistance in accordance with Ohm's law. By repeatedly modifying the global terminal voltage until the total current equals the desired applied terminal current, these resistances are utilised to update the resistor network. This new local current is then used as an input to the DFN model. The thermal problem is solved in a non-coupled way with each battery acting as an independent heat source and interacting with its environment in a "lumped" sense with a volume-averaged heat transfer coefficient. The change in local current changes the temperature of each cell and causing variation in other parameters, thus getting the cell to cell variation desired.

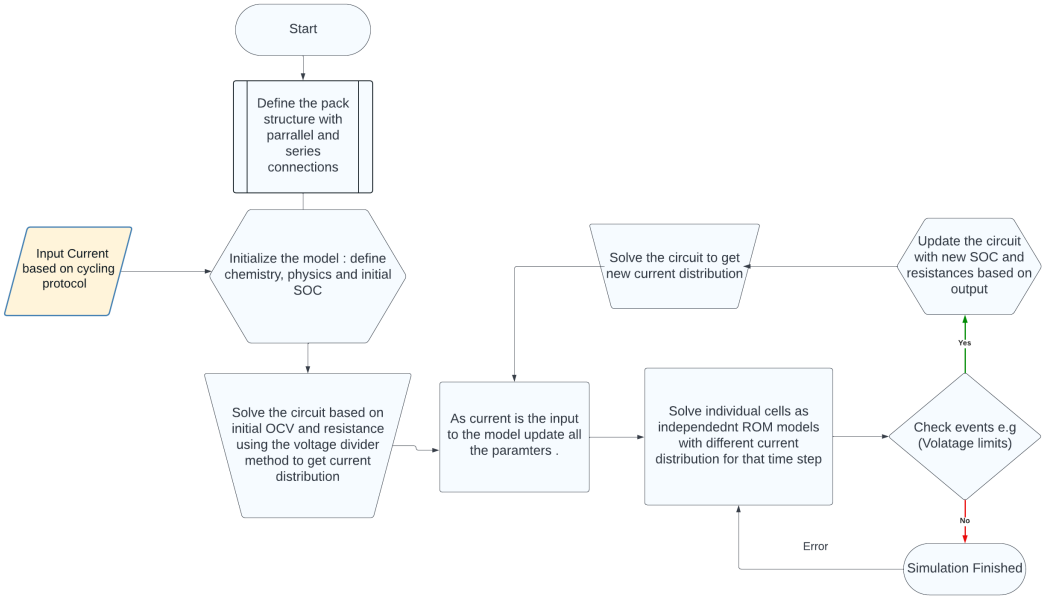

Figure A.5: Flowchart of pack-level modeling

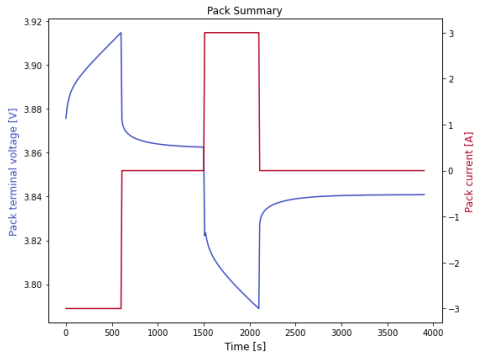

(a) NMC battery pack terminal voltage and current

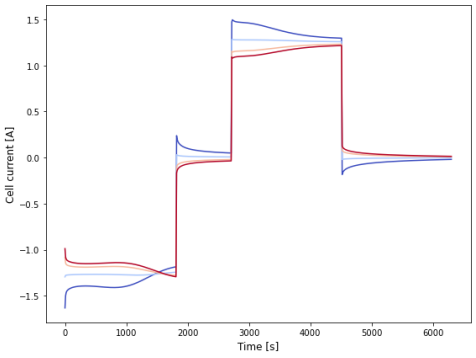

(b) NMC battery pack current

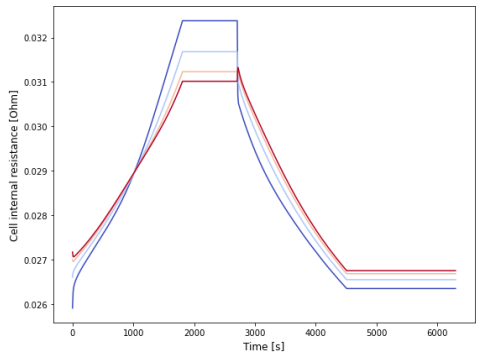

(c) NMC battery pack internal resistance

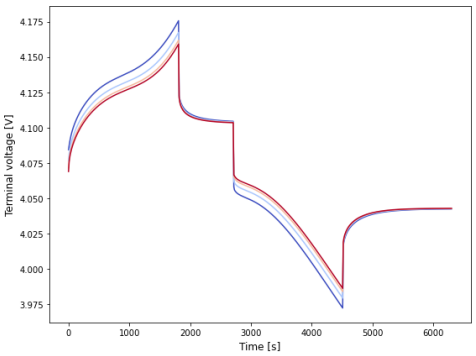

(d) NMC battery cell voltage

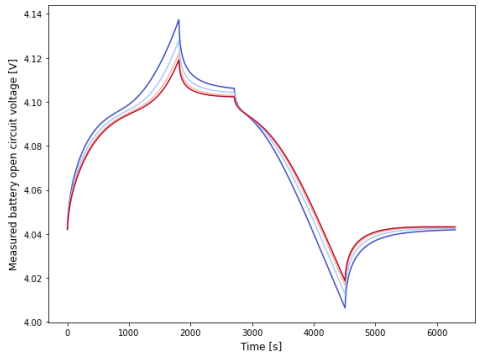

(e) NMC battery pack Open circuit Potential

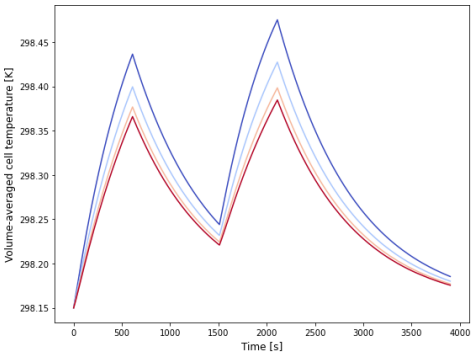

(f) NMC battery pack Temperature

Figure A.6: NMC pack model variables using SPM model with a pack of 4 in parallel and 1 in series

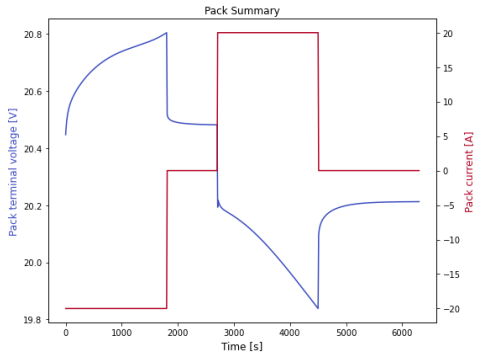

(a) NMC large battery pack terminal voltage and current

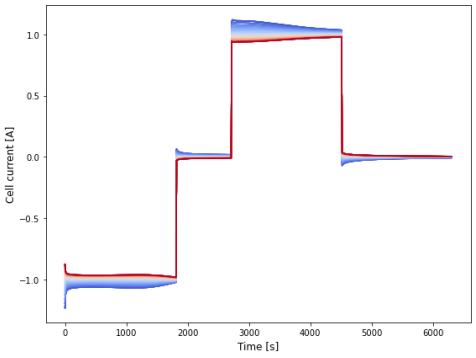

(b) NMC large battery pack current

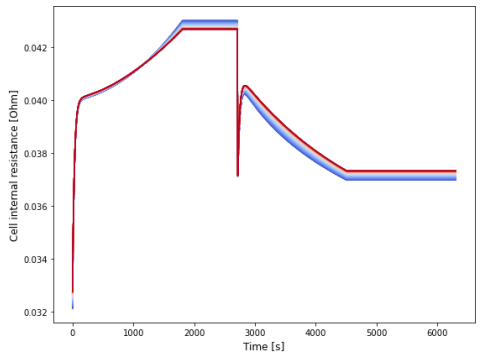

(c) NMC large battery pack internal resistance

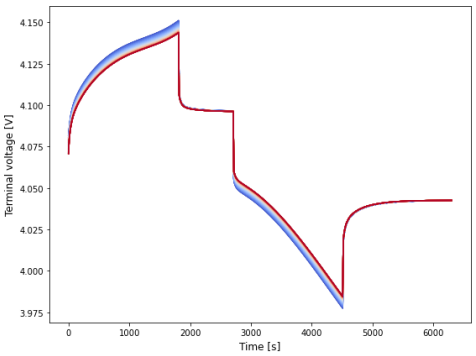

(d) NMC large battery cell voltage

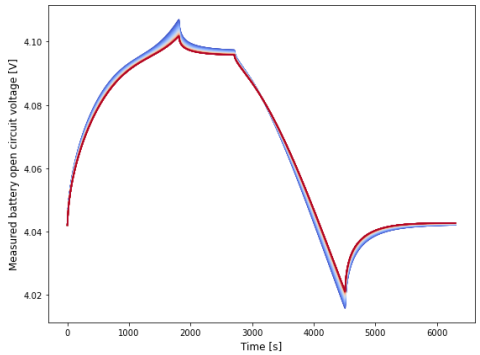

(e) NMC large battery pack Open circuit Potential

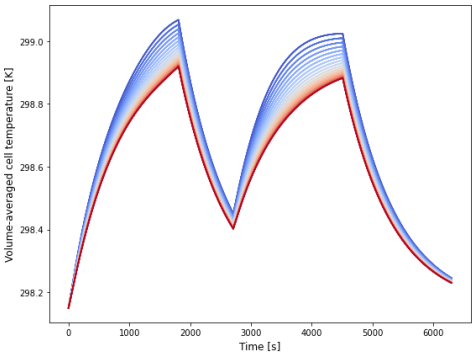

(f) NMC large battery pack Temperature

Figure A.7: NMC pack model variables using SPM model with a pack of 20 in parallel and 5 in series

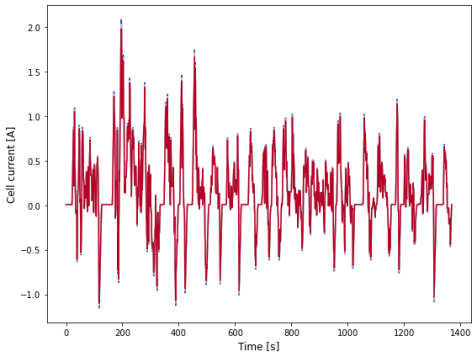

(a) NMC battery pack current for UDDS drive cycle

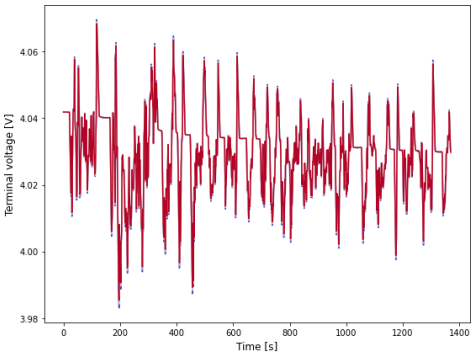

(b) NMC battery pack voltage

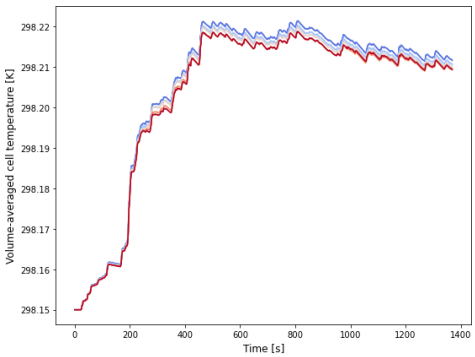

(c) NMC battery pack Temperature

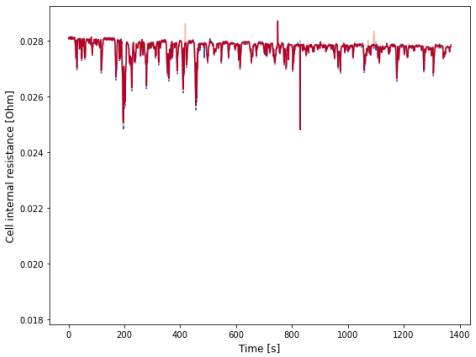

(d) NMC battery pack internal resistance

Figure A.8: NMC pack model variables using SPM model with a pack of 4 in parallel and 1 in series with a UDDS drive cycle.